Delft University of Technology

Multi-pinhole Molecular Breast Tomosynthesis: from Simulation to Prototype

Wang, Beien

DOI
10.4233/uuid:d78075cb-7614-4248-b3f5-65a5fd4b3586

Publication date
2020

Document Version
Final published version

Citation (APA)
Wang, B. (2020). *Multi-pinhole Molecular Breast Tomosynthesis: from Simulation to Prototype*. [Dissertation (TU Delft), Delft University of Technology]. https://doi.org/10.4233/uuid:d78075cb-7614-4248-b3f5-65a5fd4b3586

Important note
To cite this publication, please use the final published version (if applicable).
Please check the document version above.

Copyright
Other than for strictly personal use, it is not permitted to download, forward or distribute the text or part of it, without the consent of the author(s) and/or copyright holder(s), unless the work is under an open content license such as Creative Commons.

Takedown policy
Please contact us and provide details if you believe this document breaches copyrights.
We will remove access to the work immediately and investigate your claim.

This work is downloaded from Delft University of Technology.
For technical reasons the number of authors shown on this cover page is limited to a maximum of 10.

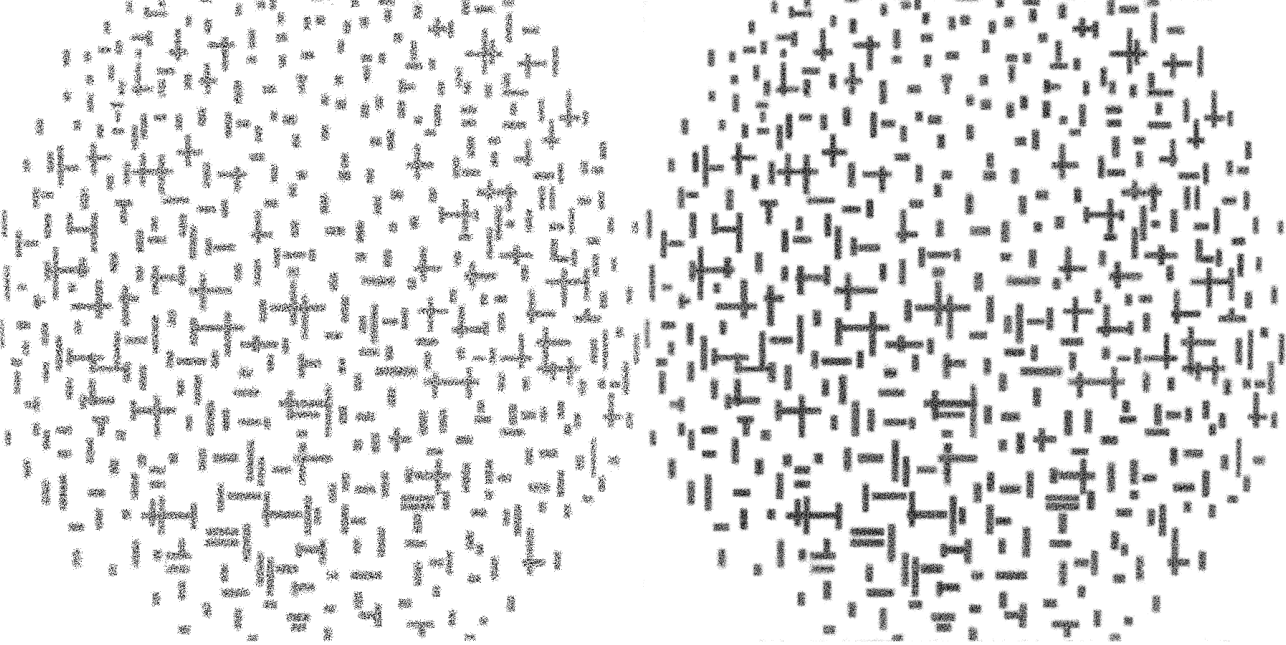

Multi-pinhole Molecular Breast Tomosynthesis: from Simulation to Prototype

Beien Wang

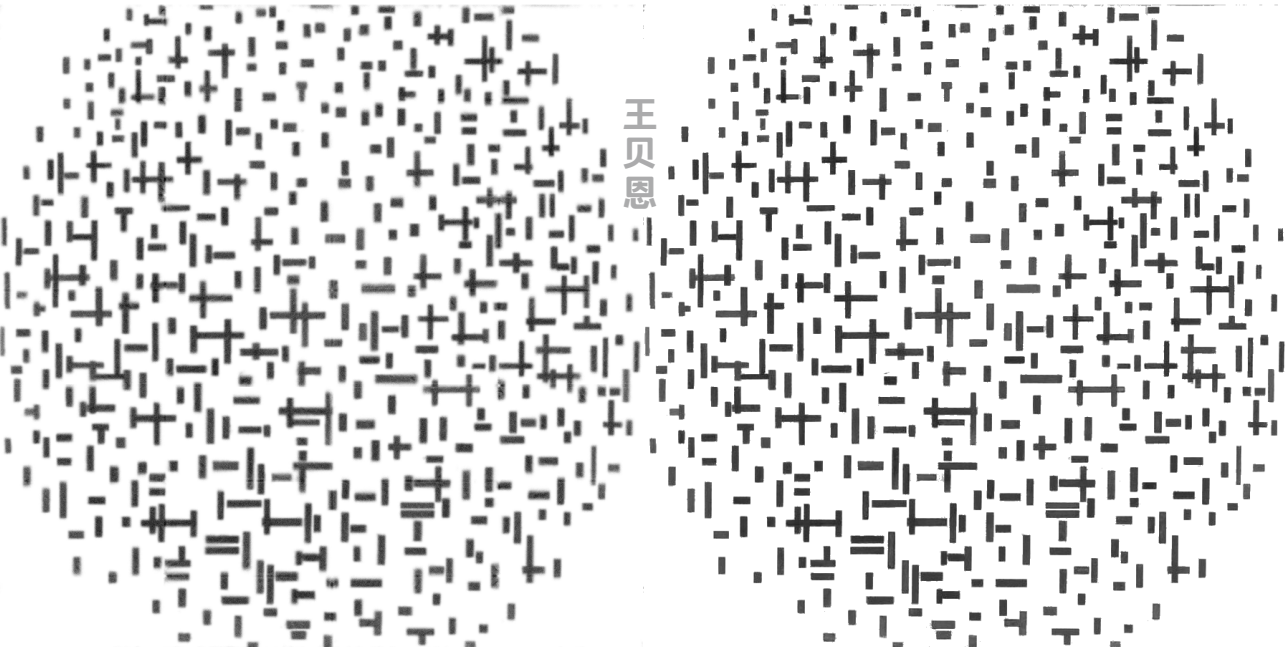

Propositions

accompanying the dissertation

Multi-pinhole Molecular Breast Tomosynthesis: from Simulation to Prototype

by

Beien Wang

1. If you want to solve an inverse problem, concentrate on the forward problem. — *Foundations of Image Science* by Harrison H. Barrett and Kyle J. Myres
2. After assembling a detector system, a common experience is that it doesn't work as expected. — *Semiconductor Detector Systems* by Helmuth Spieler
3. Mammography must have been invented by MEN because the whole process is a kind of torture for WOMEN. — a friend of a friend
4. When a field of study stagnates, research in this field tends to be like (supposedly) Igor Stravinsky's comment on Antonio Vivaldi's music: Vivaldi did not write 400 concerti, but he wrote one concerto 400 times.
5. Kitchenware shops are good places to look for lab tools.
6. It is nice to have Chinese students in the group because they know better how to use Alibaba. — Freek J. Beekman
7. A language is a dialect with an army and navy. — Yiddish wit

These propositions are regarded as opposable and defendable, and have been approved as such by the supervisor Prof. Dr. F. J. Beekman.

Stellingen

behorende bij het proefschrift

Multi-pinhole Molecular Breast Tomosynthesis: from Simulation to Prototype

door

Beien Wang

1. Als je een omgekeerd probleem wilt oplossen, concentreer je dan op het voorwaartse probleem. — *Foundations of Image Science* by Harrison H. Barrett and Kyle J. Myres

2. Na het samenstellen van een detectorsysteem is een veel voorkomende ervaring dat het niet werkt zoals verwacht. — *Semiconductor Detector Systems* by Helmuth Spieler

3. Mammografie moet door MANNEN zijn uitgevonden omdat het hele proces een soort marteling is voor VROUWEN. — een vriend van een vriend

4. Wanneer een vakgebied stagneert, lijkt onderzoek op dit gebied op (vermoedelijk) Igor Stravinskys commentaar op de muziek van Antonio Vivaldi: Vivaldi schreef geen 400 concerten, maar hij schreef 400 keer één concert.

5. Keukengerei winkels zijn goede plekken om naar laboratoriumgereedschap te zoeken.

6. Het is leuk om Chinese studenten in de groep te hebben omdat ze beter weten hoe ze Alibaba moeten gebruiken. — Freek J. Beekman

7. Een taal is een dialect met een leger en een vloot. — Jiddisch aforisme

Deze stellingen worden opponeerbaar en verdedigbaar geacht en zijn als zodanig goedgekeurd door de promotor prof. dr. F. J. Beekman.

Multi-pinhole Molecular Breast Tomosynthesis: from Simulation to Prototype

Proefschrift

ter verkrijging van de graad van doctor

aan de Technische Universiteit Delft,

op gezag van de Rector Magnificus prof. dr. ir. T. H. J. J. van der Hagen,

voorzitter van het College voor Promoties,

in het openbaar te verdedigen op dinsdag 19 mei 2020 om 12:30 uur

door

Beien WANG

Master of Science in Medical Engineering,
KTH Royal Institute of Technology, Stockholm, Zweden
geboren te Beijing (Peking), China

Dit proefschrift is goedgekeurd door de promotor.

Samenstelling promotiecommissie:

Rector Magnificus	voorzitter
Prof. dr. F. J. Beekman	Technische Universiteit Delft, *promotor*
Dr. ir. M. C. Goorden	Technische Universiteit Delft, *copromotor*
Onafhankelijke leden:	
Prof. dr. R. Boellaard	Vrije Universiteit Amsterdam
Prof. dr. L.-F. de Geus-Oei	Universiteit Leiden
Prof. dr. B. Rieger	Technische Universiteit Delft
Dr. ir. A. G. Denkova	Technische Universiteit Delft
Prof. dr. P. Dorenbos	Technische Universiteit Delft

This work is supported by the Dutch Organisation for Scientific Research (NWO) under the VIDI grant [project number 12371] 'Focused imaging of tumours'.

Keywords: pinhole collimator, breast imaging, SPECT, molecular imaging, Monte Carlo simulation, gamma detector

Printed by: Gildeprint – Enschede

Front & Back: The in-house detector's responses to perpendicularly collimated gamma beams in the shape of Piet Mondriaan's painting *Composition in line, second state*, 1916–1917 (Kröller-Müller Museum) at different noise levels.

Copyright © 2020 by Beien Wang

ISBN 978-94-6366-273-4

An electronic version of this dissertation is available at
http://repository.tudelft.nl/.

Contents

Summary v

Samenvatting vii

1 Introduction 1

2 Voxelized raytracing simulation dedicated to multi-pinhole molecular breast tomosynthesis 11

3 Simulation of novel light-guide-PMT geometries to reduce dead edges of a scintillation camera 39

4 Experimental validation of a gamma detector with a novel light-guide-PMT geometry to reduce dead edge effects 55

5 Characterisation of a multi-pinhole molecular breast tomosynthesis scanner 73

6 Conclusion 87

References 91

Acknowledgements. 103

Curriculum Vitæ 109

List of Publications 111

Summary

Breast cancer, being the most common cancer among females, is nowadays routinely diagnosed using X-ray mammography. Though this technique has proven its effectiveness in many cases, X-ray mammography has some disadvantages like reduced diagnostic sensitivity for dense breasts, need for strong breast compression and inability to assess tissues at the molecular level.

Therefore, there is a need of alternative imaging modalities to improve breast cancer diagnosis. One option is breast scintigraphy, which images the distribution of radiolabelled molecules, called tracers, that concentrate in the tumours in breasts with a planar gamma detector. Different tracers react in different physiological processes with tumours. Therefore imaging a specific tracer can reveal the specific pathological process that is specific for a certain kind of breast tumour. Despite the fact that breast scintigraphy has been reported to have improved diagnostic sensitivity in dense breasts compared to X-ray mammography and does not require strong compression, it offers only 2D images and information on the third dimension is thus lost. In this research we proposed a molecular breast tomosynthesis scanner which provides 3D images of the radiotracers in the breast. In the proposed system, the patient would lie prone on a patient bed with a hole in which the breast is inserted. Subsequently, two gamma cameras equipped with multi-pinhole collimators (therefore the technique is called multi-pinhole molecular breast tomosynthesis, MP-MBT) scan the pendant breast from both sides.

To estimate the performance of MP-MBT, the system was modelled in Monte Carlo simulations in a clinically realistic setting. The results assured us that it was worth building a prototype of MP-MBT to further investigate its imaging capability. Besides, voxelized raytracing (VRT) software developed earlier in our group to accelerate simulations and facilitate system optimisations was validated with the Monte Carlo simulation results. Subsequently, VRT was used in further studies in this project.

The promising results of MP-MBT simulations partly relied on a gamma detector with high spatial linearity over the whole detector surface. However, conventional gamma detectors used in clinical practice have large dead edges, i.e. about 4 cm from the detector edges is unusable, and a detector with small dead edges would be very expensive, which may make MP-MBT a less competitive technology. Therefore, in order to have a gamma detector suitable for MP-MBT, we came up with a few different designs with NaI(Tl) scintillators and photomultiplier tube (PMT) array readouts and evaluated their performances with Monte Carlo simulations. From the simulation results, we eventu-

ally chose a design with a staggered layout of 15 square PMTs, among which two PMTs detected the optical photons from the scintillator through extra-long additional light-guides. This gamma detector was built in our lab, and it turned out to have only about 15 mm dead edge (mainly due to the 12 mm sealing).

The customised gamma detector was equipped with a lead multi-pinhole collimator design based on previous research. The whole gamma camera was mounted on a robot arm to create a movable scanner. We calibrated the scanner with a point source and scanned a resolution phantom and a breast phantom to evaluate MP-MBT's performance. In the phantom study, the scanner showed the capability of detecting tumours down to 5 mm when a realistic tracer (technetium sestamibi) concentration was administered.

However, the current prototype is still far from a device that can be used in the clinic and we have found several problems with MP-MBT, especially the noise pattern in the reconstructed images, which should be given special attention in the future research.

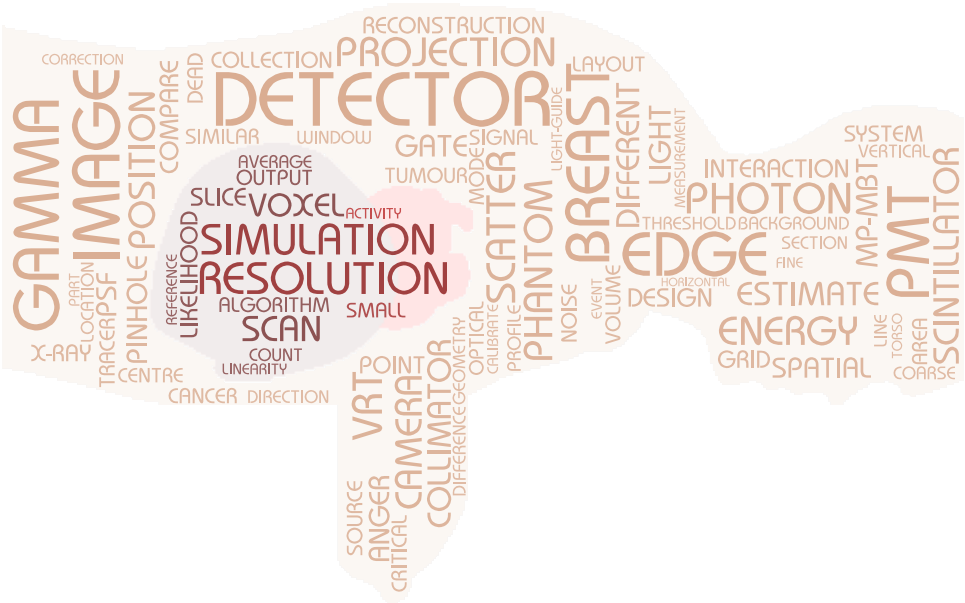

Samenvatting

Borstkanker, zijnde de meest voorkomende kanker bij vrouwen, is tegenwoordig routinematig gediagnosticeerd met behulp van röntgenmammografie. Hoewel deze techniek in veel gevallen zijn effectiviteit heeft bewezen, heeft röntgenmammografie enkele nadelen, zoals verminderde diagnostische gevoeligheid voor dichte borsten, behoefte aan sterke borstcompressie en onvermogen om weefsels op moleculair niveau te beoordelen.

Daarom is er opnieuw een behoefte van alternatieve beeldvormingsmodaliteiten om de diagnose van borstkanker te verbeteren. Eén optie is borstscintigrafie, waarbij beelden van de verdeling van de radioactief gemerkte moleculen, genaamd tracers, dat concentraat in de tumoren in de borsten met een vlakke gammadetector. Verschillende tracers reageren in verschillende fysiologische processen met tumoren. Daarom kan beeldvorming van een specifieke tracer het specifieke pathologische proces onthullen dat specifiek is voor een bepaald soort borsttumor. Ondanks het feit dat borstscintigrafie heeft werd gemeld te hebben verbeterde diagnostische gevoeligheid in dichte borsten in vergelijking met röntgenmammografie en heeft geen sterke compressie nodig, maar biedt alleen 2D-beelden en informatie over de derde dimensie is dus verloren. In dit onderzoek hebben we een moleculaire borsttomosynthesis scanner voorgesteld die 3D-beelden van de radiotracers in de borst levert. In het voorgestelde systeem zou de patiënt liggen gevoelig op een patiënt bed met een gat waarin haar borst ingebracht. Vervolgens twee gammacamera's tussen uitgerust met multi-pinhole collimatoren (dus de techniek multi-pinhole moleculaire borsttomosynthesis, MP-MBT) scant de hanger borst van beide kanten.

Om de schatting van de prestaties van de MP-MBT, werd het systeem gemodelleerd in Monte Carlo simulaties in een klinisch realistische setting. De resultaten als zeker van ons dat het de moeite waard was gebouwd een prototype van MP-MBT om verder te onderzoeken de beeldvormende mogelijkheden. Trouwens, voxelized raytracing (VRT) ontwikkelde software eerder in onze groep om de simulatie te versnellen en vergemakkelijken systeemoptimalisatie en werd gevalideerd met de Monte Carlo simulatie resultaten. Vervolgens, werd VRT constant gebruikt in verdere studies in dit project.

De veelbelovende resultaten van MP-MBT simulaties waren deels afhankelijk van een gammadetector met hoge ruimtelijke lineariteit over het hele detectoroppervlak. Echter, conventionele gammadetectoren die in de klinische praktijk worden gebruikt, hebben grote dode randen, dat wil zeggen ongeveer 4 cm van de detector randen onbruikbaar, en een detector met een kleine dode randen zeer duur zou zijn, waarbij MP-MBT min-

der concurrerend technologie kunnen maken. Daarom, om zo te een gamma-detector geschikt voor MP-MBT hebben, we kwamen met een paar verschillende ontwerpen met NaI(Tl) scintillator en fotomultiplicatorbuis (PMT) reeks uitlezingen en evalueerden hun optredens met Monte Carlo simulaties. Uit de simulatie resultaten, we uiteindelijk voor een ontwerp met een versprongen inrichting van 15 vierkante PMT's hebben gekozen, waaronder twee PMT's gedetecteerde optische fotonen van de scintillator met extra lange additionele lichtgeleiders. Dit gammadetector is in ons lab gebouwd, en deze bleek slechts ongeveer 15 mm dode rand hebben (voornamelijk door de 12 mm verzegeling).

De aangepaste gammadetector was uitgerust met een lood multi-pinhole collimatorontwerp op basis van eerder onderzoek. De hele gammacamera werd op een robotarm gemuteerd om een beweegbare scanner te maken. We hebben de scanner gekalibreerd met een puntbron en een resolutiefantoom en een borstfantoom gescand om de prestaties van MP-MBT te evalueren. In het fantoomonderzoek toonde de scanner het vermogen om tumoren tot 5 mm te detecteren wanneer een realistische tracer (technetium sestamibi) concentratie werd toegediend.

Echter, de huidige prototype is nog ver verwijderd van een apparaat dat kan worden gebruikt in de kliniek en we hebben een aantal problemen gevonden met MP-MBT, in het bijzonder het ruispatroon in de gereconstrueerde afbeeldingen, die moet worden gegeven speciale aandacht in de toekomst onderzoek.

1

Introduction

1.1. Breast cancer and current diagnostic technology

Breast cancer is the most common cancer among the female population. In 2012, about 1.7 million women worldwide were diagnosed with breast cancer and over 500,000 died of this disease. This constitutes 25% of cancer diagnoses and 15% of cancer deaths among women [1].

Nowadays, X-ray mammography is the routine technique to diagnose breast cancer and it has been proven to be able to effectively detect breast lesions in an early stage [2]. As early diagnosis and early treatment are key factors in breast cancer survival, the emergence of X-ray mammography since the 1950s has effectively reduced breast cancer mortality [3, 4]. Figure 1.1a shows a schematic illustration of the general setup of X-ray mammography. In this setup, the breast is fixed and firmly compressed against the X-ray detector by a compression paddle, behind which an X-ray tube is located. Only part of the X-rays emitted from the tube penetrate the breast and these are measured with an X-ray detector. As different tissues in the breast have different attenuation coefficients and thus absorb different amounts of X-rays, the images obtained from the X-ray detector provide information on the different tissue structures in the breast. This way, abnormal tissue structures can be interpreted as being lesions. The compression of the breast by the paddle is necessary as it reduces two important image-degrading effects. First of all, breast compression results in a decrease of X-ray scatter, a process in which photons are deflected from their original path leading to lower image contrast. Secondly, firm compression reduces tissue pile-up meaning that tumours hidden by anatomically overlaying healthy tissue.

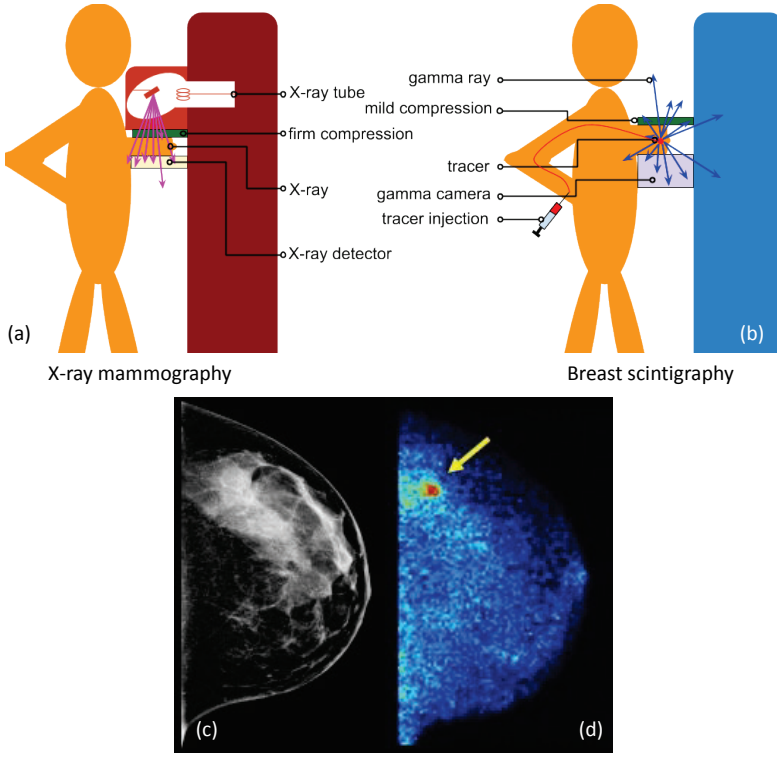

Figure 1.1: Schematic visualisation of planar X-ray and nuclear imaging of the breast. (a) X-ray mammography in which the breast is compressed as much as reasonably possible; the X-ray tube which generates X-rays and the X-ray detector are also shown. (b) Breast scintigraphy in which only mild compression is applied to the breast for fixation; the tracer which binds to the tumour and emits gamma rays is injected in the arm and transported to the target through the cardiovascular system (simplified in the figure). (c) An image obtained with X-ray mammography. (d) An image obtained with breast scintigraphy. (c) and (d) are *used with permission of Mayo Foundation for Medical Education and Research, all rights reserved.*

X-ray mammography provides 2D projection images of the compressed breast; in practice two images are taken in different directions. In principle, if many of such 2D projections are made at different angles, for example by rotating the detector and the X-ray tube around the breast, a 3D image of the breast can be computed from all these projections. If the rotation has an angular range exceeding 180°, such a technique is called X-ray Computed Tomography (CT). In general purpose CT, the X-ray tube and detector rotate around the patient's torso, which leads to significant scatter in the torso and therefore does not result in high-quality breast images. A breast-specific CT in which X-ray tube and detector are rotating around the breast is not easy to apply because of the spatial limitation and its image quality would still be hampered by the scatter in the uncompressed breast [5]. An X-ray scanner, however, with more limited angular range around a compressed breast is feasible. Obtaining 3D images from such a limited number of angles is generally referred to as tomosynthesis, and more specifically by X-ray breast

tomosynthesis for this specific case. Like CT, X-ray breast tomosysthesis also generates 3D images, but the image quality can be largely non-isotropic, unlike the fully 3D images from CT. The images from X-ray breast tomosynthesis reduce the tissue pile-up issue, and thus provide higher diagnostic value than 2D images [6]. Moreover, information on the 3D shape of the lesion becomes available in breast tomosynthesis [7–9].

Both X-ray mammography and X-ray breast tomosynthesis give a high overall diagnostic sensitivity of 70% — 90% (with sensitivity being defined as the fraction of breast cancers diagnosed successfully in examinations) with acceptable radiation dose (0.5 — 1.2 mSv; compared with a normal annual dose from the environment of 1 — 3 mSv) [10, 11]. X-ray breast tomosynthesis even provides the 3D information that X-ray mammography does not. However, these imaging modalities have two main disadvantages. The first disadvantage is that the diagnostic sensitivity for dense breasts drops significantly to 30% — 50%, i.e. it becomes very hard to distinguish lesions from normal tissue in dense breast X-ray images, which is especially disadvantageous as denser breasts are associated with a higher risk of getting breast cancer [10, 11]. The second disadvantage is that the strong compression of the breast during an examination is a huge discomfort for many women. Recently, there are studies showing that less strong compression does not necessarily reduce breast cancer detectability [12–14]. However, in clinical practice, it is still common to apply strong compression. All these disadvantages together drive many researchers to investigate alternatives to X-ray imaging techniques, e.g. magnetic resonance imaging (MRI), ultrasound imaging, optical imaging, and nuclear imaging.

Of these alternative imaging techniques, MRI, ultrasound and optical imaging have the advantage that no ionising radiation is involved; these techniques are sometimes accompanying X-ray mammography to diagnose breast cancer. MRI shows high diagnostic sensitivity to breast lesions especially for dense breasts (over 80%), but the diagnostic specificity is relatively low (around 70%; meaning that a large fraction of the MRI diagnosed breast lesions are actually benign, but still need to be investigated further with biopsies) [15, 16]. Moreover, MRI examination is quite expensive and not suitable for everyone, e.g. for patients with claustrophobia. Ultrasound is a cheap and fast imaging modality, and a combination of ultrasound and X-ray mammography has been reported to increase the diagnostic sensitivity [17]. However, the information ultrasound imaging provides is highly operator-dependent, which means that if the sonographer is not an expert in breast ultrasound imaging, the images can be easily misinterpreted. Optical imaging of breast cancers is still largely in the research stage and is probably not going to become a general clinical technique in the near future as optical photons do not have enough penetrative power to image lesions deep in the breast [18]. Nuclear imaging, of which planar scintigraphy, single photon emission computed tomography (SPECT) and positron emission tomography (PET) are the most common methods, will be discussed in the next section.

1.2. Molecular breast imaging

Medical imaging modalities are often divided into two categories according to their imaging 'philosophy'. The first category constitutes structural/anatomical imaging, in which the position, shape, and structure of certain tissues and organs are visualised. The other category entails functional/molecular imaging, in which the physiological process of interest is marked and visualised. The aforementioned X-ray mammography, X-ray breast tomosynthesis, general purpose X-ray CT, MRI, and ultrasound imaging belong to the structural/anatomical imaging class, while nuclear imaging modalities such as planar scintigraphy, PET and SPECT are functional/molecular imaging techniques. As functional images reflect the physiological processes inside an organism, function methods have been widely used in cancer diagnosis, therapy monitoring, pharmaceutical science, and neuroscience. Figure 1.1c and d show a comparison of 2D images of the same breast obtained with anatomical imaging (X-ray mammography) and molecular imaging (breast scintigraphy). It can be seen that although Figure 1.1d does not contain much structural details, the lesion is clearly emphasised, which indicates that molecular imaging can have better diagnostic sensitivity and specificity than anatomical imaging.

In planar scintigraphy, SPECT and PET, the patient is injected with a chemical solution, a so-called tracer, which (in case of cancer imaging) is preferably taken up by tumour cells. A tracer is radioactive and results in high-energy photons (directly through radioactive decay or indirectly through electron-positron annihilation), which allow to track the tracer and thus determine the location of the tumour cells. SPECT, particularly, can image multiple tracers simultaneously, meaning that multiple tumour metabolic reactions and the relationship between them can be visualised, which is particularly useful in preclinical studies and interesting in clinic [19–21]. With the development of new tracers, molecular imaging techniques (especially SPECT and PET, but also molecular breast imaging) may not only be used to locate the tumours, but also characterise them and even treat them simultaneously [22–24].

Planar scintigraphy and SPECT use single photon emitting radioisotopes as tracers and collimators to limit the incoming gamma photons' directions. While planar scintigraphy is a direct imaging technique where the measured projections provide the 2D images, in a SPECT scanner the patient is imaged over an angular range of at least 180° (in practice usually 360°) and 3D images are computed from the measured projections. PET uses positron emitting radioisotopes as tracers and coincidence detection of a pair of annihilation photons resulting from electron-positron annihilation to determine the line-of-response. From these lines-of-response the 3D distribution of the tracer can be reconstructed. However, due to the limited availability of PET scanners and tracers, PET is not often used in clinic for breast cancer diagnosis. New PET tracers and instruments for breast cancer are under development, thus PET may potentially play a bigger role in breast imaging in the future [25–27]. In this thesis we present a molecu-

lar breast tomosynthesis (MBT) scanner which, like SPECT, images the 3D distribution of single gamma photon emitting tracers but does so over a limited range of angles (hence the name 'tomosynthesis' instead of 'tomography'). It should give similar images as Figure 1.1d, but with more information, as spatial information in the third dimension is added.

Nowadays, several commercial planar breast scintigraphy systems have been developed [28, 29] and several studies have reported that these can be superior to X-ray imaging in terms of diagnostic sensitivity, i.e. about 80% — 90%, for dense breasts [11, 30, 31].

While breast scintigraphy can be viewed as the functional version of X-ray mammography, the MBT scanner we are developing can be considered as a functional version of X-ray breast tomosynthesis. In planar breast scintigraphy and MBT, strong compression of the breast as in X-ray mammography and X-ray breast tomosynthesis is not applied, as the imaging time is long (typically 10 to 20 minutes) and strong compression of the breast over such a time span is not feasible. Moreover, gamma photons have usually higher energies than X-ray photons used in breast imaging and the role of scatter in anatomical and functional imaging is different. Both reasons make mild compression of the breast in molecular breast imaging less problematic than it would be in X-ray breast imaging. Additionally, as relatively high-energy gamma photons are used, there is also no reason to believe that diagnostic sensitivity would depend on breast density; this has indeed already been demonstrated in planar breast scintigraphy [11, 30, 31].

Figure 1.2a and c shows the design of the MBT scanner we are developing [32, 33]. The top of the scanner is a bed on which the patient lies while her breast is inserted into a hole in the bed. Inside the hole (Figure 1.2a and b), two gamma cameras scan the breast, which is mildly compressed for fixation, from opposite sides. With the multi-pinhole collimator shown in Figure 1.2b and d, these two gamma cameras are able to obtain projections from multiple angles simultaneously and thus a 3D image of the tracer distribution in the breast can be calculated from them.

1.3. Gamma Camera

Figure 1.3 illustrates the different components of a gamma camera in comparison with those from a digital optical camera. A gamma camera visualises distributions of gamma sources while an optical camera visualises optical sources. The collimator in a gamma camera serves a bit like the lens in an optical camera: the former provides directional information for the incoming gamma photons, while the latter links the detection positions of optical photons to those of the optical sources. The gamma detector in Figure 1.3b, which is made of a scintillator, a light-guide, and a PMT array, serves a similar purpose as the CCD optical detector in Figure 1.3a: the former gives the positions at which the gamma photons get absorbed while the latter provides the absorption position of the optical photons. With knowledge of the detected position of the gamma/optical photon

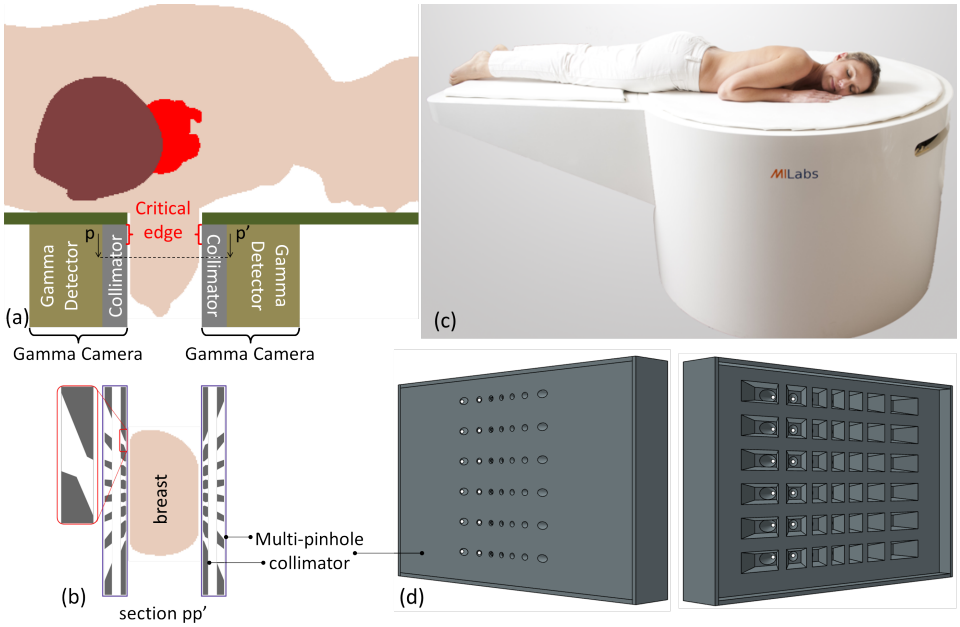

Figure 1.2: (a) Inside the hole in the patient bed, two gamma cameras scan the breast from opposite directions; every gamma camera comprises a collimator and a gamma detector. The critical edge, the upper edge of the gamma camera close to the patient's chest wall, is marked; (b) Section pp′ from (a) is shown with the converging multi-pinhole geometry displayed in detail. (c) Conceptual picture of a MBT scanner with a patient lying on a bed. (d) A 3D conceptual drawing of the multi-pinhole collimator viewed from the front and back.

and its relationship with the object, a planar image of an object can be obtained.

1.3.1. Collimator

A key difference between collimators and their counterpart camera lenses is that the former regulate the incoming gamma photons' directions at the expense of a huge loss of gamma photons, while the latter does not induce a significant optical photon loss. As gamma photons are of very high energy compared to optical photons, it is impossible to use refraction, and thus the strategy of direction control is to shape high-density material, e.g. tungsten or lead, in a certain geometry such that gamma photons are selectively absorbed based on their direction. Figure 1.3b shows a so-called parallel hole collimator, which is the most common type of collimator. It consists of a heavy metal slab with many small parallel holes inside. Gamma photons travelling in a direction that is approximately parallel to the holes can pass through, while gamma photons in other directions are absorbed by the slab.

There are also other types of collimators, and the most common type beside the parallel hole collimator is the pinhole collimator. Figure 1.4 shows a comparison between a parallel hole collimator and a pinhole collimator for mouse imaging. While for the paral-

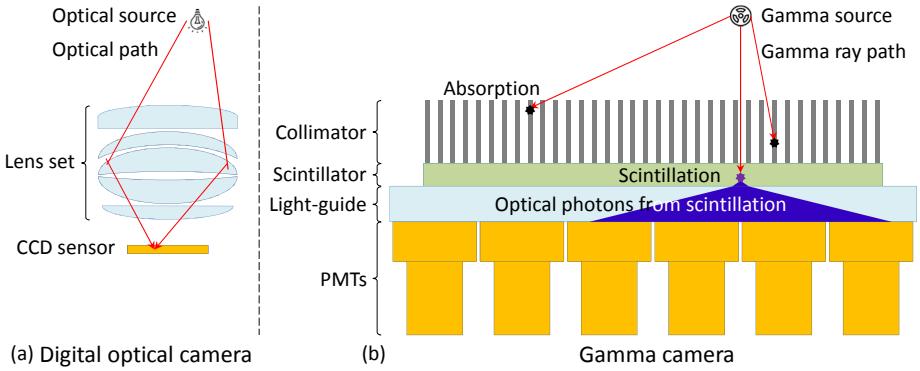

Figure 1.3: Illustration of a digital optical camera (a) and a gamma camera (b).

lel hole collimation, the projection on the detector is of the same size as the object, for the pinhole collimator the projection size depends on the pinhole-object distance and pinhole-detector distance. If, as Figure 1.4 shows, the pinhole-object distance is smaller than the pinhole-detector distance, the image will be a magnified version of the object. In all cases, the finite resolution of the gamma detector will cause the detector image to be blurred. However, when the projection on the detector is magnified, the image resolution can be better than the intrinsic detector resolution. For small objects, pinhole imaging is especially beneficial because in this case the pinhole can be placed very close to the activity (meaning very large magnification factors) while the entire magnified object still fits the detector.

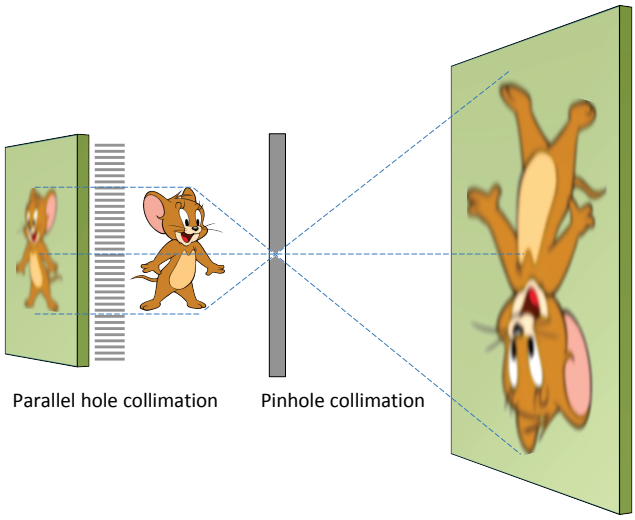

Figure 1.4: Illustration of the effect of parallel hole collimation (image has the same size as the object) and pinhole collimation (image is larger than the object if the image-pinhole distance is larger than object-pinhole distance).

As the intrinsic detector resolution is no longer a limiting factor, the spatial resolution

of a pinhole system will largely depend on the diameter of the pinhole. The smaller the pinhole diameter, the higher the resolution of the system. However, as a trade-off, if the pinhole diameter is too small, only a very small fraction of emitted gamma photons will go through the pinhole, and as a result the system sensitivity will be very low [34, 35]. A lower sensitivity means that it takes a longer time or higher amount of radioactive tracer to get a sufficient amount of photons to obtain a suitable image, which is often not practical.

To obtain high sensitivity while maintaining the high resolution property of a pinhole collimator, the concept of focusing multi-pinhole collimation was proposed [36, 37]. In this concept, multiple pinholes focus on the object and both high sensitivity and high resolution is achieved at the focus. The focus is small to ensure all pinhole projections fit onto the detector without much overlapping, and thus multi-pinhole collimator imaging is especially useful for imaging small animals, e.g. mice or rats [38]. Multi-pinhole collimator-based SPECT has already been widely applied in preclinical and pharmaceutical research with small animals [19, 39–42], and nowadays this technique is extended to image parts of the human body, like the heart or brain [43–47]. As is shown in Figure 1.2b and d, the MBT system we are developing is also based on multi-pinhole collimation, and the technique is thus called multi-pinhole (MP-)MBT [32, 33, 48].

1.3.2. Gamma detector

The gamma detector shown in Figure 1.3b is the earliest design used for scintillation imaging, which was invented by Hal O. Anger in 1950s (therefore dubbed 'Anger camera')[49]. It consists of a continuous piece of scintillator, a light-guide, and an array of PMT readouts, and today it is still the most widely-used camera design in SPECT because of its generally good performance and cost-effectiveness [50].

Nowadays, however, there are many different gamma detector designs. The principle on which the detector operates can be used to categorise detectors into two types. The first type directly converts gamma photon energy into an electrical signal. These detectors are mostly made of heavy semiconductor crystals, e.g. germanium, cadmium telluride, and cadmium zinc telluride [51, 52]. These detectors are compact and have a very high energy resolution, i.e. one can easily distinguish the photons with desired energy from other (scattered) photons. Unfortunately prices of semiconductor detectors are also very high. The second type of gamma detector uses indirect conversion: first the gamma photon's energy is converted into an optical signal, and then light sensors convert this optical signal into an electrical signal. The Anger camera in Figure 1.3b belongs to this type. The crystal which converts gamma photon energy into an optical signal is called the scintillator. When a gamma photon entering the scintillator is absorbed, thousands of optical photons are emitted isotropically, a process called scintillation. The most commonly used scintillator material is sodium iodide (NaI) doped with thallium (Tl). The light

sensor array mounted on the scintillator records the distribution of the scintillated optical photons and from this distribution, the gamma photon interaction position in the scintillator can be estimated. The light sensors used in scintillation gamma detectors are mostly photomultiplier tubes (PMTs) [49, 50]. CCD sensors are not sensitive enough and are very expensive in large sizes, so they are not often the first choice in gamma cameras [53]. The scintillator is typically a few to a few tens of millimetres thick, while the size of the PMT's sensitive area ranges from a few millimetre to a few tens of millimetre (in medical imaging applications). If only one light sensor detects the scintillated optical photons, the resolution would be the size of the light sensor, which is often not enough. In order to let more light sensors detect the optical photons from each scintillation, a light-guide (made of glass or another transparent material) is often placed between the scintillator and the light sensor array.

For every gamma photon interaction in the scintillator-based gamma detector, each light sensor will give a signal representing the amount of optical photons from this interaction location reaching this light sensor. The light sensors close to the interaction position will receive more optical photons, i.e. higher signal, and the light sensors far away from the interaction position will get lower signal. Based on the relative intensity of these signals, the interaction position can be estimated. Conventional gamma detectors with PMT output used a resistor/capacitor network to calculate the interaction position analogously with a weighted average method (the average of all PMT outputs to an interaction event weighted by the PMT positions). This method is called Anger logic, named after the inventor Hal O. Anger as well [49]. Nowadays, the available electronic technology facilitates us to process the PMT signals with more complex algorithms, but Anger logic is still a good starting point of gamma photon interaction position estimation. The detector designed for MP-MBT also uses a NaI(Tl) scintillator readout by a PMT array (a modified Anger camera) with an Anger-like algorithm as the start of interaction position estimation. This is an affordable and technically mature solution which has been proven to be good enough in most large-area detection cases.

As Anger logic uses a weighted average algorithm to estimate the interaction position, its performance is compromised near the edges of scintillator, which is often referred to as the dead edge problem. Conventional gamma detectors used in full-body SPECT systems have dead edges as large as the radius of PMTs used (about 40 mm). But fortunately these gamma detectors are large, and they need to rotate over 180° during the imaging process, so the dead edges can be compensated by the movement and usually does not lead to a serious degradation of the reconstructed images. However, in the MP-MBT system in Figure 1.2, the upper edge of the gamma camera is very close to the chest wall, and if conventional gamma detectors were to be used in this application, the scanner can hardly image this upper edge. For this reason, solving this dead edge issue is one of the topics of this thesis, and throughout it the upper edge of the gamma camera will be referred to as the critical edge.

1.4. Outline of the thesis

This thesis focuses on the experimental realisation of a MP-MBT prototype scanner. The initial design and estimated performance of the scanner were studied in an earlier simulation study [32], and in **Chapter 2**, a full Monte Carlo simulation of the entire scanner was done. This not only validated the quick simulation method used for earlier system optimisation (voxelized raytracing), but also provided the first analysis of the influence of scattered photons on the images

In **Chapter 3**, we attempt to solve the dead edge issue of the gamma detector. In a Monte Carlo simulation study, we simulated several possible affordable detector geometries all based on the use of continuous NaI(Tl) scintillators that are read out by PMTs. Unconventional light-guide geometries which allowed us to effectively realise small-sensitive area PMTs near the critical edge in a cost-effective way were proposed. We evaluated which design gave the best overall performance and met our needs.

The best performing gamma detector in **Chapter 3** was built and is experimentally evaluated in **Chapter 4**. We overcame the engineering difficulties, acquired the necessary parts, and manufactured several customised components. A thorough evaluation of the detector in terms of its spatial resolution, spatial linearity, energy resolution, and uniformity was performed. We concluded that the built detector was a cost-effective solution to the dead edge problem and that it met our requirements for the MP-MBT detector.

With the gamma detector at hand, we manufactured a multi-pinhole collimator that was optimised for MP-MBT [33]. Together with several support parts, a proof-of-concept setup of MP-MBT was built. In **Chapter 5**, an evaluation of the prototype MP-MBT scanner was given based on the measurement with resolution phantom and breast phantom. The experimental results showed that the aimed 3D detection of sub-centimetre tumours was achieved.

In the end, a concluding **Chapter 6** was given, as well as a discussion of current problems and suggestions for future research.

2

Voxelized raytracing simulation dedicated to multi-pinhole molecular breast tomosynthesis

This chapter is adapted from:
Beien Wang*, Jarno van Roosmalen*, Louis Piët, Marcel A. van Schie, Freek J. Beekman, Marlies C. Goorden. *Voxelized ray-tracing simulation dedicated to multi-pinhole molecular breast tomosynthesis*, Biomedical Physics & Engineering Express **3**.4 (2017), 045021 [54].
**These two authors have equally contributed to this work.*

Accurate gamma photon transport simulations of emission tomography systems are important to optimise system geometries and for iterative image reconstruction. Monte Carlo simulation (MCS) is widely established for this purpose but has the disadvantage of being prohibitively slow. Voxelized RayTracing (VRT) can be used as an alternative but the accuracy of VRT needs to be assessed for each simulation task at hand. The aim of this work is to propose and validate dedicated VRT code for a novel radionuclide-based multi-pinhole molecular breast tomosynthesis (MP-MBT) scanner.

The MP-MBT system images radionuclide distributions in a mildly compressed breast using two opposing gamma cameras, each equipped with a focusing multi-pinhole collimator, that slide along opposite sides of the breast. VRT simulates gamma photon transport by tracing rays efficiently through the voxelized phantom, collimator, and detector volumes using Siddon's raytracing algorithm, accelerated by dual-grid methods. To assess its accuracy, we compare point spread functions (PSFs) calculated with VRT for different voxel sizes with those generated by the established MCS toolkit GATE. Furthermore, VRT and MCS-simulated projections of realistic anthropomorphic XCAT phantoms with different compressed breast sizes are compared, as well as reconstructed images obtained from these projections.

With VRT, PSFs for MP-MBT can be simulated accurately when the fine voxel size of VRT's dual-grid is 1/8 mm. Reaching a similar deviation from noiseless PSFs takes 29300 times longer with full MCS than with VRT. Furthermore, XCAT phantom simulations show that VRT-generated projections are very close to MCS-generated low-noise projections when these are corrected for scatter by the Triple Energy Window method. However, we also find that primary gamma photons from the torso may in some cases reach the detector, meaning that torso activity should not be neglected in VRT. Finally, reconstructed images obtained from projections generated by VRT and MCS are visually very similar and have no significant difference in contrast and noise characteristics.

We conclude that VRT can accurately and efficiently simulate MP-MBT even though it neglects scattered photons originating from the torso.

2.1. Introduction

Imaging of radiolabelled molecule distributions is gaining popularity for breast cancer diagnosis. Recently, several breast-specific gamma cameras have been proposed and significant advances in sensitivity of these cameras have been made [29, 55–60]. Next to these planar gamma cameras, there is also a growing interest in 3D molecular breast imaging. General purpose single photon emission computed tomography (SPECT) and positron emission tomography (PET) are not ideal for breast imaging because they often provide no higher diagnostic sensitivity and specificity than planar systems [30, 61]. Therefore, dedicated 3D molecular breast imaging techniques are being investigated [62–71]. Recently, we proposed dedicated molecular breast tomosynthesis based on sliding multi-pinhole collimators, MP-MBT [32, 46].

To investigate the performance of MP-MBT and to further optimise its design, its acquisition, and its reconstruction parameters, efficient simulation algorithms are useful. To be able to evaluate images that could be acquired with MP-MBT, one has to be able to generate both noisy ensembles of projections of realistic distributions, as well as the virtually noiseless point spread functions (PSFs, the detector's response to a point source of activity) that are used in image reconstruction. Monte Carlo simulation (MCS) is a powerful technique for assessing gamma photon transport [72] and its accuracy has been extensively validated in the scientific community. However, MCS is also notoriously time-consuming [73–75].

Several ways to speed up MCS exist, such as applying a large production threshold for secondary particles [76, 77], ignoring some of the physics processes generating secondary particles [78–80] or optimising code for a specific application [81]. New implementation strategies based on graphics processing units (GPUs) have also recently become available [82–84]. Another class of accelerated MCS uses variance reduction techniques such as forced detection, angular response function modelling or fictitious interaction [73, 74, 85–91]. However, even with modern hardware and advanced acceleration techniques, for certain applications, MSC is still prohibitively slow and complete system simulations often take days [84, 91].

If the effects of scatter are negligible or correctable in a gamma imaging system, a simulation that only models attenuation but ignores scatter is a possible way to reduce calculation time. This can be done using a simple raytracing algorithm, in which the paths from the gamma source to the detector are tracked and attenuation of gamma photons along these paths is calculated. Analytical raytracing software, in which phantom, collimator and detector geometries are described by analytical functions, has been used to generate PSFs for simple imaging systems quickly and noiselessly [92–94]. For complicated geometries which are difficult to describe analytically, such as irregular phantoms in CT and SPECT, discrete raytracing, in which geometries are represented by a finite number of voxels or layers, is more practical [95–101]. Among these discrete raytracers, those that use a representation of volumes in cubic voxels (Voxelized RayTracing, VRT) are the most straightforward and suitable to represent highly irregular structures.

Voxelization of continuous structures introduces simulation errors since edges are no longer smooth but composed of cubic elements. The use of very fine voxels can reduce the error but puts a strain on memory requirements and slows down computation time. Solutions that have been proposed to circumvent the issue of balancing accuracy and simulation time in volume representation include using hybrid analytical-voxelized representations [85], employing non-cubic voxel shapes [102, 103] or using a spatial subdivision method such as an octree voxel size structure [104, 105]. Octree is a method for describing an object by repeatedly dividing a cubic voxel into eight smaller cubic regions until each region becomes homogeneous. It has been applied in medical imaging simulations [106–110] and is, nowadays, widely used in 3D graphics for representing irregular

volumes.

In previous medical imaging instrumentation research in which VRT was applied, only phantoms or detectors were represented by voxels [95–99, 101, 111]. In contrast, we developed VRT software in which all volumes (gamma emitter, phantom, collimator and gamma detector) are voxelized. Fixed voxel sizes are used in phantoms and detectors, but in the collimator volume for which precise geometrical knowledge is crucial and through which raytracing is most time-consuming, a form of an octree-like voxel structure with two different voxel sizes is used. Though VRT provides an attractive alternative to MCS in testing system geometries such as MP-MBT, its validity lies in the prerequisite that scatter is negligible or correctable. As tracer uptake in breast imaging is relatively high in organs such as the liver and heart [112, 113], a careful assessment of its contribution in our MP-MBT system is required. For other breast gamma imaging geometries, different amounts of scatter contamination were reported and it is thus not a priori clear what the amount of scatter is in MP-MBT [63, 114–119].

The aim of this paper is to propose our specific VRT implementation and to validate the use of VRT for MP-MBT. To this end VRT is compared against the MCS software package GATE (GEANT4 Application in Tomographic Emission [76, 77]) which is considered to be the gold standard. PSFs, projections, and reconstructed images of the anthropomorphic XCAT phantom [120] are generated by both software packages and simulation accuracy of VRT and its dependence on collimator volume voxel size settings are analysed.

2.2. Methods

2.2.1. MP-MBT

The novel MP-MBT concept (shown in Figure 2.1) was proposed in [32, 46] in which a detailed description can be found. MP-MBT aims to image the distribution of single-gamma emitting tracers in the breast to detect possible malignancies. The breast is pendant through a hole in the patient bed (equipped with 3.2 mm thick lead for shielding) and is mildly compressed at levels similar to planar molecular breast imaging [29] with optically transparent plates, through which optical cameras (not shown in Figure 2.1) view the breast. These optical cameras generate images, from which users can select a volume-of-interest which is to be imaged. Imaging takes place by the two gamma cameras located underneath the patient bed, each equipped with a multi-pinhole collimator focusing on a volume smaller than the whole breast, cf. Figure 2.1b. The gamma cameras slide to various positions during scanning in order to cover the region designated by the user. Each of the 5 mm thick collimator plates, made of tungsten alloy (97% tungsten, 1.5% nickel, and 1.5% iron), has 42 round knife-edge pinholes. An 8 mm-thick shielding plate made of the same material is located between gamma detector and collimator plate. It has 42 rectangular holes, each of them corresponding to one of the pinholes in the collimator

respectively avoiding different pinhole projections from overlapping on the gamma detectors. Gamma detectors are assumed to consist of 250×150×9.5 mm^3 NaI(Tl) crystals read out by a PMT array. For 140 keV gamma photons (from ^{99m}Tc-Sestamibi, the most prominent tracer for breast tumour detection), 90% detection efficiency can be achieved by NaI of this thickness. With the projections obtained from the two gamma cameras, the 3D tracer distribution in the breast can be reconstructed using a maximum likelihood expectation maximisation algorithm [32, 121].

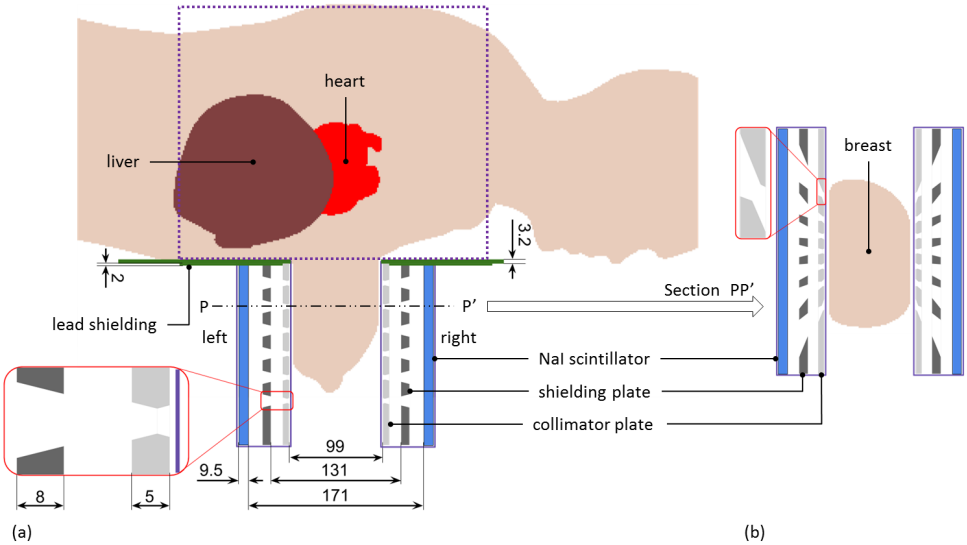

Figure 2.1: (a) Geometry of MP-MBT with the XCAT torso phantom placed in the scanner. The dotted rectangular box indicates the part of the torso phantom included in GATE simulations but not in VRT. The two gamma cameras can slide to different locations (indicated by the arrows) to focus on different parts of the breast. (b) A cross section through the gamma camera geometry (plane PP′ in (a)). All dimensions are in millimetre (mm).

2.2.2. VRT

VRT uses voxelized models of the detectors, collimators, phantoms, and the distribution of single-gamma emitters as its input. Each voxel is assigned a value which corresponds to the linear attenuation coefficient μ of its material at the energy of the gamma-emitter. When a gamma photon path crosses a voxel, the path length L through this voxel is obtained. Siddon's raytracing algorithm is used to quickly calculate path lengths in voxels [95]. Lambert-Beer's law,

$$P = e^{-\mu L}, \tag{2.1}$$

is then used to calculate the transmission probability P through the voxel. During raytracing, the transmission probabilities in the voxels that the ray passes are multiplied giving a total transmission probability. As there is always a finite probability for a gamma photon to pass through phantom and collimator, one could in principle calculate the full

transmission probability along every simulated gamma ray path. However, many gamma rays pass through large amounts of collimator material (tungsten alloy), making the transmission probability extremely small and it is computationally inefficient to keep track of all these paths. We, therefore, set a cut-off of 10^{-5} (2.76 mm collimator material) on the transmission probability through phantom and collimator below which raytracing is stopped.

The surface of the gamma detector is divided into detector pixels and each pixel is subdivided into 4×4 subpixels. For projection image assessment the pixel size is set to 1 mm, while for PSF assessment 0.5 mm is used. Gamma photons from each source position are tracked to the centres of all subpixels. The solid angle of each subpixel is taken into account by multiplying the transmission probability through the collimator of the gamma photons by the geometrical factor

$$P_{\text{geometry}} = \frac{d^2 \sin\theta}{4\pi R^2}, \tag{2.2}$$

where R is the distance from the voxel centre to the detector subpixel centre, d is the detector subpixel size, and θ is the angle of incidence of the gamma photon (see Figure 2.2a).

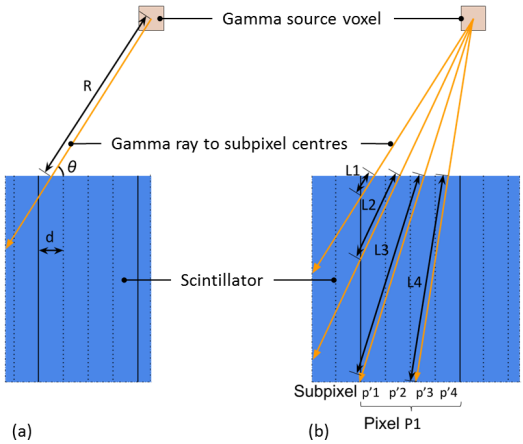

Figure 2.2: (a) The geometrical parameters used in Equation 2.2; (b) Illustration of the detector subpixel approach used in VRT. With the subpixel approach, the detection probability at pixel P1 is the sum of the absorption probabilities of subpixel p′1 — p′4, determined by path length L1 — L4. Discretisation errors are reduced by this subpixel approach.

The gamma photon is subsequently tracked through the continuous NaI(Tl) gamma detector which is represented in a voxelized form as well: it is subdivided into rectangular voxels with the length of each voxel being equal to the detector crystal's thickness (9.5 mm) and the area having the size of a detector subpixel. In the gamma detector, Lambert-Beer's law is again used to calculate the absorption probability in each detector voxel. Note that gamma photons that reach the detector under an angle can pass

different rectangular voxels and this way the varying depth-of-interaction in the detector is simulated (see Figure 2.2b). The attenuation coefficient of the detector is set to 0.217 mm^{-1}. This number is higher than the attenuation coefficient that solely includes photoelectric effect but lower than the total attenuation coefficient for 140 keV gammas in NaI (including Compton scatter). In fact, we set the attenuation coefficient such that the number of detected gammas in VRT with this attenuation coefficient is equal to the number of detected gammas found in the ±10% photopeak from GATE simulated PSFs. Thus, the added detector efficiency due to gamma photons undergoing multiple interactions in the scintillator is accounted for in VRT, but the scatter process itself which may impact spatial resolution is not taken into account. Finally, for each source position, absorption probabilities in all 4×4 detector subpixels corresponding to a detector pixel are added. The detector projection image acquired is then blurred with a Gaussian filter with 3.2 mm FWHM in order to simulate the intrinsic detector resolution. The idea of subdividing detector pixels to enhance modelling accuracy has been successfully applied in [101, 111] and the usefulness of this approach in MP-MBT will be evaluated in the results section.

The voxel sizes of collimator and shielding plates can have a significant impact on simulation results and they thus have to be chosen carefully. Generally, a small voxel size is preferable because it allows to better approximate the continuous structures in the geometry, but it also puts a strain on memory requirements and simulation time. To circumvent this issue, a dual-grid approach is used based on the idea of octree structure [105, 110]. Figure 2.3 is a 2D illustration of this approach: two different voxel sizes, a coarse one and a fine one, are used for the collimator/shielding volume. Initially, a photon is traced through the coarse voxel volume. In the coarse voxel volume, each voxel is designated to have one particular linear attenuation coefficient or it is assumed to be 'mixed' (i.e. the coarse voxel contains fine voxels with different linear attenuation coefficients). When a gamma ray is tracked through the coarse voxels, cumulative attenuation in the non-'mixed' voxels is calculated. When the ray reaches a 'mixed' voxel, VRT looks for the fine grid of this coarse voxel and continues raytracing in the fine voxels until the ray exits this coarse voxel. VRT checks whether the probability of transmission is lower than the cut-off after every fine/coarse voxel tracing.

With this dual-grid raytracing approach, the voxel size of the fine volume determines the accuracy of simulation while the combination of fine and coarse voxel sizes sets the computational speed. In this paper we first test six fine voxel sizes (1/2 mm, 1/4 mm, 1/8 mm, 1/16 mm, 1/32 mm, 1/40 mm) to determine the accuracy that we can achieve (with coarse voxel size fixed at 1 mm). Then, in order to optimise speed, we check six coarse voxel sizes (1/4 mm, 1/2 mm, 1 mm, 2 mm, 3 mm, 5 mm) to find out which one allows for the highest speed (with the optimal fine voxel size found above).

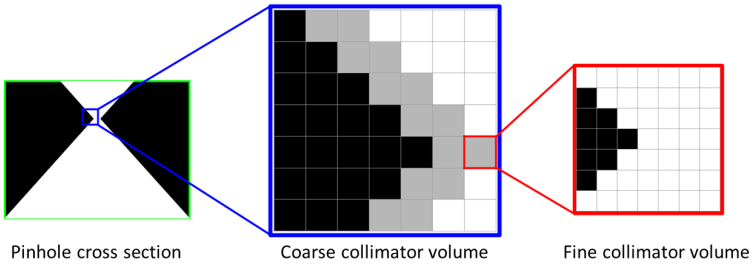

Figure 2.3: Illustration of dual-grid representation of collimator. The pinhole collimator volume consists of two materials: tungsten alloy (black) and vacuum (white). The grey coarse voxels are designated to be 'mixed' material and rays through these voxels are tracked on a finer volume.

2.2.3. MCS

To validate VRT, we use the MCS package GATE [76, 77], which is well-validated in gamma-ray imaging, radiation therapy, X-ray imaging, and optical imaging [122–129]. GATE 7.0 with Geant4 9.6 running on a CentOS 6.6 cluster is used. Only photoelectric effect, Compton scattering, and Rayleigh scattering are included in the physics list, since other physics processes are not expected to play major roles in our application [78–80]. The same geometry as simulated with VRT is also built in GATE. As we aim to assess the influence of finite voxel size in VRT, the collimator and shielding plates are generated with analytical shapes (head-to-head cones, trapezoids, and boxes), such that the GATE simulation does not suffer from discretisation effects due to the finite voxel size. The adder digitizer is applied to GATE outputs, which automatically records the interaction time, deposited energy, and energy-weighted averaged scintillator interaction position [76]. Gaussian blurring of energy is applied to each detector pixel to achieve 9% FWHM energy resolution, and Gaussian blurring in the spatial domain is also applied to simulate 3.2 mm FWHM resolution (as is done in VRT). To note, the blurring in energy and spatial domain acts as an acceleration factor of MCS and reduces noise. As we aim to compare GATE simulations with noiseless VRT, such a noise reduction is desirable. A difference between GATE photon tracking and VRT is that in GATE the gamma photons can be emitted in any possible direction, while in VRT only gamma photon paths from the centres of the gamma source voxels to the centres of the detector subpixels are accounted for. Figure 2.4 shows one of the two gamma cameras in GATE.

2.2.4. VRT accuracy and fine voxel size optimisation

To study the accuracy of VRT for different voxel sizes (of the fine volume), PSFs are obtained with VRT and GATE from point sources (ideal point source of infinitely small size) placed in the vacuum at 36 locations in front of the gamma camera (the blue crosses in Figure 2.4). The position designated by `ax1` is 11.5 mm from the front surface of the collimator plate and right on the axis of the central pinhole. The vertical interval (e.g. `a-b`

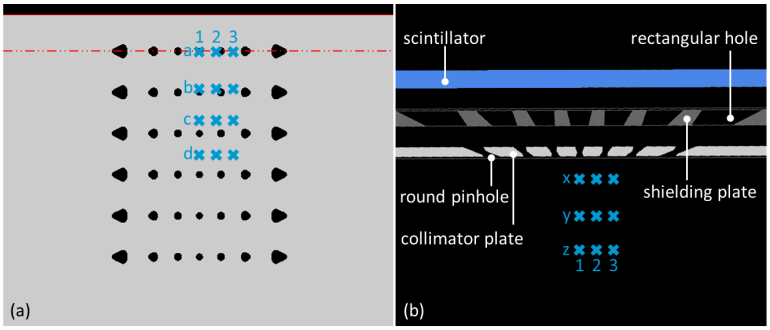

Figure 2.4: The gamma camera geometry used in GATE based on analytical shapes. (a) Front view of collimator; (b) cross section of the plane marked by a red dashed line in (a). The blue crosses indicate the locations where point sources are simulated to obtain the system's PSFs.

distance) between these locations is 20 mm, the horizontal interval (e.g. 1-2 distance) is 10 mm, and the depth interval (e.g. x-y distance) is 20 mm. These 36 positions cover about a quarter of the field of view and are representative of the whole field of view due to the symmetric allocation of the pinholes. Therefore, the voxel sizes optimised for these PSFs should also be the optimal voxel sizes for calculating the whole system matrix (containing all PSFs). To find how the fine voxel size influences accuracy, a sufficiently long GATE simulation of $5{\times}10^{10}$ isotropic emissions is done to obtain an almost noiseless reference PSF at each source location. The normalised root-mean-square error (NRMSE) between the PSFs obtained by VRT simulations with different fine voxel sizes (see 2.2.2) and the reference PSFs is calculated. It is defined by

$$\mathrm{NRMSE}_{\mathrm{GATE,VRT}} = \frac{\sqrt{\frac{\sum_{x=1}^{X}\sum_{y=1}^{Y}(n_{\mathrm{GATE}}(x,y)-n_{\mathrm{VRT}}(x,y))^2}{X\times Y}}}{n_{\mathrm{GATE,max}} - n_{\mathrm{GATE,min}}}, \tag{2.3}$$

where x and y are detector pixel indices. There are $X \times Y$ pixels in every PSF image and $n_{\mathrm{GATE}}(x,y)$ and $n_{\mathrm{VRT}}(x,y)$ are the number of counts in detector pixel (x,y) obtained with GATE and VRT respectively. $n_{\mathrm{GATE,max}} - n_{\mathrm{GATE,min}}$ is the range of counts in the PSF obtained by GATE. The average NRMSE over PSFs from all 36 positions (referred to as a PSF-set) is calculated for each of the fine voxel sizes tested for VRT. In this comparison, the voxel size of the coarse volume, which does not influence simulation accuracy but only affects simulation time, is fixed to be 1 mm. The detector pixel size is fixed at 0.5 mm for all PSF simulations.

2.2.5. VRT time-efficiency and coarse voxel size optimisation

To optimise the time-efficiency of VRT, the same PSFs as described in 2.2.4 are again simulated with the optimised fine voxel size for 6 different VRT coarse voxel sizes (see 2.2.2) and the simulation times are recorded. This way the coarse voxel size which resulted in the fasted simulation could be determined.

Subsequently, we compare the time-efficiency of VRT with optimised voxel settings to that of GATE. For a comparison, one has to choose a setting for the number of photons tracked in GATE. For the validation study, we track $5{\times}10^{10}$ photons at each point source position as this results in almost noiseless PSFs and can thus serve as a gold standard. If fewer photons are tracked, PSFs become noisier and thus starts to deviate from the gold standard. Although this deviation from the gold standard is due to different reasons than the deviation obtained with VRT (which can be due to neglect of physics processes, due to scatter, or due to discretisation effects) we choose to determine the relative time-efficiency of VRT compared to GATE, by comparing the time it takes for GATE to arrive at the same difference level from the gold standard as VRT (again characterised by NRMSE). To this end, PSF-sets from GATE simulations with a series of different numbers of emissions are generated and NRMSE from the gold standard is calculated for each of them. Moreover, as is mentioned in 2.2.3, GATE simulation results are blurred in energy and spatial domain with Gaussian kernels in order to mimic the desired energy and spatial resolution. The use of a kernel-based way of simulating resolution instead of picking a random detector position and energy value from the detector response function (a full MCS) is a way of accelerating MCS and it is very useful in case one is interested in noiseless PSFs. Throughout this paper, we use accelerated MCS to avoid too lengthy simulations, but in the time-efficiency comparison, we also provide acceleration factors of VRT with respect to full MCS, in which the interaction energy and position are, instead of blurred, randomised according to a 9%-FWHM and 3.2 mm-FWHM Gaussian distribution respectively. In our time comparison study, all simulations are executed on the same multi-CPU computer cluster, and 25 CPUs are used.

2.2.6. Projection image comparison

In MP-MBT, the scattered gamma photons from torso and breast can be detected by the gamma detector and if the energy of these scattered photons is within the photopeak window, they will usually add a rather continuous background to the projection image. As tracer uptake in organs is rather high in breast imaging, scatter is a topic of concern in molecular breast imaging and in some designs high energy resolution gamma detectors are used [55, 57, 58]. The amount of scatter that will be detected depends on the exact system's geometry and different studies have reported very different numbers [63, 114–119].

It is thus important to evaluate the influence of scatter in MP-MBT with a realistic anthropomorphic phantom. For this reason, we implement the well-known XCAT phantom with heart, liver, torso, and deformable breasts in the GATE simulation, see Figure 2.1 [120, 130, 131]. Instead of using dual-grid voxels, the voxel sizes of the XCAT phantom are fixed: the torso, including the heart and the liver, is voxelized to a 3.2 mm grid, and the breast is voxelized to a 0.8 mm grid. Two breast sizes are checked: a 400 mL breast compressed to a thickness of 55 mm (a common B-cup breast), and a 1300 mL breast com-

pressed to a thickness of 85 mm (a common D-cup breast). The latter breast is shown in Figure 2.1. To note, the distance between the two collimators is larger than the thickness of the breast because of the 7 mm thick compression plate. The tracer uptake that we assumed in different organs is listed in Table 2.1. These are typical numbers found in practice if 925 MBq ^{99m}Tc-Sestamibi is injected to the patient [63, 112, 113, 118, 132–134].

Table 2.1: Tracer uptake in different tissues

Tissue	**Uptake** (kBq/mL)
Breast	3.7
Torso	3.7
Heart	55.5
Liver	55.5

In GATE, the detected photons are categorised according to their origin and interactions they have undergone: they are listed to be either breast-emitted or torso-emitted, and scattered or non-scattered. This way we are able to divide the total energy spectrum into different categories in order to better pinpoint which photons cause possible differences with VRT. Moreover, we apply the widely acknowledged Triple-Energy Window (TEW) scatter correction method to GATE simulated projections, in order to check if the scatter can be estimated this way [135]. We set a ±10% photopeak window (126 — 154 keV), a 14 keV wide left side window (119 — 133 keV), and a 14 keV wide right side window (148 — 161 keV). For a certain detector pixel with N_L counts in the left side window and N_R counts in the right side window, scatter is then estimated to be

$$N_S = \frac{N_L + N_R}{2} \times \frac{28\ \text{keV}}{14\ \text{keV}} \times 0.6. \tag{2.4}$$

To note there is a factor 0.6 in Equation 2.4, which aims to make the total counts after TEW correction the same as acquired with VRT. In reality, when the number of scattered photons is not known one may base this number either on simulations or different values may be tested in an optimisation study. We subtract this scatter estimate from the simulated projections to obtain TEW-corrected projections. The occurrence of negative values in the projections is prevented by setting them to zero. Note that the comparison of VRT images with scatter-corrected GATE images is relevant to assess bias as in real scanners a TEW-based scatter correction method is commonly applied.

Full projection images (with scatter), scatter-free GATE projections, TEW-corrected GATE projections, and VRT projections of the same phantom scan are compared. To note, in the VRT simulations, only the compressed breast phantom is included while the torso phantom is neglected. Additionally, in generating projections, VRT only tracks the rays through the breast phantom (single-grid). The subsequent raytracing through the collimator (dual-grid) is done using previously acquired PSFs that were stored on disk. The transmission probability obtained from raytracing through the phantom is then multiplied by the corresponding collimator raytracing transmission factor. This gives exactly

the same results as a complete raytracing simulation from each activity containing voxel in the phantom through the collimator to the detector but is more efficient.

2.2.7. Image reconstruction

The comparison of PSFs and projection images allows to estimate how accurate VRT is in the noiseless case and to which extent the TEW method corrects for the bias caused by scattered photons. However, when simulating reconstructed images with realistic noise levels, neglecting scatter may also lead to an underestimation of noise in images as detector images of scattered photons are noisy themselves. To better investigate the impact of this, we also simulated a full scan of the 400 mL breast phantom with a 6.0 mm diameter spherical lesion inside (see Figure 2.5) using both GATE and VRT to obtain projection images. For normal breast tissue and organs we assume the realistic activity levels provided in Table 2.1 while the lesion uptake is taken to be 37 kBq/mL, 10 times as high in normal breast tissue. The total scan time is assumed to be 10 minutes. In case GATE is used to simulate projection images, the number of gamma emissions corresponding to the given activity levels and scan time are simulated. When VRT is used, noiseless projection images are generated (similar as described in 2.2.6) after which Poisson noise is applied. In order to be able to acquire 3D reconstructions, projection images are acquired for a total of 170 different positions of the sliding gamma detectors. Precise infor-mation on the positions used and other scan details can be found in [32].

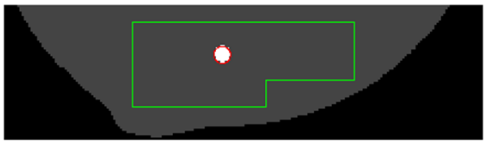

Figure 2.5: A slice of the XCAT breast phantom with a 6 mm diameter lesion inside. The red circle labels the lesion, and the green polygon marks the background.

The projections generated by either GATE or VRT are used as the input of a maximum likelihood estimation maximisation (MLEM) reconstruction algorithm, while the system matrix used in MLEM in both cases is generated by VRT. Data acquired from different gamma detector positions are all simultaneously taken into account in image reconstruction [121]. In case GATE-generated projections are used, TEW scatter correction is applied to compensate for scatter from the breast and torso. In that case, scatter images are obtained in the same way as in 2.2.6 but an additional Gaussian filter with 11.8 mm FWHM is applied to smoothen them. The reason to blur the scatter images is to limit the noise amplification due to TEW correction as is usually done [136, 137]. The scatter images are then added to the simulated projections in the denominator of the MLEM algorithm similar as summarised in [138]. Note that the size of the smoothing filter and the side windows chosen are not optimised in this study. While voxel size of the phantom in VRT and GATE simulations was set to 0.8 mm, voxel size of reconstructed images was 1.6 mm, in order to mimic a realistic continuous activity distribution.

Ten GATE simulations and ten noise realisations of VRT-simulated projections are used to generate reconstructed images. Besides visually comparing reconstructed images, we also compared the mean contrast of the lesion over the background, as well as the noise as standard deviation in the background. Figure 2.5 shows how we defined the regions used; the area inside the 6 mm diameter red circle is considered to be lesion area, while the area > 3 mm outside the red circle but still inside the green polygon is considered to be background area.

2.3. Results

2.3.1. VRT accuracy for generating PSFs

In Figure 2.6, an example PSF profile is shown for collimators parametrised by different fine volume voxel sizes. From this image, one can see that the setting of the fine voxel size influences the accuracy of generating PSFs, especially near the PSF's maximum. The counts of the GATE-generated PSF (considered to be the ground truth) are normalised to the total number of emissions of the point source (5×10^{10}) so that the total counts in a PSF represent the sensitivity of the scanner. No scaling factor needs to be applied to VRT-generated PSFs as solid angle is taken into account. As explained in the method section, photons that scatter in the collimator or scintillator and end up being detected in the photopeak are included in GATE-generated PSFs.

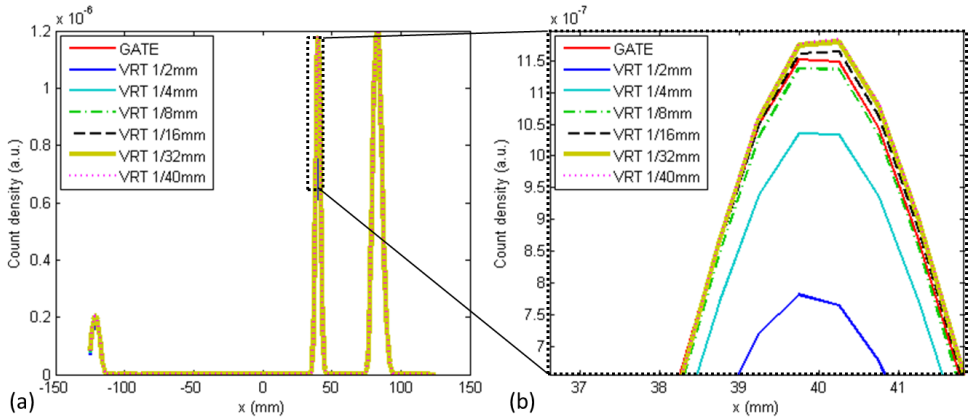

Figure 2.6: (a) Simulated PSF profiles for the cy3 location (see Figure 2.4). GATE generated PSFs and VRT generated PSFs using different fine collimator volume voxel sizes are shown; (b) is the enlarged view of the part of (a) in the black dotted box.

In Table 2.2, the differences between VRT-simulated PSFs and GATE-simulated reference PSFs are quantified by means of the NRMSE, averaged over the 36 point source positions. The maximum difference over the 36 positions is also provided. From the table, we can infer that the differences between VRT and reference PSFs become smaller when the fine

volume voxel size is decreased from 1/2 mm to 1/8 mm. Therefore we choose 1/8 mm to be the fine voxel size in subsequent simulations. For smaller voxel sizes the error does not decrease anymore and even slightly increases. This slight unexpected increase will be discussed later. In the current VRT simulation, every detector pixel is divided into 4×4 subpixels in the simulation. Without this subpixel approach, the NRMSE and maximum difference for the 1/8 mm fine voxel size increase to 0.230% and 11.83% respectively. Therefore, the subpixel approach does improve the accuracy of VRT and is also applied in the subsequent comparison.

Table 2.2: Comparison of different voxel sizes for the fine volume (coarse volume voxel fixes at 1 mm)

Fine volume voxel size (mm)	**Diff. from reference**	
	NRMSE (%)	Max. diff. (%)
1/2	0.601	33.13
1/4	0.234	11.21
1/8	0.143	5.07
1/16	0.140	5.32
1/32	0.150	6.34
1/40	0.151	6.18

Figure 2.7 shows several PSFs at different locations in the field of view obtained with GATE (reference) and VRT with the 1/8 mm fine voxel size setting. The profiles are shown on both linear and semi-logarithmic scale. These profiles confirm that GATE and VRT give very similar PSFs as could also be assessed from the numbers in Table 2.2.

It is worth noting that in the semi-log scale graphs (Figure 2.7b, 2.7e, and 2.7h), the amplitude of VRT-generated PSFs goes to zero at locations in between pinholes while GATE-generated PSFs do not. The reason that there is zero signal for VRT is the result of the applied cut-off described in 2.2.2, that results in raytracing being stopped when traversing more than 2.76 mm of collimator material. In GATE, such a cut-off is not applied and as scattered photons are included there can be a signal in any detector pixel. By analysing the simulation results, we found that the signal in between pinholes is mainly caused by gamma photons that undergo multiple interactions in the scintillator. In this situation, the total energy deposition can still be within the ±10% photopeak meaning that these photons are included, and the interaction position is estimated at the centroid of different interaction positions. Note that the signal in between pinholes is extremely small showing that all though VRT only includes detector scatter by adapting the NaI attenuation coefficient, it is well able to simulate MP-MBT including resolution degradation due to multiple scatter in the scintillator.

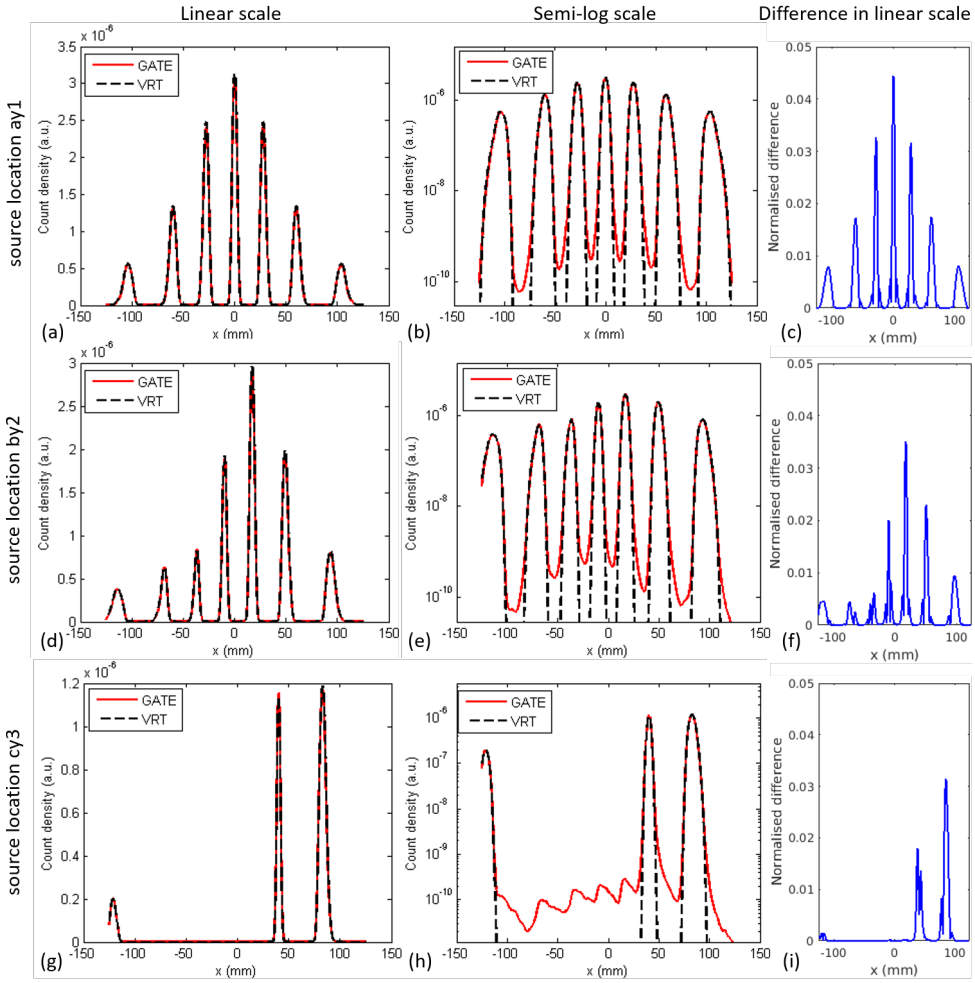

Figure 2.7: Central PSF profiles obtained with GATE and VRT for optimised fine voxel size of 1/8 mm. Gamma source is at location ay1 (a)–(c), by2 (d)–(f), and cy3 (g)–(i) in Figure 2.4. PSFs on linear scale and semi-log scale are shown, as well as the difference plots between VRT and GATE normalised to the maxima of GATE-simulated PSFs.

2.3.2. VRT time-efficiency optimisation

While the accuracy of VRT is only determined by the fine voxel size, the time-efficiency also depends on the coarse voxel size. In Table 2.3, the simulation time of VRT (total time required for obtaining the 36 PSFs) for different settings of the coarse volume voxel size is listed. A coarse voxel size of 2 mm is optimal in terms of computational speed and we therefore choose 2 mm as the coarse voxel size for this scanner in subsequent simulations. Table 2.3 also confirms that the accuracy of VRT remains the same once the fine voxel size is fixed.

Table 2.3: Comparison of different voxel sizes for the coarse volume (fine volume voxel fixes at 1/8 mm)

Coarse volume voxel size (mm)	**Time in VRT** (s)	**Diff. from reference** NRMSE (%)
1/4	122	0.143
1/2	67	0.143
1	38	0.143
2	24	0.143
3	41	0.143
5	65	0.143

To determine the relative speed of VRT compared to GATE, one has to set the number of emissions that has to be simulated in GATE. If the number of emissions decreases, PSFs become noisier and there is a difference to the reference (almost) noiseless PSFs with 5×10^{10} emissions simulated. The number of emissions that have to be simulated by accelerated (blurred) and full GATE to obtain the same difference level from the gold standard as VRT is 1.5×10^{7} and 1.3×10^{9} emissions respectively. For this number of emissions, VRT with optimised coarse voxel size is 337 times faster than accelerated GATE and 29300 times faster than full GATE. However, one should note that the sources of the deviation from the reference PSF are different: in GATE deviations are caused by stochastic noise, while in VRT they are due to the minor residual mismodelling of the system.

2.3.3. Projection image comparison

Phantom representing 400 mL-breast

Figure 2.8 shows energies of detected photons for the XCAT phantom simulation. Energy spectra are separated into different parts determined by the origin of the gamma photons ('breast' or 'torso') and the types of interactions they undergo before being detected ('scatter' or 'no scatter'). Here 'scatter' refers to both Compton and Rayleigh scatter in the phantom and collimator, while single scatter and multiple interactions in the scintillator are always included in all simulations. We did not distinguish between 'torso scatter' and 'torso no scatter' in the figures because the 'torso no scatter' fraction is too small to be visible in the whole detector spectrum. Figure 2.8a corresponds to the left detector (i.e. the detector closest to the liver, see Figure 2.1), and Figure 2.8b corresponds to the right detector. The scatter fraction (the amount of gamma photons scattered in the phantom or collimator that get detected in the ±10% photopeak window) is about 20% on both detectors. The torso fractions (the amount of gamma photons originating from the torso) are 4% and 9% in the photopeak on the left and right detector respectively.

Projection images obtained by GATE and by VRT for the same phantom are shown in Figure 2.9 and Figure 2.10, as well as the profiles marked in white. In these images, a scatter-

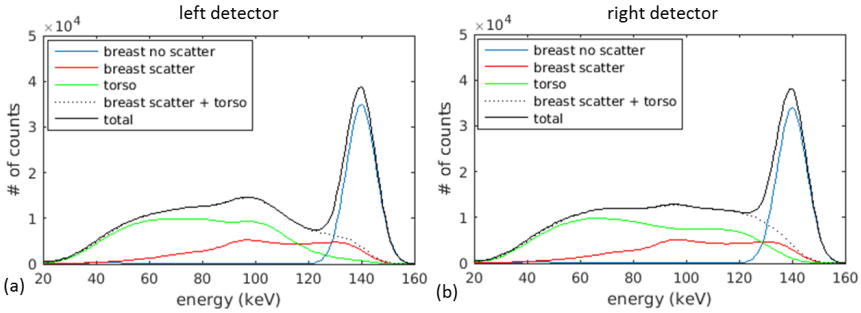

Figure 2.8: Energy spectra for the MP-MBT detectors obtained from GATE simulations of the 400 mL-breast.

free projection (by simply ignoring photons that scattered in phantom and collimator) and a TEW-corrected projection are shown as well. The projection pattern from the pinholes can clearly be distinguished. These pinhole projections are non-overlapping, because of the design of the shielding plate in between the multi-pinhole collimator and detector. Note that in these projection images only part of the detectors is used because these images are for the smaller (400 mL) breast. The projections from VRT are very similar to those from the scatter-corrected GATE projections and, as expected, scatter-free GATE projections. Since the TEW-corrected projections and the VRT-generated projections are very similar, the difference is hardly visible on the same colour scale. Therefore, we provide the same difference images shown in different colour scale in the supplementary material.

Phantom representing 1300 mL-breast

In Figure 2.11, the same energy spectra as in Figure 2.8 are shown for the larger (1300 mL) breast. Corresponding projections and profiles can be found in Figure 2.12 and Figure 2.13. Like for the 400 mL-breast, the scatter fraction in the ±10% photopeak window is about 20% on both detectors. The torso fractions are 4% and 7% in the photopeak on the left and right detectors respectively.

In contrast to the projections for the smaller breast shown in Figure 2.9 and Figure 2.10, in Figure 2.13 there is a discrepancy between the GATE projections and the projections simulated by VRT. To understand the cause of the difference, it is important to note that the TEW-corrected GATE projection is very close to the scatter-free GATE projections. Apparently, scatter can be well corrected for with the TEW method and the photons missed by VRT are not scattered photons but primary (non-scattered) photons. We come back to this issue in the discussion session.

In Table 2.4, the differences between the TEW-corrected projection image and the VRT projection image are quantified in terms of NRMSE for both breast sizes. The maximum differences are listed as well. The NRMSE and maximum difference in the 1300 mL- right breast are especially large, which reflects the discrepancy in Figure 2.13.

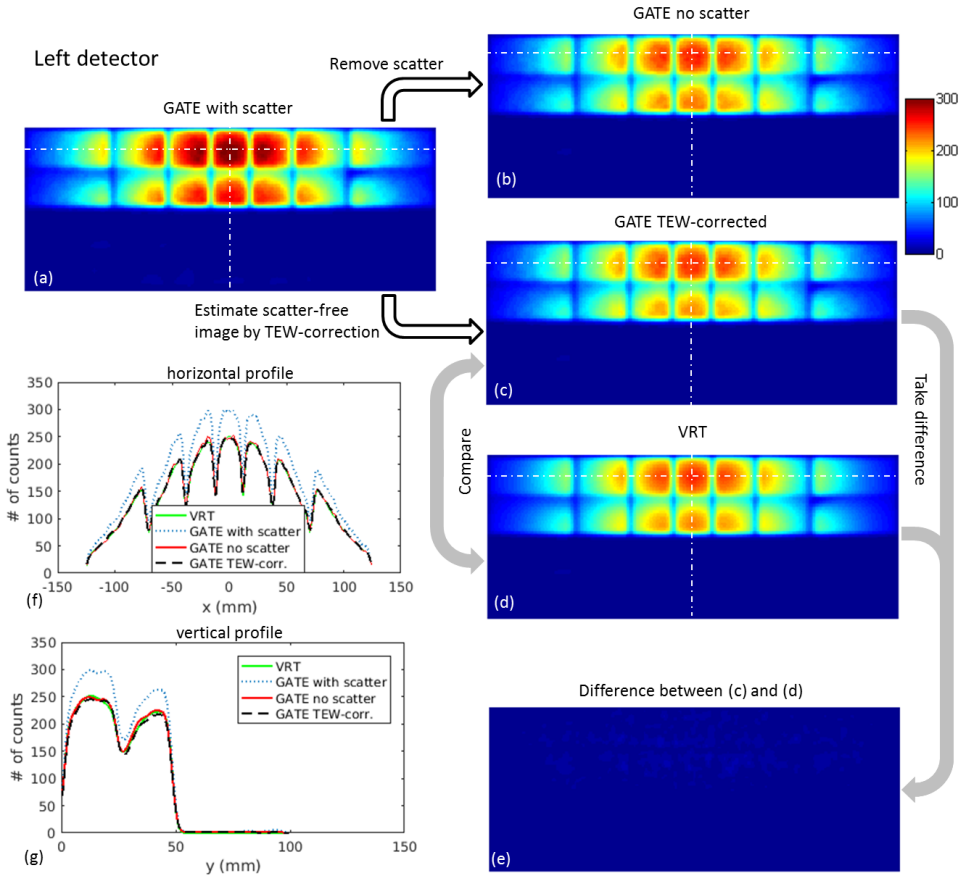

Figure 2.9: Left detector projection images of the GATE simulated XCAT phantom with the 400 mL-breast. (a) Full projection with scatter and torso signal; (b) projection without scatter (treated as ground truth for photons scattered in the phantom and collimator); (c) scatter-corrected projection using the TEW method; (d) the projection obtained with VRT (only breast phantom); (e) difference between VRT-generated projection and scatter-corrected projection. (f) and (g) are the horizontal and vertical profiles marked in white in (a)—(d).

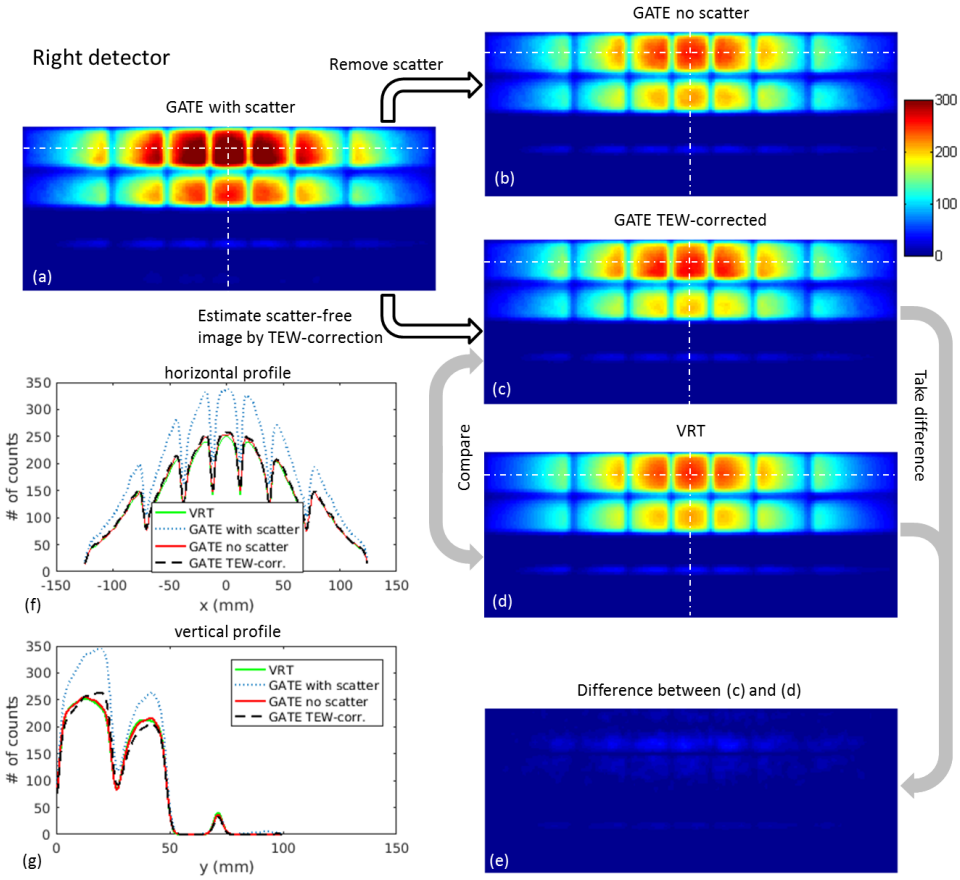

Figure 2.10: Right detector projection images of the GATE simulated XCAT phantom with 400 mL-breast. (a) Full projection with scatter and torso signal; (b) projection without scatter (treated as ground truth for photons scattered in the phantom and collimator); (c) scatter-corrected projection using the TEW method; (d) the projection obtained with VRT (only breast phantom); (e) difference between VRT-generated projection and scatter-corrected projection. (f) and (g) are the horizontal and vertical profiles marked in white in (a)–(d).

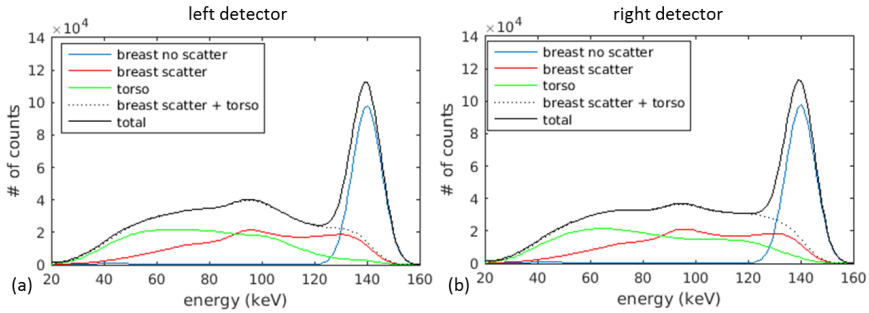

Figure 2.11: Energy spectra for the MP-MBT detectors obtained from GATE simulations of the 1300 mL-breast.

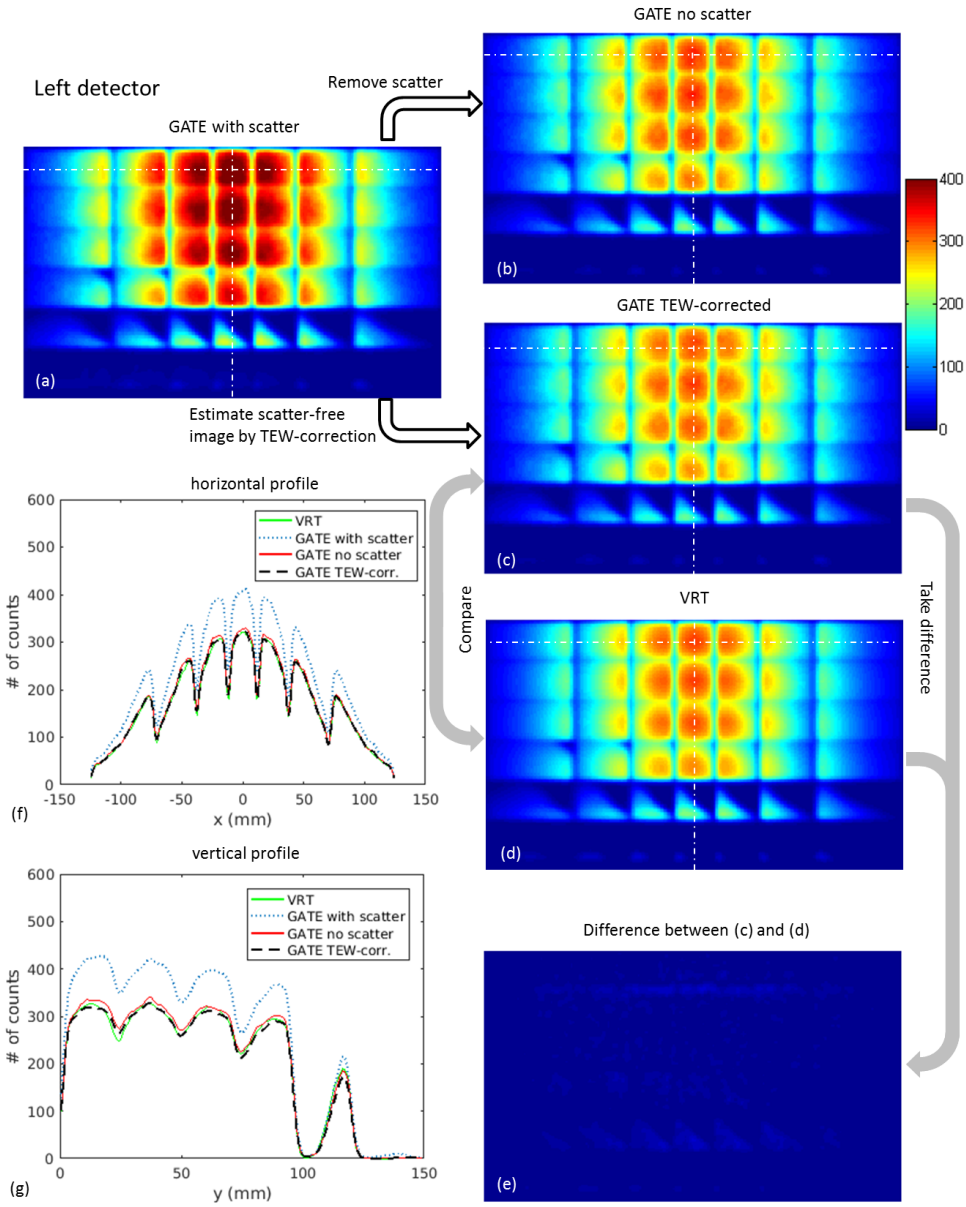

Figure 2.12: Left detector projection images of the GATE simulated XCAT phantom with the 1300 mL-breast. (a) Full projection with scatter and torso signal; (b) projection without scatter (treated as ground truth for photons scattered in the phantom and collimator); (c) scatter-corrected projection using the TEW method; (d) the projection obtained with VRT (only breast phantom); (e) difference between VRT-generated projection and scatter-corrected projection. (f) and (g) are the horizontal and vertical profiles marked in white in (a)–(d).

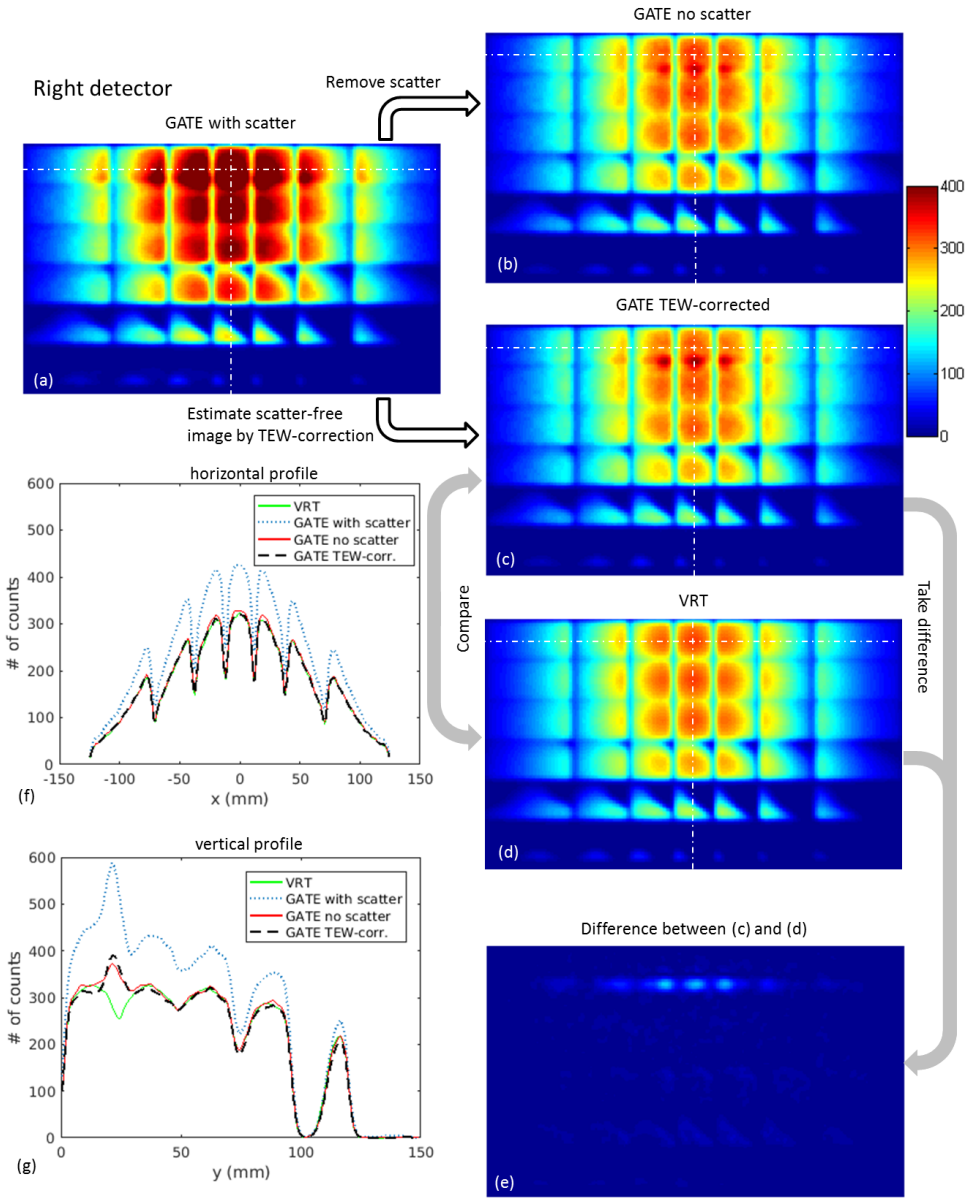

Figure 2.13: Right detector projection images of the GATE simulated XCAT phantom with 1300 mL-breast. (a) Full projection with scatter and torso signal; (b) projection without scatter (treated as ground truth for photons scattered in the phantom and collimator); (c) scatter-corrected projection using the TEW method; (d) the projection obtained with VRT (only breast phantom); (e) difference between VRT-generated projection and scatter-corrected projection. (f) and (g) are the horizontal and vertical profiles marked in white in (a)–(d).

2.3.4. Reconstructed images

Figure 2.14 shows the same slice (3.2 mm thick) through reconstructed images obtained from (a) GATE-simulated projections, and (b) VRT-generated noisy projections. TEW

Table 2.4: Comparison of projection images

Projection image	Diff. from reference	
	NRMSE (%)	Max. diff. (%)
400 mL left	1.08	5.26
400 mL right	2.44	15.08
1300 mL left	1.37	8.53
1300 mL right	2.43	32.85

scatter correction is applied in case GATE-simulated projections were used. These images are post-filtered by a 3D Gaussian filter of 3 mm FWHM. Visually, reconstructions from GATE-simulated projections with TEW correction applied and from VRT-generated noisy projections appear very similar. The profiles between the two green lines in Figure 2.14a and 2.14b are shown and compared in 2.14c. Similar images from different noise realisations can be found in the appendix Figure 2.16.

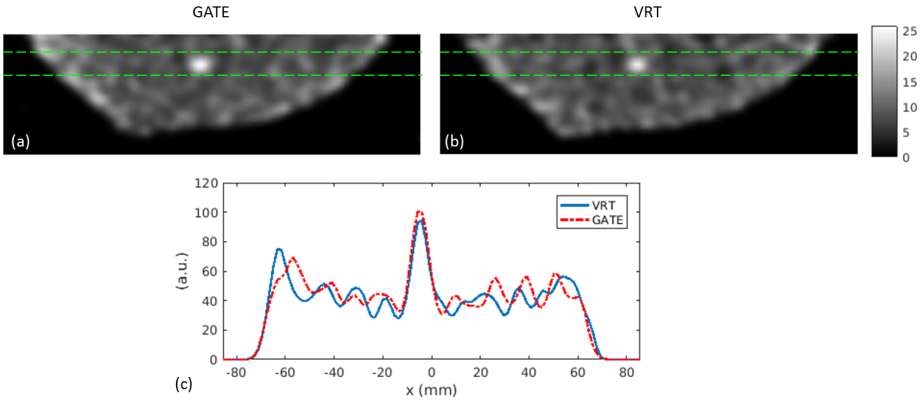

Figure 2.14: Slices through MLEM reconstructed images with 20 iterations used obtained with the two methods. Images are obtained from (a) GATE-simulated projections with TEW scatter correction used in reconstruction, (b) VRT-generated noisy projections. The profiles between the two green lines are plotted in (c).

As noisy images cannot be directly compared as was done for noiseless projections, we also assess noise and contrast in reconstructed images for ten sets of GATE-simulated projections with TEW-correction and ten noise realisations of VRT-simulated projections. The average contrast and noise of the lesions and backgrounds are provided in Table 2.5, as well as the standard deviation over different noise realisations. There is no significant difference in the numbers for the different methods.

Table 2.5: Comparison of reconstructed images

	GATE	VRT
contrast	1.36±0.20	1.40±0.24
noise	0.193±0.015	0.200±0.011

2.4. Discussion

From the PSF profiles in Figure 2.6 and Figure 2.7 and the differences displayed in Table 2.2, it is clear that the PSFs from GATE and VRT (at 1/8 mm fine voxel) agree very closely. Note that initially when the fine voxel size in VRT is decreased, the PSFs acquired by GATE and VRT become more similar as one would expect. However, for voxel sizes below 1/8 mm the difference goes up slightly. From this, we conclude that for such very small voxel sizes the difference between GATE and VRT is not dominated by the discretisation effect anymore and thus we deemed a fine voxel size of 1/8 mm to be sufficiently small. We do not have an exact explanation for the increasing difference between GATE and VRT for smaller voxel sizes. The small residual differences (on average 0.14%) may be caused by (i) the reference GATE simulation not being completely noiseless, or (ii) photons that scattered in collimator or detector.

Together with the 1/8 mm fine voxel size which is necessary for simulation accuracy, we find that a coarse voxel size of 2 mm led to the highest simulation speed. The optimal coarse voxel size strikes a good balance between two extremes. When it is too large, the number of mixed voxels increases and thus much more rays have to be tracked on the fine collimator grid: in the extreme situation in which the whole collimator plate is made out of a single coarse voxel, VRT will have to look into the fine volume for every photon path and the dual-grid method is actually not used. On the other hand, if the coarse voxel size is very small, raytracing on the coarse voxel grid itself is already slow and completely dominates simulation time. We have shown that with the optimal coarse voxel size, VRT could reach the same difference level from the reference PSFs 337 times faster than accelerated GATE or 29300 times faster than a full GATE MCS.

Note that the VRT voxel size combination of 1/8 mm and 2 mm is 'optimal' for the current collimator and detector geometry. For a different collimator or scanner, there might be better combinations. However, from our experience, as long as the thickness of the collimator/shielding plate is an integer multiple of the coarse voxel size, and the pinhole diameter does not change very much, the optimal dual grid setting should stay the same. Furthermore, up to now, we have only tried a dual-grid collimator representation. It is possible to use full octree-structure grids to represent the collimator which may lead to higher time-efficiencies. However, finding the optimal setting for a multi-grid approach is beyond the scope of this research, since the time-efficiency for VRT with the current setting is already good enough for us as with these settings, as noiseless system matrices could be generated in minutes. Compared with other raytracing SPECT simulators in which collimators are defined by analytical shapes [92, 93, 96, 98, 130], the advantage of VRT is that geometries that are hard to describe analytically can be easily implemented. Furthermore, a design drawing of a collimator can be directly voxelized to a volume that can be used in raytracing. The disadvantage is that it requires some trial and error to determine the voxel size (combination) that provides a satisfactory discretisation error

and acceptable computational speed.

While the PSF simulations show that in principle VRT is an accurate and fast simulator, they do not consider scattered gamma photons from the human body which can play a major role in clinical imaging and is ignored in VRT. In real scanners, projection images contain scattered photons which are usually corrected for prior to reconstruction or in the iterative reconstruction process. The TEW method is a simple and popular scatter estimation method. Thus, to accurately predict the performance of a real MP-MBT system, the projection images from VRT are supposed to closely resemble TEW-corrected images. In the projection images and profiles in Figure 2.9 and Figure 2.10, we show that for the 400 mL-breast, TEW-corrected GATE projections and VRT projections are very similar, and an NRMSE of about 1% is found. However, for the 1300 mL-breast, a discrepancy is encountered. A comparison with scatter-free GATE projections reveals that the discrepancy is not due to scatter (as TEW-corrected GATE images very closely resemble scatter-free GATE images). In Figure 2.15a, a zoom-in view of Figure 2.1, it can be seen that some gamma photons from the liver directly reach the right detector through the first row of pinholes. We checked this by removing the torso phantom and acquiring the same projection image as in Figure 2.13. In the vertical profile of this projection, shown in Figure 2.15b, the VRT generated profile agrees very well with the scatter-corrected GATE-generated profile. On the left detector, such an issue is not observed as there is no organ on the cranial side of the body that has ^{99m}Tc-Sestamibi uptake as high as the liver. Note that in principle VRT can simulate direct activity from the torso so this finding does not disqualify VRT as an accurate simulator of MP-MBT. However, in this paper we only simulate photons originating from the breast. Thus, the lesson learnt is that when designing such a system one has to consider direct paths from the torso to the detector, and these have either to be taken into account in the simulator or the geometry has to be adapted as to avoid these paths.

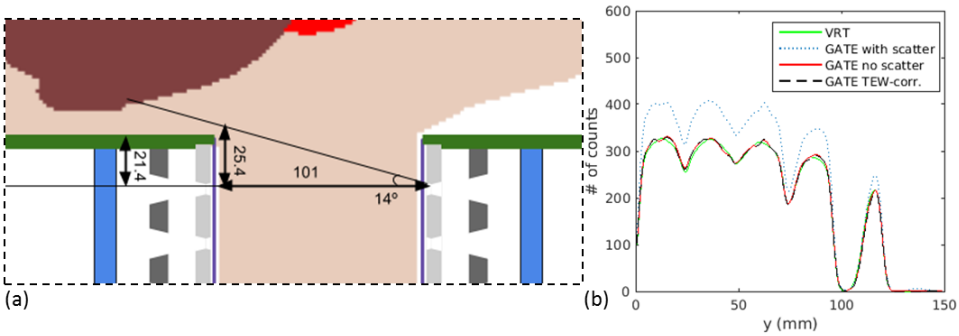

Figure 2.15: (a) An enlarged view of the MP-MBT system for the 1300 mL-breast phantom (see Figure 2.1); through the first row of pinholes, gamma photons from part of the liver can directly be detected by the right detector. (b) A vertical profile of the right detector projection (the same as Figure 2.13g) in which the torso phantom is removed from GATE simulation; the mismatch in VRT and the scatter-corrected GATE projections disappears.

As stated above, neglecting Compton scattering in VRT is acceptable with our speci-

fied MP-MBT geometry as Compton-scattered photons can be corrected for with a TEW method even though we use a conventional NaI(Tl) gamma detector with a moderate energy resolution of 9%. This minor contribution of Compton scattering to breast images agrees with an earlier work on planar compressed breast imaging with a parallel hole collimator [118] although other papers have indicated different results [114, 116]. The reason for the rather small ratio of scattered photons in the photopeak despite the high tracer uptake in the heart and liver probably lies in the fact that gamma photons from the torso have to be scattered by a rather large angle in order to be redirected in the direction of the gamma detector. Large-angle scatter is generally associated with a large energy loss and thus the majority of these scattered photons can be rejected because they are detected outside the photopeak window. Although in many studies nowadays semiconductor detectors are used, it is shown here that the energy resolution of NaI(Tl) is sufficient for this application.

Note that the fact that VRT can accurately simulate TEW-corrected projections means that we can correct for the bias caused by scatter. However, there is another aspect to scatter that VRT cannot correct for which is the added noise level due to the scattered photons. Therefore, we also simulated reconstructed images based on either GATE-simulated projection or VRT-generated images. Visual inspection as well as contrast-noise characteristics show that images obtained with both methods were very similar, further indicating that VRT can be used to predict the quality of simulated images. As computation time for such images is considerable we only simulated reconstructed images for the 400 mL breast size, but as the scatter fraction is similar for the larger breast our results indicate that the neglect of scatter in VRT is also acceptable for these larger breast sizes. However, in the case larger breast simulation, direct paths from liver to detector either have to be modelled in image reconstruction or prevented by a slight change in design. Note that on the left side of the reconstructed breast images from GATE, there is a slight increase of signal compared to VRT images. We believe that such bias can be removed by tuning the size of the scatter windows and the amount of blurring of the scatter projections. This, however, is beyond the scope of this paper because we have just tested one setting of these parameters, but may be the subject of future research. We chose TEW for scatter correction because of its simplicity and because it is one of the most commonly used approaches in the clinic [138, 139]. There are of course other more advanced scatter estimation techniques [138], which can also be implemented in practice. However, in this paper, we focus on proving that VRT can be used to generate realistic simulated images and testing out different scatter correction techniques is beyond the scope of this paper.

2.5. Conclusion

VRT can accurately simulate the proposed MP-MBT system with more than four orders of magnitude better time-efficiency than full MCS. Ignoring scatter in VRT is feasible because the amount of scatter in the photopeak is limited in our pinhole collimator-based MP-MBT geometry and can thus be corrected. However, direct gamma photon paths between liver and gamma detector can exist for large breast sizes and have to be carefully considered in design and simulation. VRT can be very useful in evaluating geometries for MP-MBT.

Acknowledgement

We thank Dr. William Paul Segars from Duke University for kindly providing the XCAT phantom for this research.

Appendix

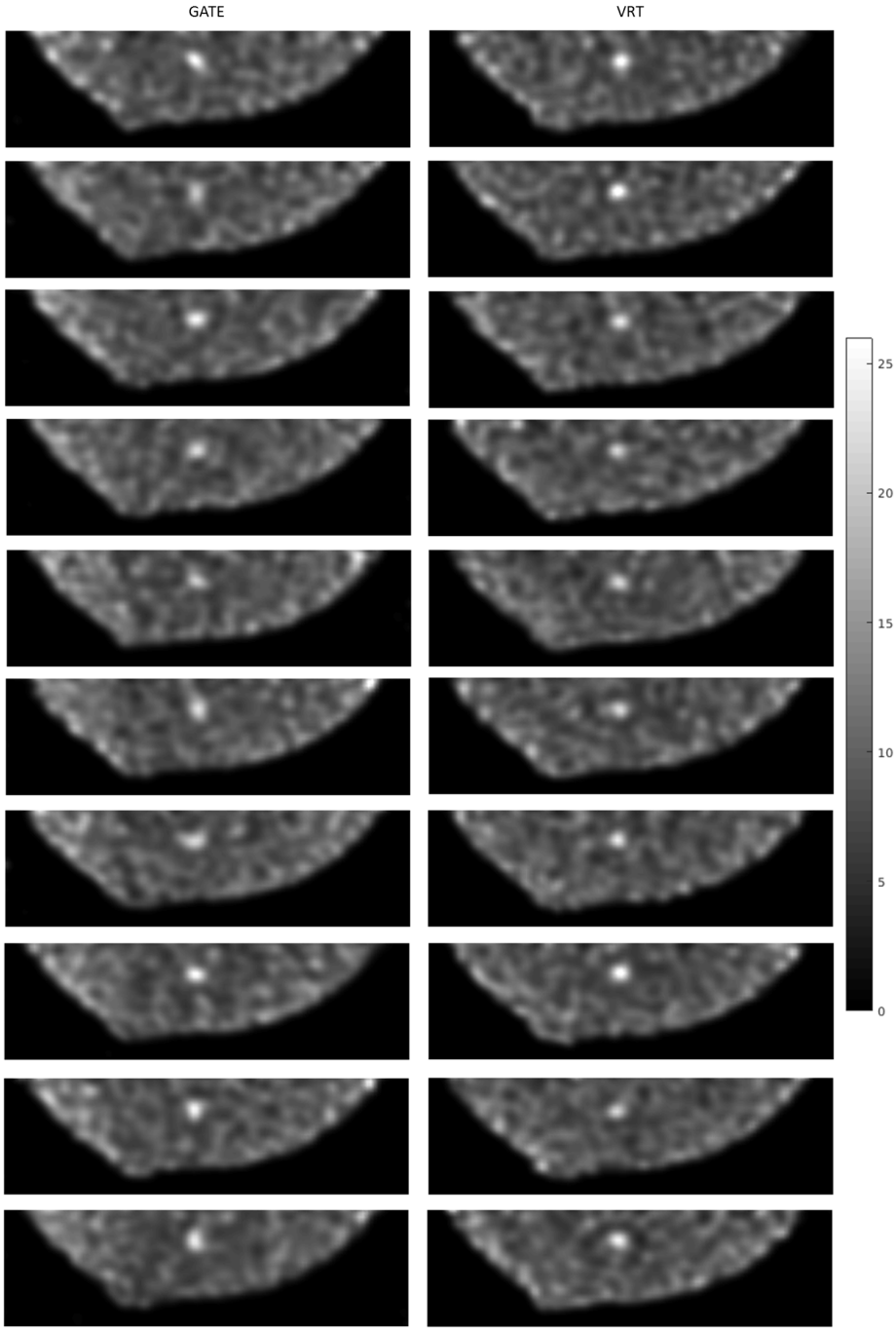

Figure 2.16: Reconstructed images similar as in Figure 2.14 for all simulated noise realisations.

3

Simulation of novel light-guide-PMT geometries to reduce dead edges of a scintillation camera

This chapter is adapted from:
Beien Wang, Rob Kreuger, Freek J. Beekman, Marlies C. Goorden. *Novel light-guide-PMT geometries to reduce dead edges of a scintillation camera*, Physica Medica — European Journal of Medical Physics **48** (2018), 84-90 [140].

Anger cameras based on monolithic NaI scintillators read out by an array of PMTs are predominant in planar gamma imaging and SPECT. However, position estimation of gamma interactions is usually severely degraded near the edges of the scintillator which can be extremely undesirable for applications like breast imaging.

Here we propose a relatively cost-effective solution based on the use of scintillators with absorptive edges with an unconventional light-guide-PMT layout employing a maximum likelihood positioning algorithm. The basic design on which we aim to improve consists of a monolithic NaI(Tl) scintillator read out by 3×5 square PMTs (conventional layout, CL) that could be suitable for molecular breast imaging. To better detect gamma interactions near the crystal's critical edge, we tried different set-ups: we replaced the 5 large PMTs near the edge by 11 smaller PMTs (small-sensor layout, SSL); we emulated rectangular PMTs along the critical edge by inserting a row of 5 rectangular light-guides that direct the light toward square PMTs placed behind (shifted layout, SL); we inserted rectangular light-guides alternatingly, such that the PMTs are in an interlocking pattern (alternating shifted layout, ASL).

The performance of our designs was tested with Monte Carlo simulations. Results showed that SSL, SL, and ASL gave better spatial resolution near the critical edge than CL (3.4, 3.6, and 4.1 mm near the edge compared with 5.3 mm for CL), and thus resulted in a larger usable detector area. To conclude, for applications where small dead edges are crucial, our designs may be cost-effective solutions.

3.1. Introduction

Gamma detectors that deliver information on the interaction position and energy of incoming gamma photons are key elements in nuclear medicine scanners. Both in planar scintigraphy and in SPECT, gamma detectors based on continuous NaI(Tl) scintillators that are read out by an array of photomultiplier tubes (PMTs), usually referred to as the Anger camera, have been predominant for decades. In Anger cameras, the gamma photon's interaction position and its energy are conventionally estimated using Anger logic [49], which is based on calculating the centroid of the PMT outputs. Anger logic has become popular because it can be simply implemented with a resistor/capacitor network and Anger logic combined with heuristic linearity and non-uniformity corrections provides satisfactory position and energy estimation results in most applications. Unfortunately, the positioning linearity and spatial resolution are usually poor near the scintillator's edges, a situation often referred to as the dead edge effect. This effect has implications for the usable field-of-view of a gamma camera which is smaller than the scintillator's surface.

Although reducing dead edges is almost always profitable to enhance the usable detector surface and thus the system's sensitivity, in whole-body SPECT the presence of dead edges is usually accepted because with the large-area detectors that are commonly applied, the size of the dead edges is relatively small and because not using the detector's

edges does not have to lead to image artefacts. However, in other applications, the use of the detector's edges can be absolutely necessary in order to arrive at useful images. Examples of this include planar breast imaging [30, 61] and a dedicated multi-pinhole molecular breast tomosynthesis (MP-MBT) technique proposed in our group [32, 46]. In the proposed MP-MBT scanner, a woman is lying prone on a patient bed with her breast pendant in a hole in the bed. The breast is mildly compressed and two gamma cameras are placed on either side of the breast close to the chest wall. In simulations, such a design resulted in a tumour-to-background contrast-to-noise ratio $2 - 3$ times higher than commercial planar scanners. The edge area of the detector in this design is used to image the part of the breast close to the chest wall. However, in conventional Anger cameras, the dead edge roughly equals the PMT radius and as most common PMTs are two or three inches in diameter, about 25 mm or 40 mm at the edges would be unusable if we would employ a standard Anger camera in MP-MBT. Therefore, a detector with small dead edge is essential for MP-MBT.

To improve positioning linearity near the edges, several solutions have been proposed over the years. In some cases, PMTs were extended over the edges of the scintillator both for continuous crystals [141] and pixelated or semi-pixelated scintillators [142–144]. However, in MP-MBT there is no room for such a placement of PMTs since the scintillator extends till the patient bed. Another option is to read out the continuous crystals with smaller light sensors, including position-sensitive PMTs [145–147], avalanche photodiodes [148, 149], silicon photomultipliers [150, 151], charge-coupled devices [152], or to use a combination of pixelated scintillators and these small light sensors [153–157]. However, using small light sensors instead of PMTs for large surface gamma detectors (such as in MP-MBT, 240×140 mm^2 area) leads to enormously increased costs. A third option is to use semiconductor gamma detectors instead of scintillation-based detectors. These detectors transfer gamma energy directly into an electrical signal and are already applied in several dedicated breast scanners [55, 158]. Besides being able to reduce dead edges, semiconductor detectors improve energy resolution over scintillator detectors, although several studies have shown that the benefit of this in dedicated breast scanners is limited [54, 115, 117, 118]. However, like small light sensors, the use of semiconductor detectors significantly increases the gamma camera's costs over those of the Anger camera.

Besides using new detector materials or advanced light sensors, several algorithms to better decode the scintillation position from the light distribution in PMT-read out scintillators have been proposed, e.g. maximum likelihood estimation [159, 160], chi-squared error estimation [161], the k-nearest-neighbour method [150], a Gaussian filter algorithm [152], advanced light model fitting [146, 149], and different machine learning algorithms [148]. These decoding processes are more sophisticated and also more computationally demanding than weighted averaging, as is done in Anger logic, but they have been proven to be more effective in resolving scintillations near the edges. These algorithms are often used together with black-edge detectors which use absorbing material at the sides

of the scintillator [141, 144, 146, 147, 160]. Such absorptive edges increase the position dependence of the light spread near the edges, and thus improve position estimation in these areas.

Inspired by several of the above-mentioned elements, the aim of this paper is to propose a novel gamma scintillation detector design that has a cost comparable to that of the Anger camera but has improved spatial resolution and positioning linearity near the edges. This is achieved by using smart light-guide-PMT geometries to emulate smaller light sensors near the edges and by using a black-edge scintillator combined with a maximum likelihood (ML) positioning algorithm. PMTs used have a square shape in order to optimally cover the rectangular scintillator. Different designs are evaluated using Monte Carlo simulations.

3.2. Methods

3.2.1. Gamma detector designs

Detector dimensions are chosen such that they are suitable for the MP-MBT scanner proposed in our group [32, 46] which has a minimum requirement for the active detector area of 240×140 mm^2 and the scintillator thickness is 9.5 mm. We test four different designs in a simulation study which all fulfil the minimum dimension requirement.

The first design (Figure 3.1a), which is the most basic (therefore dubbed 'conventional layout', CL) comprises a 240×180×9.5 mm^3 NaI(Tl) scintillator, a 14 mm thick glass light-guide, and 15 Hamamatsu R6236 PMTs (60×60 mm^2 square PMTs with 54×54 mm^2 photocathodes) [162]. The entrance surface of the scintillator is painted white (reflective) while the edges are black (absorptive). As a comparison, we will also show some results for the same design but with a white-edge scintillator. Note that in our design, PMTs placed at the right and left sides of the gamma detector partly extend over the edges. In this way, the left and right edges are effectively read out by half-sized PMTs which is expected to improve resolution and linearity in these edge areas [141]. However, at the upper edge which is assumed to be the critical edge of the detector, such an approach is not feasible as there is no space to allow for this (this is the edge placed close to the patient's chest wall).

An alternative to CL could be the use of smaller PMTs, e.g. Hamamatsu R1548-07 (24×24 mm^2 square PMTs with (2×)8×18 mm^2 photocathodes [162]), which is the second design tested ('small-sensor layout', SSL; Figure 3.1b). In that case, 21 PMTs would be needed to cover the 240 mm long upper edge. As the price per PMT is approximately constant, the costs for PMTs would increase by 40% while the scintillator size would be reduced to 240×144 mm^2. In principle, smaller PMT sizes are only required in the direction perpendicular to the edge and one would thus like to use rectangular PMTs if these would be com-

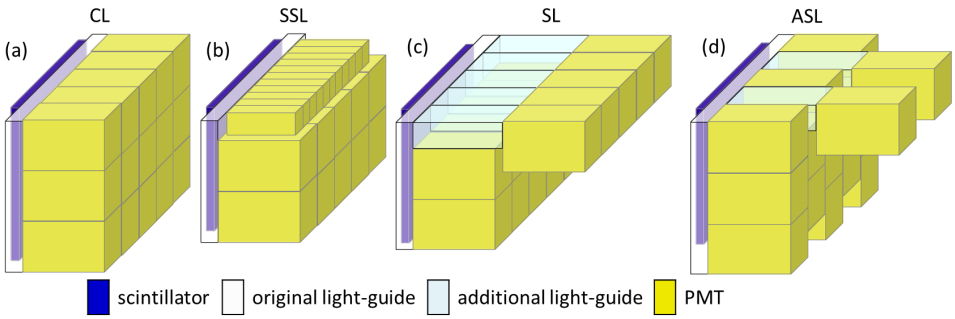

Figure 3.1: The four gamma detector designs tested in this paper. The scintillator, light-guide and PMTs are shown schematically for (a) CL, (b) SSL, (c) SL and (d) ASL.

mercially available for the same price. As this is not the case, we propose an alternative design: the 'shifted layout' (SL, Figure 3.1c). In this layout, an additional light-guide, with a cross-section that is half the PMT area, is inserted in between the original light-guide and each of the upper row PMTs. The additional light-guides are covered by Lambertian reflectors like Polytetrafluoroethylene (PTFE) with 98% reflectivity [163]. The length of the additional light-guide is assumed to be 160 mm, longer than the length of the PMTs (123 mm). The light-guide is assumed to be borosilicate crown glass. A variant on SL is the 'alternating shifted layout' (ASL, Figure 3.1d), in which the additional light-guides still exist, but the PMTs are placed in an interlocking layout instead of in a conventional grid. Because the second light-guide is half as wide as the PMT front face, the scintillator sizes for SL and ASL are both 240×150 mm^2. We come back to this reduced area in the discussion section.

3.2.2. Simulations

The performance of our gamma detector designs is assessed by the well-validated Monte Carlo simulation software GEANT4 Application for Tomographic Emission (GATE) [76, 77, 128]. The optical surface parameters in GATE are tuned in such a way that the simulator gives the best agreement with our available clinical Anger camera with 3-inch round PMTs. Here we simulate square PMTs, and we assume the light propagation in the new setups remains valid. In Table 3.1 the relevant parameters used in the GATE simulations are listed.

The refractive index of the white reflector was set to 1.0 which reflects the presence of an air gap between the white reflector and the scintillator/light-guide. Furthermore, low reflectivity as reported in [166, 167] is assumed which is representative for high-quality black edges because it has been reported that the quality of the black absorber is crucial in the black-edge scintillation camera performance.

To assess spatial resolution and positioning linearity, NEMA suggests to put lead masks

Table 3.1: Settings in simulation

Parameter in GATE	Status
Photoelectric effect	`StandardModel`
Compton scatter	`StandardModel`
Optical simulation	`Scintillation`, `OpticalAbsorption`, `OpticalRayleigh`, `OpticalBoundary`
Photocathode	Efficiency: 0.29 [162]
Black absorber	Reflectivity: 0.05, refractive index: 1.8
White reflector	Lambertian reflection, reflectivity: 0.98, refractive index: 1.0
Interface (scintillator to light-guide)	Roughened
Scintillator (NaI(Tl))	Density: 3.67 g/cm^3, light yield: 38000 photons/MeV, intrinsic energy resolution: 5% [164, 165], refraction index: 1.85
Light-guide (glass)	Density: 2.50 g/cm^3, refraction index: 1.50, absorption length: 3.11 m

with thin parallel slits on the gamma detector and irradiate them with gamma rays from a source placed at a relatively large distance above the detector to approximate parallel rays perpendicularly directed towards the detector surface [168]. In this way, the line response function (LRF) from each slit is obtained, and from these LRFs, positioning linearity and spatial resolution in horizontal and vertical directions are measured. In GATE this measurement is simulated by irradiating the gamma detector with vertical and horizontal line sources of 140 keV gamma photons (energy of ^{99m}Tc gamma emission). Gamma emitters are evenly distributed in the infinitely thin lines (as is shown in the solid black lines in Figure 3.2) and all gamma photons are emitted perpendicular to the detectors. The interval between two neighbouring lines is 10 mm, and the outer horizontal and vertical lines are all 2 mm from the edges of the scintillator.

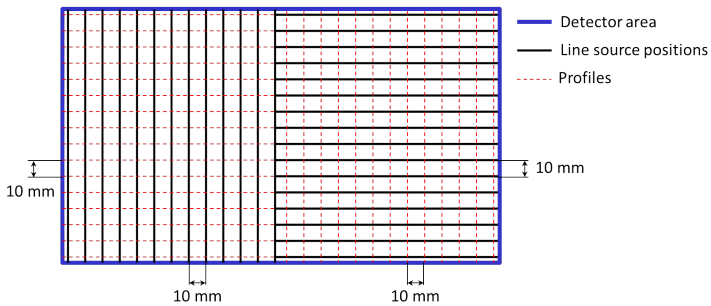

Figure 3.2: Line sources irradiate the gamma detector. The left part of the detector is irradiated by vertical line sources (marked by solid black lines) while the right part of the detector is irradiated by horizontal line sources. The profiles of the LRFs are taken at every intersection of the solid black lines with dashed red lines.

To obtain the light collection map and linearity correction map for Anger logic estimation, the gamma detectors are also irradiated by point sources of 140 keV gamma photons, and the point response functions are determined. From each point source, about

2000 gamma photons are emitted perpendicular to the gamma detector's surface. These gamma point sources are placed in a grid of 5 mm interval over the whole detector.

To apply ML estimation, a series of reference PMT outputs, i.e. the expected number of optical photons detected by each PMT for all possible scintillation locations, should be obtained. These reference PMT outputs are extracted from the PRF simulation. The light collection spectrum of each point source is obtained and the interactions in the ±10% window around 140 keV are averaged and then taken as reference PMT outputs. In this case, the reference PMT outputs also include scatter in the photopeak. Then reference PMT outputs are obtained at a 1 mm grid by cubic interpolation of the 5 mm-interval reference PMT outputs and used for ML estimation.

3.2.3. Data processing

We use GATE simulation results to generate a list of gamma photon detections, in which the number of optical photons sensed by each PMT (the PMT output) in every interaction is recorded. These data are then contaminated by simulated readout noise which is Gaussian distributed with zero mean and a full-width at half-maximum (FWHM) of 6 photons. This noise level is estimated based on the measurement from readout electronics in our lab. We use this list of data as the input to Anger and ML position estimation. Anger logic is implemented as an output-weighted average of PMT coordinates. To improve Anger estimation resolution, a threshold is applied to each PMT output. Only the PMTs with outputs above the threshold are used in the weighted average process. The threshold in our case is set as 3% of the total summed PMT output at every detection. We apply a linearity correction as is commonly done for Anger cameras in the same way as described in [169] with linearity correction map obtained from the PRF data.

The ML positioning algorithm is based on the assumption that if the gamma photon's energy and the interaction position are fixed, the number of scintillated optical photons detected on each PMT ($\mathbf{n} = [n_1\ n_2\ \cdots\ n_M]$, M PMTs in total) is Poisson distributed [160]. Of course the readout noise is not Poisson-distributed, but as its FWHM of 6 photons is less than 5% of the mean PMT output, using a Poisson distribution is a tolerable approximation in this case. If the Poisson mean of the output of PMT m ($\bar{n}_m(x,y)$) for a gamma photon of a certain energy is known for every possible gamma interaction location, one can write the probability that an interaction occurring at location (x,y) resulted in output $\mathbf{n}$ as:

$$\Pr(\mathbf{n} \mid x,y) = \prod_{m=0}^{M} \frac{[\bar{n}_m(x,y)]^{n_m}}{n_m!} e^{-\bar{n}_m(x,y)}. \tag{3.1}$$

Note that in this equation we do not take the dependence of the PMT outputs on the depth of interaction in the crystals into account, rather $\bar{n}_m$ represents an average over different depths. In this work, the mean outputs $\bar{n}_m(x,y)$ were obtained by interpolat-

ing simulated PRFs, as is described in 3.2.2. The most likely gamma photon interaction location $(\hat{x}, \hat{y})$ is the one that maximise Equation 3.1:

$$(\hat{x}, \hat{y}) = \arg\max_{x,y} \{\Pr(\mathbf{n} \mid x, y)\}. \tag{3.2}$$

In practice, the logarithm of $\Pr(\mathbf{n} \mid x, y)$ is maximised which simplifies the calculation and gives exactly the same result.

The searching strategy used in this paper to obtain the most likely interaction position is a contracting-grid algorithm based on the one described in [170]. This method can quickly search for the target in a multi-dimensional space by dividing the search into grids of different intervals, and as long as $\bar{n}_m(x, y))$ is a smoothly changing function of location, it should give the same result as an exhaustive search. The initial search is done on a coarse grid such that the target's rough location is obtained. Later on, with the found rough location as the starting point, this search is repeated on an ever finer grid. Though the search is exhaustive in every grid, the total time complexity is much less than exhaustively searching the whole range in the fine grid. The grids used here are:

- 5-by-5 grid with 13 mm interval;
- 5-by-5 grid with 5 mm interval;
- 3-by-3 grid with 3 mm interval;
- 3-by-3 grid with 2 mm interval;
- 3-by-3 grid with 1 mm interval.

So in total 77 iterations are required for every detected interaction and the searching range is 52×52 mm^2. The starting point is the Anger estimated position. The resulting images will have a pixel size of 1 mm.

3.2.4. Performance evaluation

In order to evaluate the gamma camera's performance, we use the LRFs to determine positioning linearity and spatial resolution, and PRFs to obtain the total light collection and the energy resolution. To note, the energy resolution here is not calculated from the energy spectrum but from the light collection spectrum: a histogram of the total number of photons collected (sum of all PMT outputs) for each interaction.

Spatial resolution in this paper is obtained by fitting a Gaussian function to the LRFs and then determining its FWHM. To obtain information on how spatial resolution varies over the detector, profiles (one pixel-width; 1 mm) of the LRFs are taken along all dashed red lines in Figure 3.2 which have 10 mm spacing. For visualisation purposes, we then interpolate the spatial resolution distribution on the whole detector to 1 mm intervals. Spatial resolution in horizontal and vertical directions ($R_{\mathrm{i}x}$ and $R_{\mathrm{i}y}$) is presented separately, and we also calculate an 'averaged' spatial resolution by determining the root-mean-square

(RMS) in both directions: $R_{\mathrm{i}xy} = \sqrt{(R_{\mathrm{i}x}^2 + R_{\mathrm{i}y}^2)/2}$. Energy resolution ($R_{\mathrm{i}E}$) is defined to be the FWHM of a Gaussian fit to the light collection spectrum divided by the mean of the fit (given as a percentage) at each point source position.

As postulated by NEMA [168], positioning linearity of the detectors is given by differential linearity which is defined as the standard deviation of every estimated LRF in the direction perpendicular to the lines. Finally, we also provide the usable field-of-view (UFOV) of the different designs which we define as the area where $R_{\mathrm{i}xy}$< 5 mm.

3.3. Results

3.3.1. Black-edge gamma detector and ML algorithm

In Figure 3.3, the LRFs obtained with the CL are shown for a white-edge scintillator read out by (a) Anger logic and by the (b) ML algorithm, and (c) for a black-edge scintillator employing the ML algorithm. LRFs are only shown on half the detector surface because of the horizontal symmetry of the layout. It is clear that if a scintillator with white reflecting edges is used, a significant part near the scintillator's edges is not usable (about 30 mm from the upper and lower edges, and 15 mm from the left and right edges), even if ML estimation is used. With Anger estimation (3.3a), the lines near the edge pile up inwards to about half a PMT-size from the edge, while with ML estimation (3.3b), the lines up to a distance of half the PMT size from the edge are severely blurred and cannot be distinguished anymore. For the black-edge detector with ML estimation (3.3c), the position estimation at the edge is much improved compared to 3.3a and 3.3b, though at the corners resolution is clearly reduced. Anger estimation on a black-edge detector is not an option because a weighted average algorithm would give even poorer positioning linearity with the lower number of sensed optical photons on the near-edge PMTs [171].

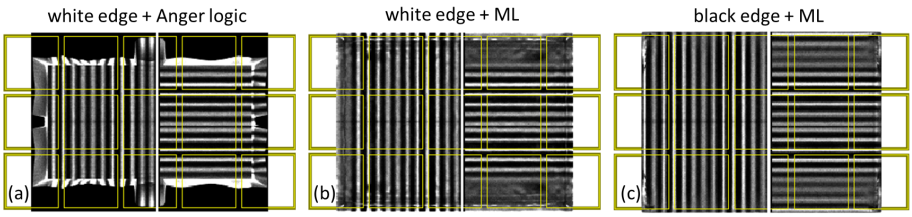

Figure 3.3: The LRFs of the CL with different edge treatment and positioning algorithm combinations. The yellow squares in the figures mark the effective area of the PMTs. The critical camera edge is the upper edge.

For the same conventional detector layout, Figure 3.4 shows three example light collection spectra obtained for (a) the white-edge detector and (b) black-edge detector at three example locations (centre, edge, and corner). Clearly, the total number of optical photons collected depends on where in the scintillator the gamma interaction took place; more optical photons are collected for events in the centre compared to events near the

scintillator's edge (5 mm to one edge in this example) and corner (5 mm to two edges). This effect of varying light collection over the scintillator is much stronger when black absorptive edges are used; in that case edge scintillations have almost 50% less light collection than in the centre while in the corners the light collection is reduced by about 65%. For the white-edge detector, the largest light loss is about 30% at the corner of the detector, but as the edges and corners of white-edge detectors cannot be used and the light collection at edges of the usable area is the same as in the centre, in practice a global light collection window is usually set for subsequent scatter rejection [135]. From the spectra, one can conclude that a global light collection window is not applicable in black-edge scintillation detectors.

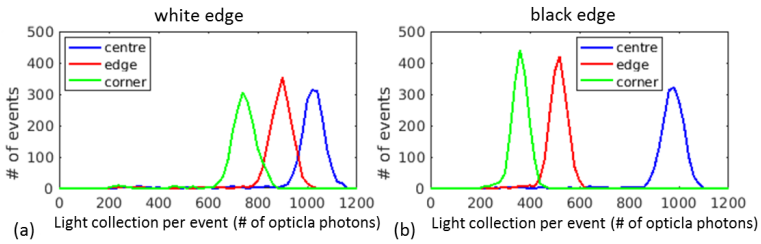

Figure 3.4: Example light collection spectra for CL with scintillators with (a) white edge and (b) black edge treatments. Three typical positions are tested: centre, edge (5 mm to one edge of the scintillator), and corner (5 mm to two edges of the scintillator). These spectra were obtained by simulating an irradiation with 2000 gamma photons per position.

3.3.2. Different detector layouts

In Figure 3.5, simulation results for all PMT layouts are compared. All of the four detectors have black edges and positioning is thus done with ML estimation. For the same reason as in Figure 3.3, LRFs on only half of the detector area are shown. From the LRFs in Figure 3.5e—h, spatial resolution maps in horizontal (3.5i—l) and vertical (3.5m—p) directions are calculated. The light collection maps shown in 3.5q—t are obtained from the PRFs. It can be seen that the four layouts have similar resolution in horizontal direction (about 3.6 mm on average), but that SSL, SL, and ASL show better resolution in vertical direction close to the upper critical edge (3.4 mm, 3.6 mm, and 4.1 mm up to 30 mm to the critical edge compared to 5.3 mm in CL). For SSL and SL, the places with poor resolution are all near the lower edge, while for ASL, they are more spread over the detector area. For all four detector designs, light collection at the centre of the detector is higher than that at the edge.

In Table 3.2, the mean spatial resolutions in horizontal and vertical directions (R_{ix} and R_{iy}) over the whole detector obtained from Figure 3.5i—p are listed. The differential linearity (lin.) in horizontal and vertical directions is calculated from the LRFs 3.5e—h. The UFOVs are determined by R_{ixy}< 5 mm. The centre, edge (< 8 mm from an edge), and corner (< 8 mm from two edges) mean energy resolutions (R_{iE}) are calculated (see 3.2.3).

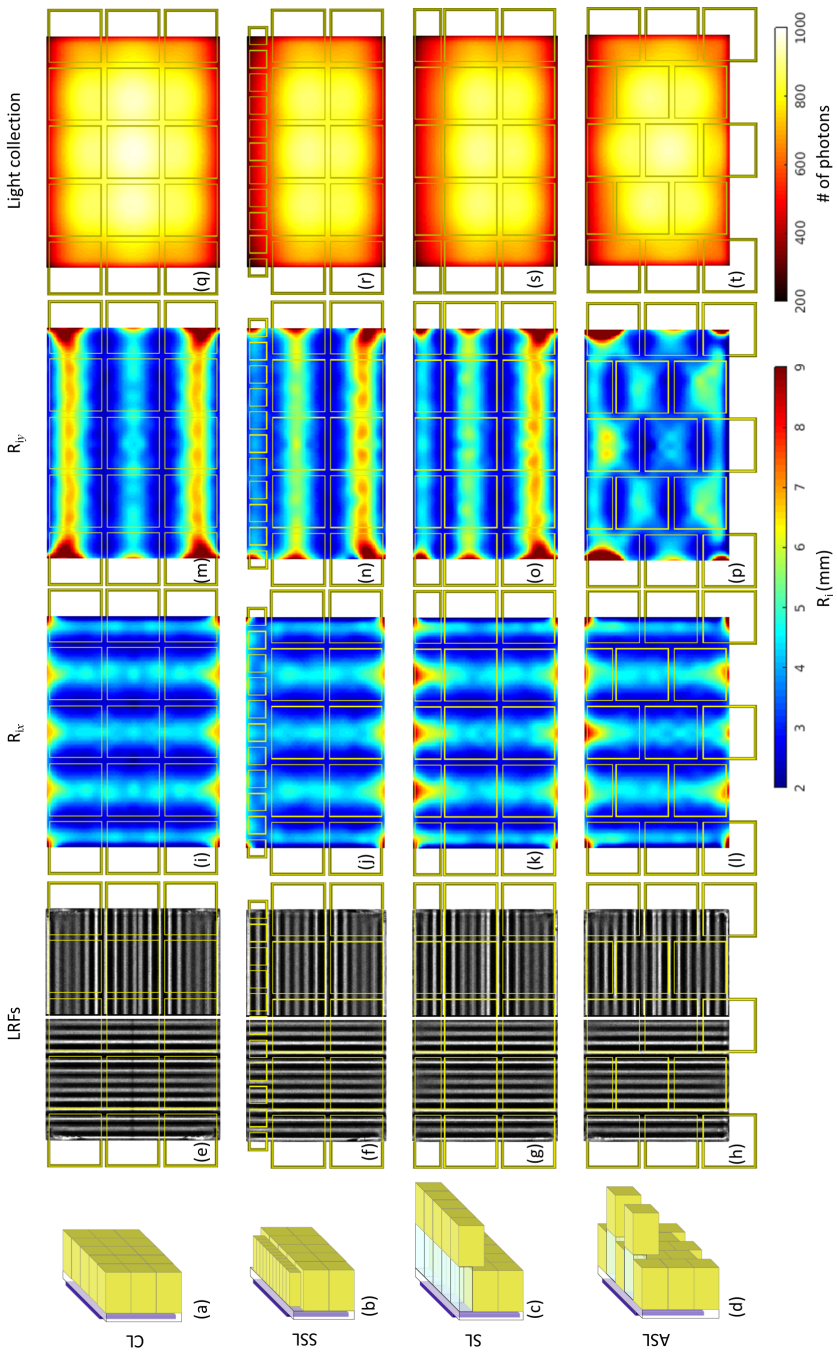

Figure 3.5: The LRFs, spatial resolution in horizontal and vertical directions (R_{1x} and R_{1y}), and light collection of the four gamma detector layouts. The yellow rectangles in the graphs mark the effective area of the PMTs. The energy resolution maps are not shown but the representative values are provided in Table 3.2. All four layouts are black-edge detectors using ML estimation.

Table 3.2: Spatial resolution, positioning linearity (lin.), UFOV, and energy resolution obtained for the four different layouts

	CL	**SSL**	**SL**	**ASL**
R_{ix} (mm)	3.54	3.58	3.70	3.67
R_{iy} (mm)	4.31	4.28	4.19	3.85
lin.x (mm)	0.10	0.11	0.11	0.12
lin.y (mm)	0.27	0.21	0.18	0.17
UFOV (%)	81.5	86.4	84.1	90.0
R_{iE} centre (%)	11.6	12.1	12.1	11.9
R_{iE} edge (%)	14.4	15.4	15.1	14.7
R_{iE} corner (%)	16.4	17.6	16.8	16.1

3.4. Discussion

From Figure 3.3 it is clear that the use of black absorptive edges and ML estimation can largely improve positioning linearity near the edges compared with a traditional white-edge detector with Anger logic positioning, though the spatial resolution near the edges is still rather poor. For all four layouts in Figure 3.5e—h, significant distortion in LRFs is not observed except in the corners. The distorted area in the three non-conventional layouts is smaller than that in the CL, which is also reflected by the spatial resolution-defined UFOV in Table 3.2. In the simulation study of MP-MBT [32] we assumed that the dead edge of the detector was 5 mm, and SSL, SL, and ASL seem to be able to achieve this goal as the LRFs nearest (2 mm) to the scintillator edges are resolved. Note that the SSL, SL and ASL result in shorter detectors than the CL, as we keep the same number of rows of PMTs and the MP-MBT application only requires a 140 mm long detector. If one would like to compare different designs at equal detector area, one has to add an extra row of PMTs to the non-conventional designs resulting in a larger part of the scintillator being covered. Adding another row of PMTs would require five more PMTs for SL or SSL, and two more PMTs for ASL. The performance of such extended detectors can be predicted through vertical symmetry: PMT layouts in the UFOV of (180 mm long) extended detectors are vertically symmetric, thus we can simply mirror the upper 90 mm of the resolution map down to roughly predict the resolution in the lower 90 mm. This is still an estimation as the lower edge should have better resolution than suggested by simply mirroring as no additional light-guide would be needed there. For extended SL, the vertical and horizontal resolutions are 3.84 mm and 3.76 mm, and for extended ASL, they are 4.05 mm and 3.66 mm. For SSL, such symmetry does not exist, so the performance cannot be predicted. Table 3.3 estimates the usable area per PMT of different layouts including the two extended layouts (240×180 mm^2).

Although the CL detector surface is larger than the other three simulated layouts, the actual usable area is not always much different (see Table 3.3): the actual usable area (the

Table 3.3: Usable area per PMT of different designs

	CL	SSL	SL	ASL	Extended SL	Extended ASL
# of **PMTs**	15	21	15	15	20	17
UFOV (%)	81.5	86.4	84.1	90.0	91.2	89.7
UFOV (%) / **PMT***	5.4	4.1	5.6	6.0	4.6	5.3
Actual usable area (mm^2) / **PMT***	2347	1422	2018	2160	1970	2279

* The extended (240×180 mm^2 size) detector performance is estimated from vertical symmetry instead of an extra Monte Carlo simulation.

number of PMTs multiplied by the actual usable area per PMT) in SSL (21×1422 mm^2) is 85% of CL (15×2347 mm^2); SL's usable area (15×2018 mm^2) is also 86% of that of CL; ASL (15×2160 mm^2) has a usable area that is 92% of that of CL. From the quotations we got, the cost of an additional light-guide, and the extra cost of the 160 mm longer detector box would make the whole gamma detector (scintillator + PMTs + readout electronics + detector box) price increase by less than 4% when ASL is constructed compared to CL. Other solutions, e.g. applying small light sensor, scintillator pixilation, and using semiconductor detectors are usually much more expensive. For example, according to the online price of SiPMs [172], using SiPMs to cover a detector surface as large as ours will be 5 times as expensive as using PMTs, resulting in a doubling of the total detector price. This estimate does not even include the costs for extra electronic readout channels.

From the spatial resolution maps in Figure 3.5i—p, it is clear that the spatial resolution is always best in the interstices of PMTs, while it is the poorest in the centres of PMTs, especially in the centres of PMTs near edges. Such a phenomenon is also observed in other detectors using ML estimation or Anger logic [160, 161] and it is not difficult to understand: in scintillator detectors, position estimation accuracy depends on the sensitivity of the light distribution (PMT outputs in this case) to the exact interaction position and the total amount of light collection. In the centres of PMTs, light spread is not that sensitive to the scintillation position, while in the interstices, a subtle position change already leads to large light spread changes, i.e. PMT output changes; in the centres of the near-edge PMTs, PMT outputs are the least location-sensitive and the total photon collection is smaller than in the centre of the detector; therefore, the spatial resolution is worst in these places. The purpose of designing ASL is to reduce the number of large PMTs at the edges and avoid continuous low-resolution regions, e.g. PMTs at lower rows in SSL and SL (Figure 3.5n and 3.5o). Note that the light collection above the centres of the PMTs is higher than in the interstices. We believe that a trade-off between light collection and the sensitivity of PMT outputs to the exact interaction position may result in the minor fluctuations in the top row of the spatial resolution map for ASL (e.g. there appear to be two poor resolution centres close to the PMTs' centre).

An issue with the proposed designs may be the light collection loss due to the black edges. In Figure 3.5q—t a reduced light collection near the edges is clearly observed, as well as

in Figure 3.4 in which the difference between black- and white-edge detectors is obvious. For the three unconventional designs Table 3.2, the energy resolution in the central region of the detectors is always poorer than for the CL. This is because the centre-to-edge ratio in the CL is the highest, so that the black edges absorb less scintillated light from the central part of the detector. As a result of black edges, a global energy window over the whole detector, as is in most Anger cameras, is not suitable. Instead, a scintillation-position-dependent energy window could be applied, as long as the PMT outputs are sufficiently distinct in different interaction positions for different amounts of energy deposition. An efficient way for energy windowing might be to apply a rough (localised) energy window based on the Anger estimated scintillation location.

Furthermore, in the simulation, the attenuation of optical photons in light-guides is assumed to be the attenuation of borosilicate crown glass [173]. For the additional light-guides inserted in front of the upper row of PMTs, the attenuation of the 160 mm glass, the absorption in the PTFE reflector, and the absorption at the transitions of different materials result in about 20% less light collection on the PMTs attached compared to directly mounting PMTs to the 14 mm-thick light-guide. This light loss leads to poorer energy resolution at the upper edge (see Figure 3.5s). Additionally, poorer photon statistics degrades the spatial resolution in SL and ASL, as is specially obvious in the middle of the second row of PMTs. Such a deterioration of spatial resolution compared to CL is also observed in SSL, which we believe is probably because of the of lower fill-factor of smaller PMTs (0.5 instead of 0.8 for the R6236 PMTs).

In the current study both the calibration and the line source test are based on the same Monte Carlo simulations, which is an 'ideal' situation while in practice the exact response of scintillator, light-guide and PMTs may be unknown. We have tried to keep experimental practicality into mind. For example, the simulated processes of obtaining the PRFs and LRFs are not impractical, as they are based on NEMA recommendations for actual measurements, as is mentioned in 3.2.2. Also some realistic non-ideality is created as we interpolate calibration PRFs simulated on a 5 mm grid to a smaller 1 mm grid. However, in practice there may be some scatter in the mask for calibration and the collimated gamma beams are wider than in the simulations where we assumed infinitely small points sources, e.g. a width of about 1 mm is common. As the FWHM of PRFs is mostly 2 — 4 mm, we expect that this effect is not too large. Also, the mechanical and electrical stability of the system is not included in the simulations. However, from our experience with Anger cameras (470×590 mm^2 NaI scintillator readout by 3 inch PMTs), the mechanical parts can be produced rather reliable (0.01 mm motion error), and the electronics (especially PMTs) perform consistently for years after the first few days run-in period. The breast detector should not be more fragile than other existing systems.

3.5. Conclusion

The black-edge ASL gamma detector using ML estimation proposed in this paper can be a cost-effective solution for better resolving the dead edges. SSL and SL give better spatial resolution near the critical edge, but the resolution in other parts of the detector is compromised. As a drawback of using black edges, the light collection over the detector will be non-uniform, which requires extra work to apply a position-dependent energy window. Experimental tests have to be done to assess the real performance of the new design and confirm the results of this paper.

4

Experimental validation of a gamma detector with a novel light-guide-PMT geometry to reduce dead edge effects

This chapter is adapted from:
Beien Wang, Rob Kreuger, Jan Huizenga, Freek J. Beekman, Marlies C. Goorden. *Experimental validation of a gamma detector with a novel light-guide-PMT geometry to reduce dead edge effects*, IEEE Transactions on Radiation and Plasma Medical Sciences **4** (2019), 98-107 [174].

PMT-based scintillation cameras are still predominant in molecular imaging, but have the drawback that position estimation is severely degraded near the edges (dead edge effect). This leads to sensitivity losses and can cause severe problems in applications like molecular breast imaging and in certain SPECT devices. Using smaller light sensors or semiconductor detectors can solve this issue but leads to increased costs. Here we present a gamma detector based on standard PMTs with a novel light-guide-PMT geometry that strongly reduces dead edges. In our design, a monolithic NaI(Tl) scintillator is read out by square PMTs placed in a staggered arrangement. At the edge of the scintillator we inserted additional light-guides to emulate half-size PMTs. Detector performance was assessed for ^{99m}Tc imaging; an average spatial resolution of 3.6 mm was measured over the whole detector, degrading to 4.0 mm within 30 mm to the critical edge. The dead edge of the scintillator is < 3 mm. Since a 12 mm seal was used, the overall dead edge is < 15 mm, which is a significant improvement over conventional Anger cameras (~4 cm dead edge). Therefore, the presented geometry can be useful in creating economical gamma detectors with reduced dead edges.

4.1. Introduction

Gamma detectors used in nuclear medicine are mostly based on NaI(Tl) scintillators read out by an array of photomultiplier tubes (PMTs) that estimate the gamma interaction positions using Anger logic [49]. These gamma detectors, often referred to as Anger cameras, give satisfactory position and energy resolution, have good detection efficiency, and are relatively cost-effective. However, Anger cameras also have the drawback of poor spatial linearity and resolution at the scintillator's edges, which is often referred to as the dead edge effect [141, 175, 176]. Although not being able to use the whole scintillator surface always has the drawback of sensitivity loss, it is accepted in most clinical whole-body SPECT scanners in which the rotating Anger cameras are large and not using the edges of the cameras does not automatically lead to artefacts. In contrast, in some applications, dead edges as large as in conventional Anger cameras (roughly 4 cm which corresponds to the radius of the PMTs) are completely unacceptable. For example, in some dedicated cardiac SPECT systems, multiple relatively small stationary gamma camera modules are closely surrounding the chest in order to increase count yield from the heart on which they focus [45, 144], and large dead edges will result in large gaps between active detector areas and thus compromised sampling completeness. Additionally, in molecular breast imaging, in which the detectors are put close to the chest wall [57, 177], the use of conventional Anger cameras will result in being unable to image breast tissue near the chest.

To improve spatial resolution and linearity near the edges, current solutions mostly involve using small light sensors (e.g. position-sensitive PMTs, silicon photomultipliers) and/or scintillator pixelisation [68, 142, 144–147, 149–152, 157, 178, 179]. Semiconductor gamma detectors which convert gamma energy directly into electric signal are also an

option to reduce dead edges and these have already been applied in some applications [45, 180–184]. However, all these solutions come at a significant increase in costs compared to Anger cameras read out by conventional PMTs [140].

To find a cost-effective solution to the dead edge problem, we conducted a simulation study [140], in which we investigated several gamma detector designs based on a continuous NaI(Tl) scintillator with absorptive painted edges (so-called black edges), read out by square PMTs placed in different geometries, all using a Maximum Likelihood (ML) algorithm for position estimation [160]. Parameters in this simulation study were chosen with a multi-pinhole molecular breast tomosynthesis scanner (MP-MBT) in mind which we are currently constructing. In this MP-MBT one edge of the gamma camera (referred to as the critical edge throughout this paper) has to be placed close to the patient's chest wall [32, 33, 140] and large dead edges as common in Anger cameras are not acceptable at that edge. A spatial resolution similar to that of Anger cameras is sufficient in our application as we employ pinhole magnification. From the simulation study, we found that with PMTs placed in a staggered arrangement, facilitated by an additional light-guide (Figure 4.1a), a satisfactory positioning accuracy over the detector surface could be obtained (average horizontal and vertical spatial resolution 3.67 mm and 3.85 mm respectively) while resolution loss near the edge was diminished (average horizontal and vertical spatial resolution in region 30 mm from the critical edge: 3.82 mm and 4.14 mm). In this paper we present an experimental validation of this design using a prototype that has been constructed in our lab.

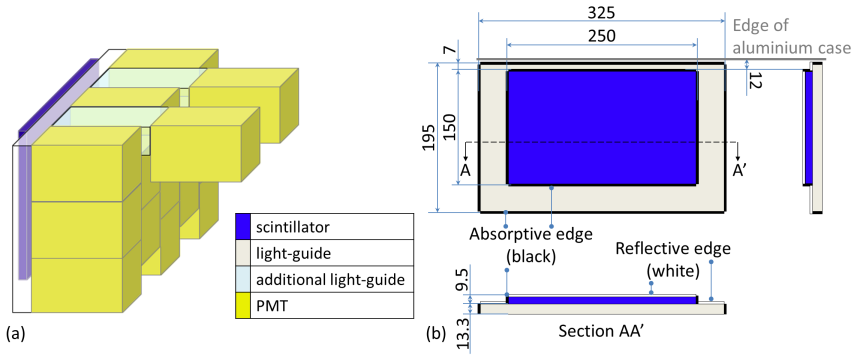

Figure 4.1: (a) A 3D conceptual drawing of the studied detector geometry. (b) Schematic drawing of the scintillator's and the light-guide's dimensions and their edge treatments.

4.2. Methods

4.2.1. Gamma detector design

The gamma detector comprises a 250×150×9.5 mm^3 NaI(Tl) scintillator (Scionix B.V.) attached to a 325×195×13.3 mm^3 glass light-guide (Figure 4.1b), and is read out by 15 Hama-

matsu R6236 PMTs, each having a 54×54 mm^2 square sensitive area [162]. The entrance surface of the scintillator is painted with a reflective coating while the edges are absorptive (Figure 4.1b and Figure 4.2d). The scintillator and light-guide are sealed in an aluminium case (the matt face in Figure 4.2a) with a distance of about 12 mm from the upper edge of the scintillator to the upper edge of the aluminium case (see Figure 4.2b), which is the minimum distance the manufacturer can safely achieve to preserve the hygroscopic NaI(Tl) crystal from humidity. The PMTs are attached to the light-guide in a staggered arrangement (Figure 4.1a) and extend partly over the scintillator's left, right, and lower edges [140]. At the upper critical edge, three PMTs are directly attached to the light-guide and two other PMTs are attached via two 150 mm-long additional light-guides with 60×31 mm^2 cross-section. The additional light-guides are fused quartz bricks, polished on all six surfaces, and wrapped with white PTFE tapes. This special light-guide-PMT geometry aims to imitate partly-overextending PMTs at the critical edge (where there is no physical space for truly overextending PMTs), like at the other three edges. All of the PMTs and additional light-guides are fixed in the detector box with aluminium frames and pushed tightly against the readout window of the light-guide (Figure 4.2c). Optical grease (Scionix BC90/147) is applied at the interfaces to ensure good optical coupling. A light-tight box, which is painted black inside to reduce the influence of possible light leaks to PMTs, is used to hold the detector. The high voltage applied to the PMTs is 800 V.

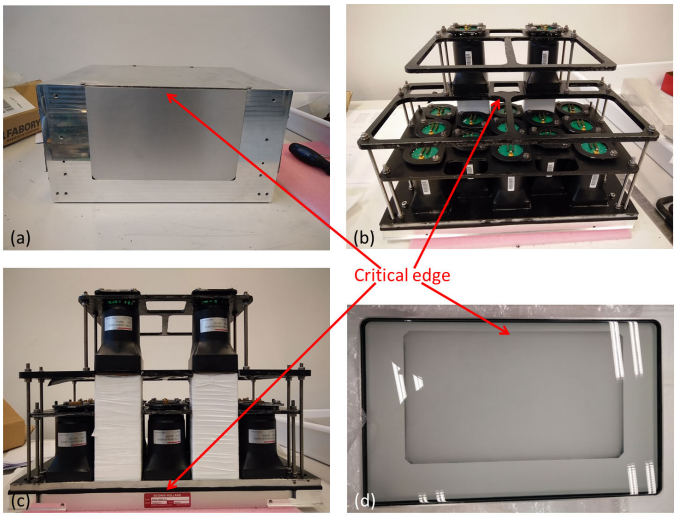

Figure 4.2: Pictures of the gamma detector in various degrees of disassembly to illustrate the components inside. The position of the critical edge in each picture is marked by the red arrows. (a) The front face of the detector showing scintillator and detector box. Note that this side is facing down in (b)–(d). (b) A bottom view of the detector showing the placement of the PMTs. (c) A top view of the detector showing the additional light-guides (white blocks) and the two PMTs that are not directly placed on the light-guide attached to the scintillator, but coupled to it via the additional light-guides in a stacked structure. (d) The scintillator underneath the light-guide.

4.2.2. Read-out scheme

Figure 4.3 illustrates the read-out scheme. The signal from each PMT is continuously sampled through a pulse shaping circuit, which includes low pass filters and pole-zero correction by one of the ADC channels on a NI-5752 ADC board (sampling frequency 50 MHz) mounted on a NI PXIe-7961 FPGA. The FPGA is programmed in LabVIEW and stores the 15 PMTs' ADC values in cyclic buffers with 1k depth (20 µs). The ADC sample stream from each channel is high-pass filtered to create a trigger signal, and if any of the 15 trigger signals is above a preset threshold (logic OR operation), an event will be triggered. After a trigger, the 15 PMTs' cyclic buffers are read, and the sum of 90 samples following the trigger signal is considered to represent the PMT pulse integral, while 15 samples preceding the trigger signal are used as a baseline reference. The sum of the 90 samples subtracted by the baseline offset determined by the 15 samples is calculated. During the event processing, new triggers are not accepted. An event data structure contains the 15 integrals of PMT pulses corrected for their own individual baselines, a timestamp, an event number, and a trigger map (indicating which PMT triggered the event). The events built on FPGA are transferred to a PC through a DMA transceiver. On the PC, a LabVIEW program controls the data acquisition process.

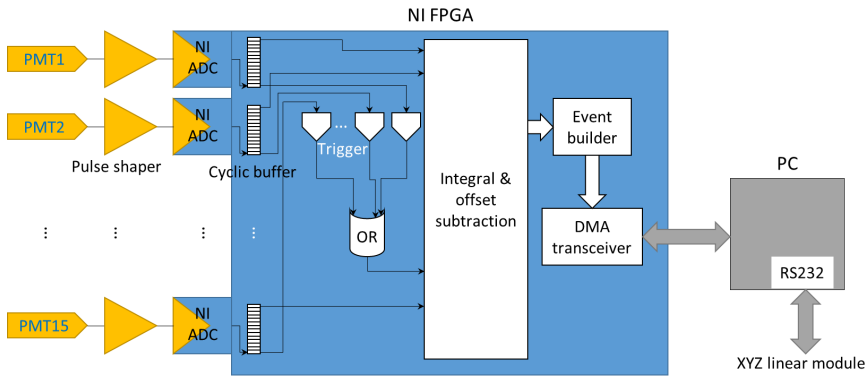

Figure 4.3: The PMT signal acquisition and XYZ linear module controlled by the PC.

4.2.3. Position and energy estimation

The interaction position and energy for each event are both estimated with Anger logic (centroid of gravity) and ML: the result of the former is the start location of the search in the latter. To improve Anger estimation, a threshold is applied to each PMT output followed by a linearity correction [169].

The ML algorithm is implemented based on a Gaussian model instead of a Poisson model, as the absolute number of optical photons collected by PMTs is hard to measure [145, 160]. If the Gaussian mean and standard deviation of the output of PMT m ($\mu_m(x, y, E)$ and $\sigma_m(x, y, E)$, referred to as reference PMT outputs) are known for gamma photons at all

possible interaction location and energy combinations (x, y, E), one can calculate the likelihood that an interaction resulted in the measured PMT outputs. The interaction location and energy combination $(\hat{x}, \hat{y}, \hat{E})$ estimated by the ML algorithm is the one that maximises this likelihood. Details of ML estimation can be found in [140, 145, 160, 185].

The detector was calibrated only with a 140 keV beam source (see 4.2.4) and the reference PMT outputs for other energies were obtained by scaling the 140 keV outputs (both μ_m and σ_m). The values of σ_m are scaled taking into account the detector intrinsic energy resolution of ~5% [164, 165].

A combined estimation of the interaction location and energy $(\hat{x}, \hat{y}, \hat{E})$, i.e. a full search in 3D space, is computationally expensive. However, for single-isotope imaging the interaction energy is only used to reject scattered events. As this can also be done by likelihood thresholding [160, 175], we also implemented an ML estimation of only the interaction position (x, y) and then applied the likelihood threshold to reject scatter.

The energy estimation in our Anger logic implementation is done by comparing the light collection of the test event with the reference mean light collection at the Anger estimated position, normalised by 140 keV (using the same reference PMT outputs from ML calibration). As a check, we also estimated the interaction energy with the same Anger approach in case we used likelihood thresholding for scatter rejection.

4.2.4. Calibration

Before assembling the 15 PMTs into the gamma camera, their relative gains were first calibrated by measuring their photopeak positions in the gamma ray detection spectra. This relative gain is used in Anger logic position estimation, which serves as a starting point of ML estimation. To this end, a small piece of NaI crystal was mounted on top of each of the PMTs, and two gamma sources, ^{57}Co and ^{241}Am, were placed near the setup. Subsequently, the relative gain of each PMT was measured for at least 48 hours, and the average value after it settled to a stable value was taken. Two additional gain measurements were done to determine the attenuation of the scintillation light within the two pieces of additional light-guides. After inserting each of the two additional light-guides between the small NaI crystal and a PMT, we compared the measured photopeak position to the measurement without the light-guide and in this way we obtained the attenuation of light in the 150 mm long quartz glass. This attenuation was later accounted for in the PMT gains for the two PMTs behind the two additional light-guides. The PMT gains were used in gain corrections in all subsequent measurements.

After the gain calibration, all PMTs and additional light-guides were mounted onto the gamma detector. Subsequently a trigger calibration and a position calibration were applied. To this end, a beam collimator was used as is conventional in gamma detector calibration with monolithic scintillators [145–147, 160, 175, 186, 187]. A disk with 50 MBq

^{99m}Tc inside was put in a lead-made beam collimator with a Ø1.1×25 mm^3 hole to obtain a perpendicular gamma photon beam on the detector. We obtained about 1000 counts per second within the photopeak with this activity. The beam collimator was fixed on an XYZ linear module with 0.03 mm positioning accuracy that could scan over the whole scintillator area.

The trigger thresholds of the PMTs were set according to the criterion that only the interactions close to a PMT could possibly trigger this PMT. Details of the criterion are illustrated with the example in Figure 4.4. With the chosen thresholds, the trigger rate from the same beam should be more or less constant irrespective of placement with respect to the PMTs.

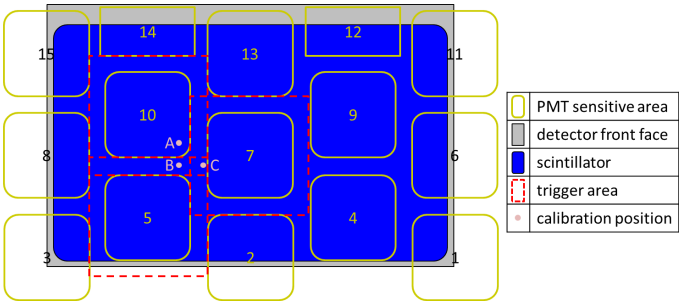

Figure 4.4: Example of the criterion of setting trigger thresholds: interactions at position A (above the sensitive area of PMT 10), should trigger PMT 10 but should not trigger other PMTs; interactions at position B (above the gap between PMT 10 and 7), should either trigger PMT 10 or 7 but should not trigger other PMTs; interactions at position C (above the interstitial of PMT 10, 7, and 5), should trigger PMT 10, 7, or 5, but should not trigger other PMTs. Based on these criteria, the trigger area for every PMT can be drawn (dotted red line).

After proper PMT trigger thresholds were set, the scintillator was scanned by the collimated 140 keV photon beams in a 5 mm pitch grid (4 s per position), while recording the PMT outputs at each of these positions. The first and last rows/columns of the scanned positions were 1 mm from the nearest scintillator edges. This measurement was done to get the reference PMT outputs used in ML estimation and Anger linearity correction (see 4.2.3).

Subsequently, scattered photons were removed from the calibration measurement with the following procedure consisting of three steps:

- **Step 1**: filter out the events that were triggered by the PMT(s) whose trigger area (see Figure 4.4) did not include the known calibration position.
- **Step 2**: filter out the events that are outside the photopeak in the spectrum of the (sum of) *triggered* PMT output(s) (outside the photopeak is defined as being outside twice its full-width-at-half-maximum (FWHM)).
- **Step 3**: filter out the events that are outside the photopeak in the spectrum of the sum of *all* PMT outputs. Figure 4.5 illustrates the effects of these three steps on

the events measured at position B in Figure 4.4.

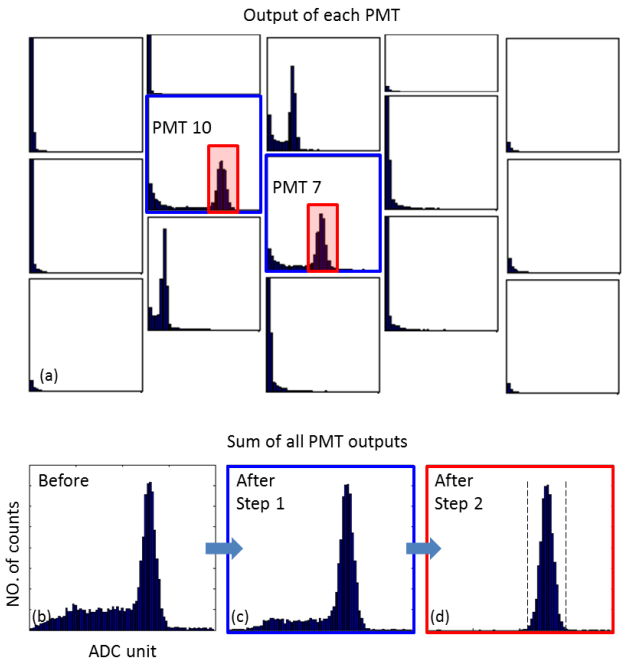

Figure 4.5: Example of the effect of the three cleaning steps on the spectrum of the sum of all PMT outputs. (a) Output spectra resulting from a calibration beam at position B in Figure 4.4 (same layout as the PMT layout). (b)–(d) shows the sum of spectra of all PMTs at each step: (b) is before the cleaning procedure; (c) is after selecting the events triggered by PMT 10 and 7; (d) is after filtering out the events outside the photopeak of the sum spectrum of PMT 10 and 7. A photopeak window is applied to (d) subsequently as Step 3 to further remove residual scattered events.

After the three-step 'cleaning' procedure, the μ_m and σ_m of each PMT signal over all 'clean' events were calculated for a given beam position, and this 5 mm-interval calibration dataset of PMTs' was then bi-cubically interpolated into a 1 mm grid to be used in ML estimation. The 'clean' calibration data is also used to calculate the mean light collection map and light collection resolution map of the detector. Light collection is determined by summing the mean output of all PMTs, while light collection resolution is calculated by taking the FWHM of the photopeak of the spectrum of the sum of all PMT outputs and dividing it by its mean. We use the term light collection to differentiate the direct sum signal (in ADC units) from the estimated energy (in keV units). Similarly, light collection resolution is obtained from the light collection spectrum, while energy resolution is obtained from the spectrum of estimated energies.

The likelihood threshold map described in 4.2.3 is also generated from the calibration data. From earlier Monte Carlo simulations and literature [140, 160], we chose the threshold to be 15% meaning that the threshold would reject the 15% least likely events in the

'clean' dataset. Later, we also tested other thresholds for comparison. An example likelihood spectrum with the chosen threshold is shown in Figure 4.6.

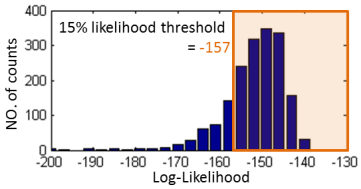

Figure 4.6: The likelihood spectrum of the 'clean' events at position B in Figure 4.4. The 15% likelihood threshold at this position occurs for a log-likelihood of -157.

4.2.5. Test data measurement

Several test datasets were acquired to characterise the detector's intrinsic spatial resolution, its spatial linearity, its energy resolution, and its uniformity. It is important to note that the 'cleaning' procedure in 4.2.4 was not applied to test data as *a priori* knowledge when evaluating the camera performance as with the test data we want to mimic the realistic situation in which the origin of the gamma photon is unknown.

The first measurement was a line spread function (LSF) measurement. According to NEMA standard [168], the intrinsic spatial resolution and linearity are to be evaluated as the profiles of LSFs, measured by masking the detector with a lead plate with vertical/horizontal slots of 1 mm-width and a gamma source put far away in front of the detector. We used our beam collimator and the XYZ linear module to imitate such a measurement by sweeping the source in vertical and horizontal lines along the detector face with a speed of 7.5 mm/s back-and-forth. The count density of the lines on the detector was about 1500 counts/mm. The LSFs were put at a 10 mm interval at the centre of the detector and at a 6 mm interval near the edges. We took multiple 1 mm-wide profiles perpendicular to every LSF and fit a Gaussian function to every profile (default `Trust-Region` fit implemented in MATLAB™). From this fit, we calculated the FWHM resolution and differential linearity (averaged standard deviation of the fitted profile centres of each line). The first and last lines were 3 mm from the nearest scintillator edges. The sweeping method should give equivalent result as the NEMA method, but is easier to apply (we are not in the possession of slit masks) and more flexible (different slit intervals can be tested).

The second test dataset came from a point spread function (PSF) measurement which was acquired in the same way as the calibration dataset, except that a 10 mm pitch grid in the centre of the detector and a 6 mm pitch near the edges was used. The first and last rows/columns of the PSF tested positions were also 3 mm from the nearest scintillator edge. This dataset was used to characterise the energy resolution of the detector that can be obtained by different estimation algorithms. The PSFs are easy to 'clean' com-

pared with LSFs, as was described in the 'cleaning' procedure in 4.2.4, and for this reason they were also used to analyse in-depth the estimated PSFs from different algorithms, the scatter rejection capability with different methods, and the influence of different thresholds in likelihood threshold ML.

The third measurement done was a uniformity measurement which was performed, according to NEMA [168], by putting an uncollimated source of 13 MBq ^{99m}Tc in front of the detector two meters away and measuring for 50 minutes. Then the counts were resampled in 5×5 mm^2 superpixels and filtered by a 9-point kernel $[[1,2,1],[2,4,2],[1,2,1]]$. The integral and differential uniformity were subsequently calculated over the whole detector using the definition:

$$\text{uniformity} = \frac{\max - \min}{\max + \min} \times 100\%, \tag{4.1}$$

where max and min are the maximum and minimum superpixel values on the whole detector for integral uniformity, and the local maxima and minima over 5 consecutive superpixels for differential uniformity. A separate uniform irradiation measurement (7 MBq ^{99m}Tc for 100 minutes, 2 m from detector) was done to obtain the correction map for calculating a corrected uniformity (uncorrected flood image pixel-wise divided by the correction map).

4.3. Results

4.3.1. Maps from calibration data

From the calibration data, we obtained the light collection, light collection resolution and 15% likelihood threshold maps over the detector surface (see Figure 4.7). As explained in 4.2.4, these three maps are subsequently used in energy estimation and scatter rejection. As the scintillator has black edges, it can be expected that the light collection is not uniform over the whole surface. This was indeed the case; compared to the central part of the detector, the edges had about 60% light collection while the corners collect about 40% as much light. The horizontal asymmetry of Figure 4.7a may be caused by the reflector above the scintillator at the top-left corner not being properly attached to the scintillator. Consequently, the FWHM light collection resolution map was comparable to that of a conventional large area white edge Anger camera in the centre (~9%), yet poorer at the edges and corners (~15%). Here the light collection resolution is equivalent to the optimal energy resolution of the detector as it is from a 'clean' dataset and free from possible inaccuracy from position/energy estimation methods.

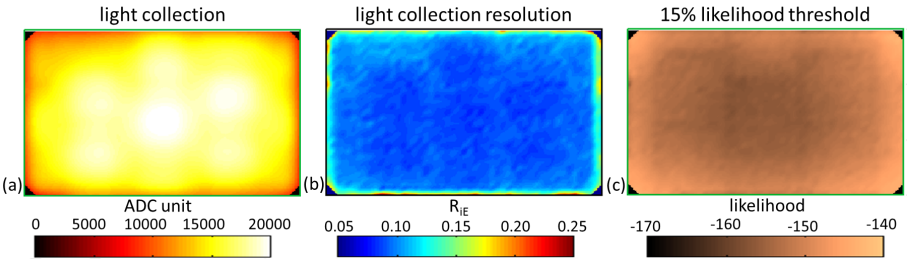

Figure 4.7: From the calibration data, we acquired (a) the light collection map (b) the light collection resolution map, which is equivalent to the optimal energy resolution, and (c) the likelihood threshold map (here we show the 15% likelihood threshold).

4.3.2. Position estimation

For the measured vertical and horizontal LSFs, we used two methods to estimate the interaction position and to reject scatter events. The first method was to use ML to co-estimate both interaction position and energy (called energy ML). In this case the energy window was set to a width of twice the FWHM of the light collection resolution (Figure 4.7b). The LSFs estimated with this method are shown in Figure 4.8a, from which interpolated spatial resolution maps (Figure 4.8b) are calculated. The second method used was the application of a likelihood threshold to remove scatter events (called 15% likelihood ML). The likelihood threshold is location-dependent and was shown in Figure 4.7c. The LSFs estimated with this method are provided in Figure 4.8c, from which the spatial resolution maps of Figure 4.8d are calculated. Note that the LSFs near the edges in Figure 4.8a and 4.8c were differently spaced (6 mm intervals) than in the centre (10 mm intervals). It is clear that likelihood thresholding gives better results than energy ML near the edges in terms of average differential linearity ($\bar{\ell}_{\text{diff.}}$) and average spatial resolution ($\bar{R}_i$). For the last 30 mm from the scintillator critical edge, the energy ML method gave an average spatial resolution of 3.58 mm and 5.32 mm in horizontal and vertical directions respectively, while the likelihood thresholding method gave 3.60 mm and 4.33 mm resolution.

4.3.3. Scatter rejection

Intrinsic spatial resolution characterises the FWHM of the line profiles but does not tell how well scattered events are removed (which would add background counts to the detector). Additionally, it is important to check that the algorithms do not throw away true (i.e. non-scattered) events as this would negatively impact the detector's sensitivity. Therefore, to better characterise these properties for the energy ML and 15% likelihood ML methods, we here checked these issues using the PSF measurement and compared results with that of conventional Anger logic, as this is the standard method and should still work well in the centre of our detector. For this comparison, the energy window in Anger estimation was set to the same values as the energy window used in energy ML. In

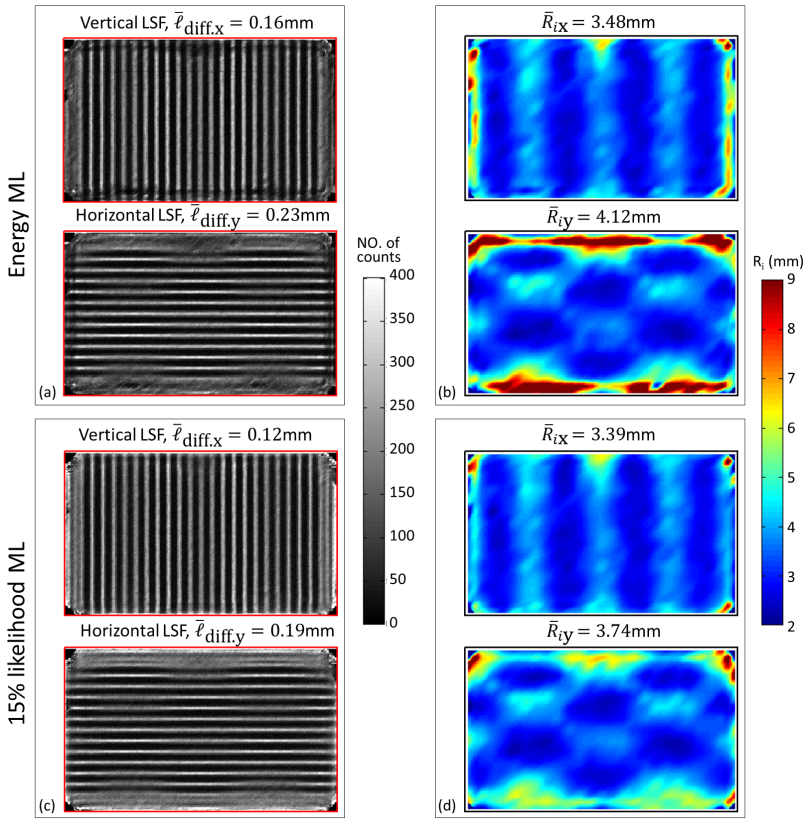

Figure 4.8: LSF test dataset as measured by the gamma detector using different algorithms for position estimation. (a) Detector images obtained with an (x, y, E) 3D ML search, with (b) resulting interpolated spatial resolution maps. (c) Detector images obtained with likelihood thresholding (threshold set at 15% least likely calibration data) with (d) resulting calculated and interpolated spatial resolution maps. The averaged differential linearity $\bar{\ell}_{\text{diff.}}$ and intrinsic spatial resolution $\bar{R}_i$ are also provided. Note that the LSFs near the edges in (a) and (c) were differently spaced (6 mm intervals) than in the centre (10 mm intervals).The rectangular frame in all the images marks the edge of the scintillator.

Figure 4.9a—c, all estimated test PSFs are shown for energy ML, 15% likelihood ML and Anger logic. The PSF within the yellow box (which is 25 mm from the critical edge of the scintillator) was subsequently projected onto the horizontal axis and shown in Figure 4.9d—f in semi-log scale for the same algorithms. These plots show that background counts were present although these were not visible on the scale of Figure 4.9a—c and did not contribute to the FWHM spatial resolution. However, such background counts may play a role when reconstructing images from the projections and an algorithm which is better able to reject them is generally preferable. In this experiment, these background counts most likely originated from background radiation and scatter in the beam collimator plus its holder.

As is already clear from visual inspection of Figure 4.9d—f, 15% likelihood ML (Figure 4.9e)

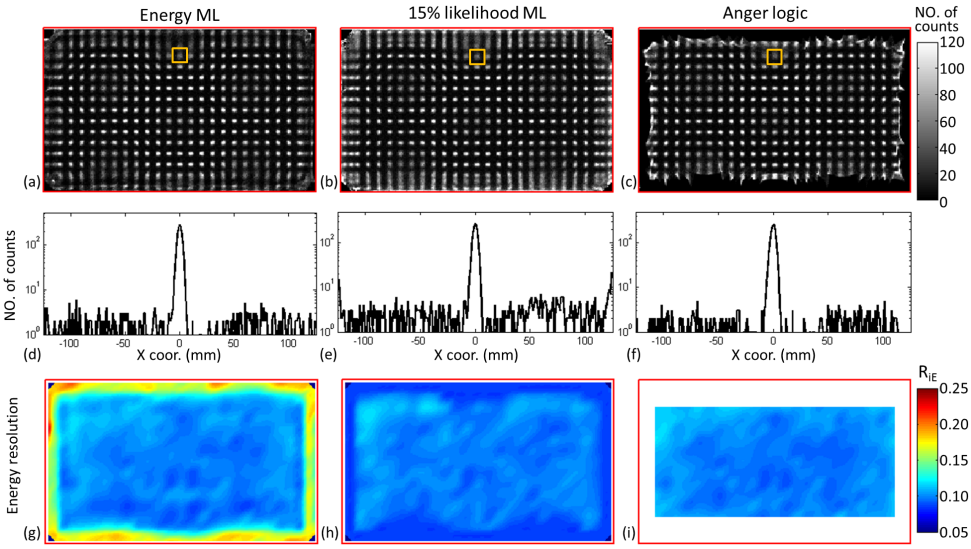

Figure 4.9: (a) The test PSFs estimated with the energy ML method. (b) The test PSFs estimated with 15% likelihood ML. (c) The test PSFs estimated with Anger estimation; the central linear region is up to about 25 mm to the edges. (d)–(f) show projections of the marked PSF in the yellow boxes in (a)–(c) in semi-log scale. (g)–(i) show the spatial distribution of the energy resolution from (a)–(c). In (i) only the energy resolution in the central part of the detector is calculated as the position estimation is completely distorted at the edges.

resulted in more counts in the background than the other two methods. A quantitative comparison of the three methods' average central PSF and background count ratios is shown in Table 4.1. Here the central PSF and background count ratios are defined as the number of counts inside or outside Ø10 mm of the irradiation position, divided by all incoming photons. As a reference, we also show these numbers for the same dataset but with scatter removed by the 'cleaning' procedure of 4.2.4 and with position estimated with the ML algorithm without any event rejection (called 'clean' data ML).

In the *centre* of the detector where Anger logic was able to obtain linear position estimation (at least 15 mm away from the left and right edges, 25 mm from the upper and lower edges), Anger logic, energy ML, and 15% likelihood ML lead to similar central PSF count ratios as the 'clean' dataset, thus all methods have similar behaviour for non-scattered events. However, the background count ratios were different: the 'cleaning' procedure left only 1.1% background, while Anger logic and energy ML left 7.7% and 9.3% respectively, and the 15% likelihood ML had a 16% background count ratio, which was the highest among the three methods.

Over the *whole* detector, 15% likelihood threshold still leads to similar central PSF count ratios as the 'clean' dataset (34% vs. 35% respectively), while the difference in background count ratios between these two methods was still large (2.4% vs. 18%); energy ML had a reduced central PSF count ratio over the whole detector (30%) because the position estimation near the edges was quite poor. We also varied the likelihood threshold to see

Table 4.1: The average central PSF and background count ratio of test positions in the centre of the detector or over the whole detector for different algorithms

method and region		central PSF count ratio	background count ratio
centre of detector			
'clean' data ML		0.36	0.011
Anger		0.36	0.077
energy ML		0.36	0.093
ML likelihood threshold	15%	0.34	0.16
whole detector			
'clean' data ML		0.35	0.024
Anger		N/A	N/A
energy ML		0.30	0.11
ML likelihood threshold	12%	0.34	0.19
	15%	0.34	0.18
	18%	0.33	0.18
	21%	0.32	0.16
	25%	0.31	0.15
	30%	0.30	0.15
	37%	0.28	0.13
	45%	0.25	0.11

if that is a proper way to reject more background counts. However, from Table 4.1 it can be seen that using a higher threshold leads to rejection of more background only at the expense of rejecting as many valid events (events near irradiated position). To evaluate how the estimated energy from energy ML correlates to the calculated likelihood from 15% likelihood ML, we made a scatter plot for the events' likelihoods and energies which is shown in the appendix Figure 4.11.

4.3.4. Energy resolution

Figure 4.9g—i showed the estimated energy resolution obtained with the three methods. At the central region, all three methods gave similar energy resolution of about 10%, which, understandably, is poorer than the light collection resolution in Figure 4.7b, as this is the best achievable energy resolution obtained from calibration data from which scatter was removed. The linear region of Anger logic is limited to the central part of the detector, so for Anger logic only the energy resolution in the central part is shown. An unreasonable feature in Figure 4.9h is that the edges have even better energy resolution than the central part. We checked the estimated energy spectra near the edges and the 15% likelihood ML method tends to estimate a test event at the position where the reference light collection is similar to the test event's light collection. We therefore cannot

use the energy estimation results near the edges from the 15% likelihood ML to facilitate scatter rejection.

4.3.5. Uniformity

As was shown in 4.3.3 and 4.3.4, energy ML did not give an equally accurate position estimation near the critical edge as 15% likelihood ML and it was also slow, therefore 15% likelihood ML is the preferred method for our MP-MBT application. For this reason, we only applied the 15% likelihood threshold algorithm to the uniformity measurement data. Figure 4.10a shows the flood image obtained in this way. Piled-up counts can be observed at the edges and distortions occur at the corners. The source of the pile-ups are discussed in the Discussion section. With the approach described in 4.2.5, in the central region, defined as the detector area more than 5 mm away from any edge, we calculated the integral uniformity of the detector to be 12% and the maximum differential uniformities to be 8% and 7% in horizontal and vertical direction respectively without any uniformity correction. After uniformity correction (shown in Figure 4.10b), in the same region the integral uniformity was 1.7% while the maximum differential uniformities were 1.2% and 1.3% in horizontal and vertical directions.

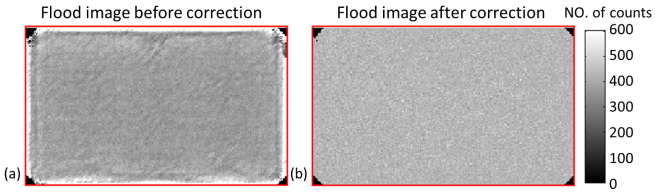

Figure 4.10: Flood image measured with a 13 MBq ^{99m}Tc source placed about 2 m in front of the detector for 50 minutes without any uniformity correction (a), and after uniformity correction (b). Pixel size shown is 1 mm^2. The rectangular frame marks the edge of the scintillator.

4.4. Discussion

From the measurement results shown in Figure 4.8, it can be inferred that the proposed detector using ML position estimation with likelihood thresholding gives an intrinsic spatial resolution comparable to that of conventional Anger cameras in the centre (about 3.5 mm resolution). Near the critical edge, the vertical resolution is somewhat degraded (4.3 mm on average in the last 30 mm from edge), but this region is completely useless in conventional Anger cameras. Energy ML gives much poorer spatial resolution near the scintillator's edges and is slower than the 15% likelihood threshold method. Therefore energy ML seems not to be the most suitable algorithm for this detector. The test positions are up to 3 mm to the scintillator edges while the calibration positions are up to 1 mm to the scintillator edges. Considering the good spatial linearity and uniformity near the critical edge with 15% likelihood ML, it is fair to say that the dead edges are less than

3 mm from the scintillator edge. Including the 12 mm sealing required to preserve the enclosing hygroscopic NaI(Tl) crystal, the overall dead edge of the detector is thus less than 15 mm. This is much better than the 4 cm dead edge for conventional gamma cameras, and should be sufficient to realise the proposed and simulated MP-MBT for which we already performed simulations with 15 mm dead edge gamma camera and found results very similar to those in [32, 33]. If, in the future, the sealing material over the critical edge could be reduced while the NaI(Tl) is still well protected, the scintillator could be positioned closer to the critical edge and the overall critical edge could be even reduced.

Ideally, to evaluate the effect of the two additional light guides one would like to experimentally compare different gamma camera geometries. Unfortunately, this is not possible due to practical constraints (rearranging the PMTs in the current detector may lead to damage). However, in an earlier study we have simulated a gamma detector of similar dimension as the assembled one but with different PMT arrangements [140], including the current one and an arrangement without additional light-guides. The experimental detector compares well to the simulation results in terms of spatial resolution. Especially the similarity in how resolution varies over the detector area is striking; the best resolution is obtained in the interstitials between PMTs, a poorer resolution is achieved above the centres of PMTs, and the poorest resolution is above the centre of the edge PMTs. Based on these similarities with simulations, we believe that for a detector without additional light guides the last 30 mm critical edge would have spatial resolution similar to that above PMT 13 (see Figure 4.4) in the assembled detector which is among the poorest areas of the detector. This would seriously hamper our MP-MBT scanner's performance.

Additionally, we would like to point out that a design with additional light guides along the full critical edge was also simulated Figure 4.4. While such a design is beneficial for resolution near the critical edge, the downside is a much poorer spatial resolution along the opposite edge. Therefore, we chose to build the current staggered design. The simulation results were presented in Chapter 3.

From Table 4.1 the 15% likelihood threshold seems to be a proper choice as the number of accepted counts in the PSF is comparable to that of Anger logic, indicating that valid events are accepted. The background found in the test data (as shown in Figure 4.9e) is hard to get rid of by adjusting the likelihood threshold, as is evident from the numbers in Table 4.1. This background also exists for energy ML and Anger position estimation (Figure 4.9d and 4.9f), but its magnitude is about 40% smaller for these methods than for 15% likelihood ML. Similarly, we checked that in the LSF measurements, the background counts (counts within 5 mm from the scanned lines) also have about 40% smaller magnitude for energy ML than for 15% likelihood ML (in the centre of the detector). This means that energy windowing is still better at scatter rejection than likelihood thresholding, and this could be a reason to use energy windowing in the central region of the detector and use likelihood thresholding only near the edges. Whether this background will be a big issue or not has to be checked in a real scanner where scattered photons from the torso

are present and need to be rejected.

The flood image in Figure 4.10a contains quite obvious pile-up counts at the edges. These pile-ups are partly due to the ML algorithm, which tends to give a certain amount of pile-ups at the end of its search grid. In Figure 4.8e and 4.8g, and Figure 4.9b, there are indeed some observable pile-ups in the last pixels near the edges of the scintillator, though the effect is very small. The main source of the pile-ups is probably the presence of the aluminium case of the scintillator. As was mentioned in 4.2.1, the scintillator is placed in an aluminium case with a thickness of 12 mm at the critical edge and 4 mm to other edges. The critical edge requires more sealing space as the light-guide does not extend over the scintillator's edge very much, while at the other three edges, the light-guide edges extend about 30 mm over the scintillator's edge. As the cross section for scatter of 140 keV gamma photons in aluminium is large, extra scatter events will take place near the critical edge. It should be kept in mind that when using the camera, the aluminium sides of the detector should be shielded.

In SPECT imaging, scatter rejection with simply one photopeak window is not always sufficient. A triple energy window scatter correction is often applied [54, 135]. With the ML likelihood thresholding method, the counts in the side energy windows are mostly rejected and thus we can no longer implement a triple energy window correction. One may think of using three reference PMT output sets plus three likelihood threshold sets for three energy windows (photopeak and two side energies) respectively in order to obtain projection images of the three energy windows, and then apply a triple energy window scatter correction. The reference PMT outputs for the 140 keV photopeak are directly calculated from the calibration measurement, and to get the reference PMT outputs in the two side energy windows, we may scale the calibration measurement to the side window energies, and then follow the process in 4.2.4. This idea will be tested in the future with phantom scans.

The current detector is designed and built to be applied in a MP-MBT system in which there is one critical edge. However, the proposed additional light-guide design can in principle be extended to all edges of the detector if required, so that it can meet the requirements of dedicated cardiac SPECT scanners, or any other applications in which minimising dead edges is important.

4.5. Conclusion

In conclusion, we have presented and experimentally evaluated a black-edge gamma detector with staggered PMT arrangement in combination with ML position estimation. We found that the detector has the ability to also estimate events near the scintillator's edges; the detector dead edge including the 12 mm sealing case is less than 15 mm. The detector therefore is a good and cost-effective solution when conventional cameras with

roughly 4 cm dead edges are not acceptable.

Acknowledgement

The authors would like to thank Malte Verleg and Ernst van der Wal from DEMO TU Delft for their help of making the detector box into reality.

Appendix

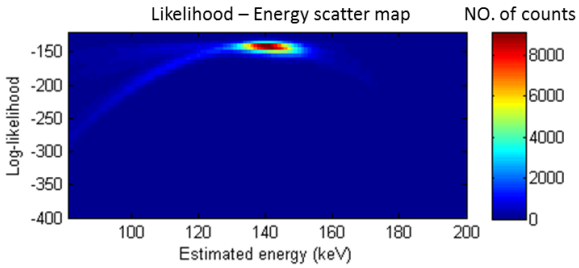

Figure 4.11: A scatter plot of the log-likelihood from likelihood ML and estimated energy from energy ML for all events in the PSF test data measurement. Only the centre of the detector is considered (as this is the region where both algorithms estimate positions properly) and rejected events are included. It is clear that a large log-likelihood strongly correlates with a 140 keV photopeak energy. For other energies, most events have a clearly decreased likelihood, but for lower energies there also exist events with a rather high likelihood. These events most probably are the cause that windowing estimated energy is more effective in scatter rejection than likelihood thresholding (see Table 4.1).

5

Characterisation of a multi-pinhole molecular breast tomosynthesis scanner

This chapter is adapted from:
Beien Wang, Jarno van Roosmalen, Rob Kreuger, Jan Huizenga, Freek J. Beekman, Marlies C. Goorden. *Characterisation of a multi-pinhole molecular breast tomosynthesis scanner*, Physics in Medicine and Biology **submitted** (2020).

In recent years, breast imaging using radiolabelled molecules has attracted significant interest. Our group has proposed a multi-pinhole molecular breast tomosynthesis (MP-MBT) scanner to obtain 3D functional molecular breast images at high resolutions. After conducting extensive optimisation studies using simulations, we here present a first prototype of MP-MBT and evaluate its performance using physical phantoms. The MP-MBT design is based on two opposing gamma cameras that can image a lightly compressed pendant breast. Each gamma camera consists of a 250×150 mm^2 detector equipped with a collimator with multiple pinholes focusing on a line. The NaI(Tl) gamma detector is a customised design with 3.5 mm intrinsic spatial resolution and high spatial linearity near the edges due to a novel light-guide geometry and the use of square PMTs. A volume-of-interest is scanned by translating the collimator and gamma detector together in a sequence that optimises count yield from the scan region. Derenzo-like resolution phantom images showed that the system can reach 3.5 mm resolution for a clinically realistic ^{99m}Tc activity concentration in an 11-minute scan, while in breast phantoms the smallest spheres visible were 6 mm in diameter for the same scan time. To conclude, the experimental results of the novel MP-MBT scanner showed that the setup had sub-centimetre breast tumour detection capability which might facilitate 3D molecular breast cancer imaging in the future.

5.1. Introduction

Breast cancer is the most commonly diagnosed cancer in women. About 25% of cancer diagnoses and 15% of cancer deaths in females are due to breast cancer [1]. X-ray mammography (sometimes assisted by ultrasound or magnetic resonance imaging) is the most widely-used imaging modality in breast cancer diagnosis [2]. Although X-ray mammography has generally high diagnostic sensitivity (over 80%) and reasonably low dose (less than 1 mSv), it suffers from a reduced sensitivity for patients with dense breasts, which is especially disadvantageous as denser breasts are associated with a higher risk of getting breast cancer [10, 11]. Recently, dedicated molecular breast imaging using radiolabelled tracers has been applied in a clinical setting and has been proven to provide diagnostic information complementary to that of conventional X-ray mammography, especially for patients with dense breasts [30, 31]. Several planar breast scintigraphy devices [57–60], dedicated breast SPECT [63, 71, 177] and PET [65, 66, 68, 69] scanners are under development or available on the market. As many tracers assessing physiological processes such as blood flow, glucose consumption, aberrant cellular proliferation, gene/protein expression associated with cancer, lipid metabolism, and tumour hypoxia are available or under development [23], molecular imaging may not only have diagnostic applications but also play a role in developing individualised treatment plans or in monitoring therapy.

Recently, our group proposed a novel multi-pinhole molecular breast tomosynthesis (MP-MBT) scanner dedicated to image the 3D distribution of single gamma-emitting tracers in the breast, with the aim to detect sub-centimetre breast tumours [32, 46]. In the MP-MBT design in Figure 5.1, the patient lies prone on a bed containing a hole for the

breast which is slightly compressed by two transparent compression plates. Two webcams placed behind the compression plates view the breast and their images serve as input to a graphical user interface on which the user can select a scan region [188]. The breast is then scanned by translating two gamma cameras equipped with focusing multi-pinhole collimators over a sequence of camera positions. Due to the focusing pinhole geometry and the possibility to confine the scan region, the scanner has the option to focus on a small suspect region to increase count yield from that region.

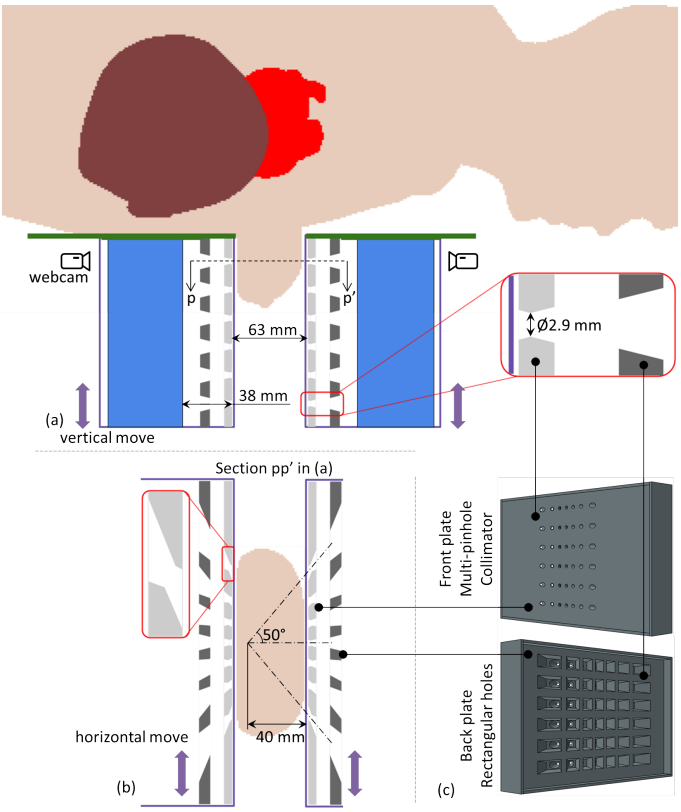

Figure 5.1: MP-MBT design. (a) A sagittal view of the scanner with the six rows of pinholes and geometry of the system shown. (b) Coronal view through section pp′ in (a) with the focusing geometry of the pinholes shown. (c) The multi-pinhole collimator 3D design showing multi-pinhole collimator and shielding plate.

Based on previously conducted optimisation studies [32, 33, 140], we have built a prototype scanner to experimentally characterise the concept of MP-MBT. To evaluate the performance of the prototype scanner, we performed phantom experiments with customised resolution and breast phantoms. In this paper, we describe the newly built MP-MBT setup and present the phantom scan results.

5.2. Methods

The built prototype setup contains a dedicated gamma detector with a multi-pinhole collimator mounted in front, an XYZ linear module (GaoGong ChuanDong Co., Ltd.) to translate the gamma camera (0.03 mm precision according to manufacturer's specifications), and a table in front of the gamma camera with a hole in it to imitate the patient bed (Figure 5.2). In the designed geometry, two gamma cameras view the breast from opposite directions. As we currently have only one gamma camera available we emulate the two-camera imaging procedure by scanning the phantom from one side, rotating it by 180°, and scanning it again from the other side. The equivalent camera-camera distance in the scans is 63 mm (see also Figure 5.1a).

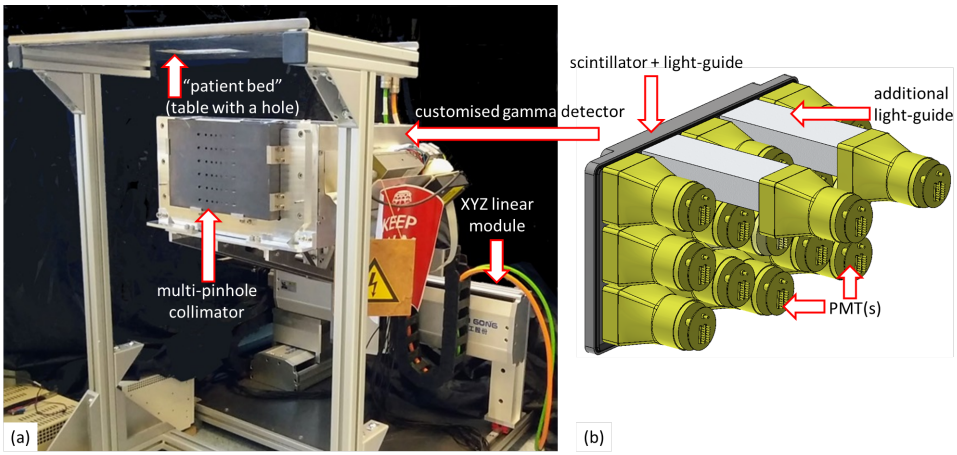

Figure 5.2: (a) MP-MBT proof-of-concept setup. The customised gamma camera is equipped with a multi-pinhole collimator and placed underneath the table representing the patient bed. It can be translated with a linear XYZ module. (b) A schematic representation of the customised gamma detector showing the encapsulated scintillator and light-guide, as well as two additional light-guides wrapped in reflecting material, and the 15 PMTs [174].

5.2.1. Collimator and gamma detector details

The lead multi-pinhole collimator (Figure 5.1c) contains a 6 mm-thick collimator plate with 42 pinholes, as well as a second 10 mm-thick shielding plate with rectangular holes between the collimator and the detector to prevent overlapping of pinhole projections on the detector. The two plates are attached by four surrounding 3 mm-thick rectangular plates made of lead. The pinholes in the collimator are grouped in 6 rows of 7 pinholes each. The 7 pinholes in each row all focus on a point 40 mm away from the collimator face, with a maximum angle between pinhole axis and direction perpendicular to the collimator of 50° (Figure 5.1b). The distance between neighbouring rows of pinholes is 24 mm. Each pinhole has a 2.9 mm diameter and opening angle of 40°. As in this design, the breast is viewed by the pinholes over an angular range less than 180°, the technique is

denoted by tomosynthesis instead of tomography. The design criteria for this collimator can be found in [33]. The front face of the collimator is placed 38 mm in front of the entrance face of the gamma detector.

A regular Anger detector was not suitable for this setup because of the large unusable edges (> 4 cm) that are commonly present in these type of detectors [140]. We, therefore, employ a customised design, comprising a 250×150×9.5 mm^3 NaI(Tl) scintillator (Scionix B.V.) attached to a 13.3 mm-thick glass light-guide and read out by 15 Hamamatsu R6236 square PMTs with a 56×56 mm^2 effective area placed in a staggered layout (see Figure 5.2b). The staggered PMT layout is enabled by a novel light-guide design [174]: two PMTs at the upper edge of the detector collect the light from the scintillator through two additional light-guides; such a design allows to realise the staggered layout without having to extend these two PMTs outside the scintillator's upper edge where the patient bed is located and thus no space is available. With this novel detector design, facilitated by maximum likelihood interaction position estimation [160], we are able to obtain high spatial linearity near the detector edges in a cost-effective way as we used rather large PMTs and a continuous scintillator. The unusable upper edge of gamma detector is about 15 mm including the 12 mm thick sealing case for the scintillator. The average full-width half-maximum (FWHM) spatial resolution for the gamma detector is 3.4 mm and 3.7 mm in horizontal and vertical directions, respectively. The detailed description and the performance of this customised gamma detector was reported in Chapter 4.

5.2.2. Point source calibration and system matrix generation

To calibrate the scanner, we measured 522 point source responses over the field of view by moving the gamma camera in front of a 10 MBq ^{99m}Tc point source of about Ø1 mm (Figure 5.3a), which is very similar to the point source calibration procedure described in [189]. In total, the calibration measurement took about one hour. This measurement was used to obtain the position/orientation deviations of the assembled gamma camera with respect to the designed geometry similar as was done in [190]. In this method, it is assumed that the actual collimator-detector geometry is well described by a rotation/translation with respect to the design. Thus, from the calibration, 12 parameters have to be estimated (3 angles describing the rotation, 3 distances describing the translation, both for the collimator and the detector). The system matrix for image reconstruction was subsequently generated using voxelized raytracing (VRT) software developed in our group [54] with the designed geometry and the geometrical information from the point source calibration as inputs. VRT takes attenuation (in the collimator and the detector) into account but ignores photon scatter. The collimator in VRT was modelled with 1/8 mm voxels of different materials (lead or vacuum) and the detector was modelled by a continuous piece of 9.5 mm-thick NaI. The scintillation process and electronic noise of the gamma detector are also not modelled in VRT. Instead, the combined effect is included in the detector intrinsic energy resolution modelling. The gamma detector in-

trinsic spatial resolution was set to 3.5 mm FWHM by blurring the VRT-generated point source responses with a 3.5 mm FWHM Gaussian kernel, which was the average value over the whole detector surface obtained by measurements [174]. As we had only one gamma camera, we measured the system matrix for this gamma camera and rotate it 180° to generate the system matrix for the virtually opposite gamma camera.

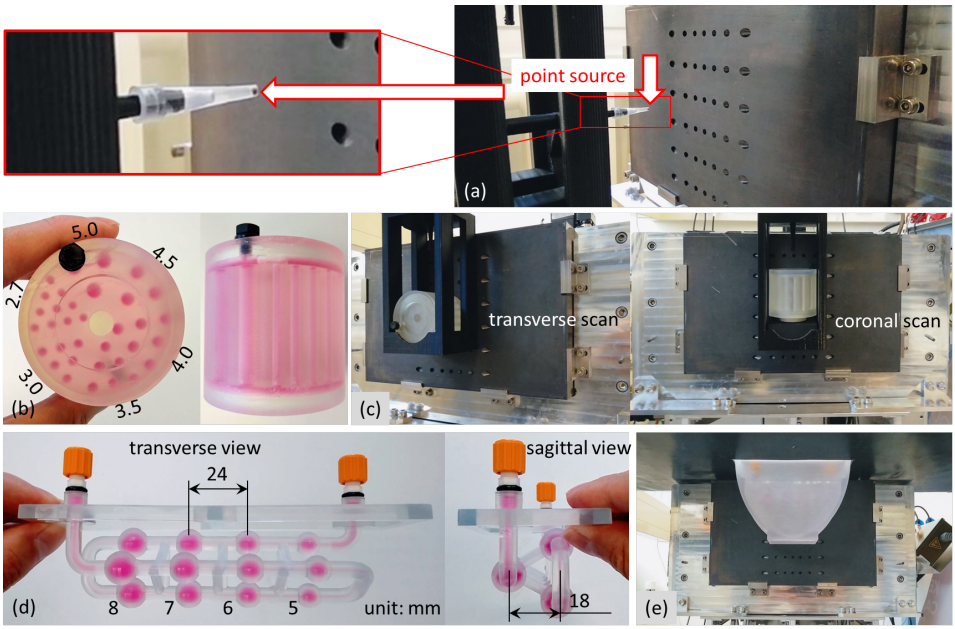

Figure 5.3: Setup for calibration and phantom measurements. (a) Setup for point source measurement including an enlarged view of the source. (b) The Derenzo-like resolution phantom with rod diameters indicated (rods were filled with red ink for better visualisation). (c) Resolution phantom measurement setup for horizontal and vertical directions in order to analyse the spatial resolution in transverse and coronal planes. (d) Tumour phantom with the diameters of the spheres and distances between neighbouring spheres indicated (spheres were filled with red ink for better visualisation). (e) Breast phantom measurement setup with the tumour phantom inside.

5.2.3. Phantom scans

To assess the spatial resolution of the scanner, a Derenzo-like resolution phantom (Figure 5.3b), 3D printed in our institute (with Formlabs Clear resin), was scanned. The phantom is a 50 mm × Ø52 mm cylinder, with 35 mm long cylindrical rods inside. At each end of the rods, a chamber of 3 mm × Ø47 mm facilitates filling of the phantom. Scans of the phantom with the rods filled with two activity concentration levels (37 kBq/mL and 370 kBq/mL ^{99m}Tc) were obtained to evaluate the system resolution. The phantom was placed in the (virtual) centre in between the two gamma cameras during scanning. To check the spatial resolution in transverse and coronal directions, two scans were performed at each activity concentration with the phantom in two different orientations

(Figure 5.3c).

Secondly, a breast phantom containing spheres of different sizes, representing different tumours, was scanned. The breast chamber (DSM Somos® Watershed XC 11122 resin; QingLiu 3D Tech. Co., Ltd.) was 3D printed and has the shape of a semi-elliptic cylinder with 110 mm semi-major axis, 75 mm semi-minor axis, and 55 mm thickness, representing the dimensions of a mildly compressed average breast (Figure 5.3e) [133, 177]. The tumour phantom (3D Systems Accura® 60 resin; Phantech LLC.) was also 3D printed and contains three sets of Ø8 mm, Ø7 mm, Ø6 mm, and Ø5 mm spheres connected by Ø1 mm channels (Figure 5.3d). The neighbouring spheres in each set have a 24 mm separation, and all spheres are at a distance of 22.5 mm and 40.5 mm from the two collimator plates. The ^{99m}Tc activity concentration injected into the tumour phantom was 37 kBq/mL while the breast phantom was filled with a background activity concentration of 3.7 kBq/mL. These levels represent a realistic activity concentration in a clinical setting when 925 MBq of ^{99m}Tc-Sestamibi is injected [113, 133, 191]. A measurement with a 15 times higher activity concentration was also done as a reference.

Two scanning modes were applied in the phantom experiments; a whole-breast mode and a focusing mode. The whole-breast mode uses a sequence of gamma camera positions that is suitable to scan the entire breast; in this case, the gamma camera moves over a 156 mm distance in the horizontal direction and 22.5 mm in the vertical direction (90 scan positions). In the focusing mode, the scan sequence is adapted such that only part of the breast is imaged. In this case, the gamma camera moves 18 mm horizontally around the Ø5 mm spheres and also 22.5 mm vertically (55 scan positions). A description of the specific scanned position in the whole-breast mode and focusing mode can be found in the appendix. In this study, the whole-breast mode sequence was used in both resolution phantom and breast phantom scan, while the focusing mode sequence was used only in the breast phantom scan with the three Ø5 mm spheres at the focus. In both modes, the total scan time was 11 minutes (emulated by two 11 min. scans at each side). For the breast phantom, we additionally added projections from two 11 min. measurements to obtain one emulated 22 min. scan. In total, eight 11 min. whole-breast mode and focusing mode scans of the breast phantom were performed, and with this dataset four 22 min. whole-breast and focusing scans were also obtained.

5.2.4. Analysis of reconstructed images

All phantom images were reconstructed with a Maximum Likelihood Estimation Maximisation (MLEM) algorithm [192]. No attenuation correction or scatter correction was applied. Besides visual inspection of the reconstructed images, we used the tumour-to-background Contrast-to-Noise Ratio (CNR) to evaluate the image quality. The CNR is

defined by:

$$\mathrm{CNR} = \frac{\bar{S} - \bar{B}}{\sigma}, \tag{5.1}$$

where $\bar{S}$ is the average signal in the tumour, $\bar{B}$ denotes the average signal in the background, while σ is the standard deviation of the signal in the background region. The regions-of-interest selected to determine tumour and background signals are shown in Figure 5.5a.

The tumour phantom includes four sets of 3 spheres of the same size (Figure 5.3d). Therefore, the data of 24 spheres were available to determine the mean and standard deviations of the CNR for every tumour size in the 11 min. scans, while the data of 12 spheres were used in the 22 min. scans.

5.3. Results

5.3.1. Resolution phantom

Figure 5.4 shows resolution phantom images for different slices, slice thicknesses and phantom orientations at several iteration numbers. All images on the same row with the same slice thickness are displayed with the same colour scale. From these images, it can be inferred that in the transverse plane, the spatial resolution is location-dependent: in the centre exactly in-between the two gamma cameras (Figure 5.4b), the spatial resolution is poorer than in the regions close to one of the gamma cameras (5.4a and 5.4c). Such a phenomenon is also observed in the coronal slices in 5.4e and 5.4f, in which the upper and lower regions in each image appear clearer than the central part. There is no significant variation along the transaxial direction of the phantom in the coronal scan, therefore, only one slice in the centre of the phantom is shown in the coronal plane (5.4e).

From Figure 5.4a—c, the smallest rods that can be distinguished in the 4.5 mm transverse slices are about Ø3.0 to Ø3.5 mm (depending on location) when a realistic 37 kBq/mL activity concentration is used. When summing all slices (33 mm) together (Figure 5.4d), Ø3.0 mm rods are clearly visible and even Ø2.7 mm rods can partly be seen. In the reference high-count phantom (filled with 370 kBq/mL activity), Ø2.7 mm rods are visible in the 4.5 mm transverse slices near the two ends of the phantom and in the 33 mm thick slices, but in the central part of the phantom, the smallest rods that can be distinguished are Ø3.5 mm. In the coronal plane, the smallest distinguishable rods are Ø3.5 mm regardless of the amount of activity and the slice thickness.

5.3.2. Breast phantom

Slices through the breast phantom images are displayed in Figure 5.5. In the 11 min. whole-breast scan of a breast containing a realistic activity concentration (Figure 5.5b),

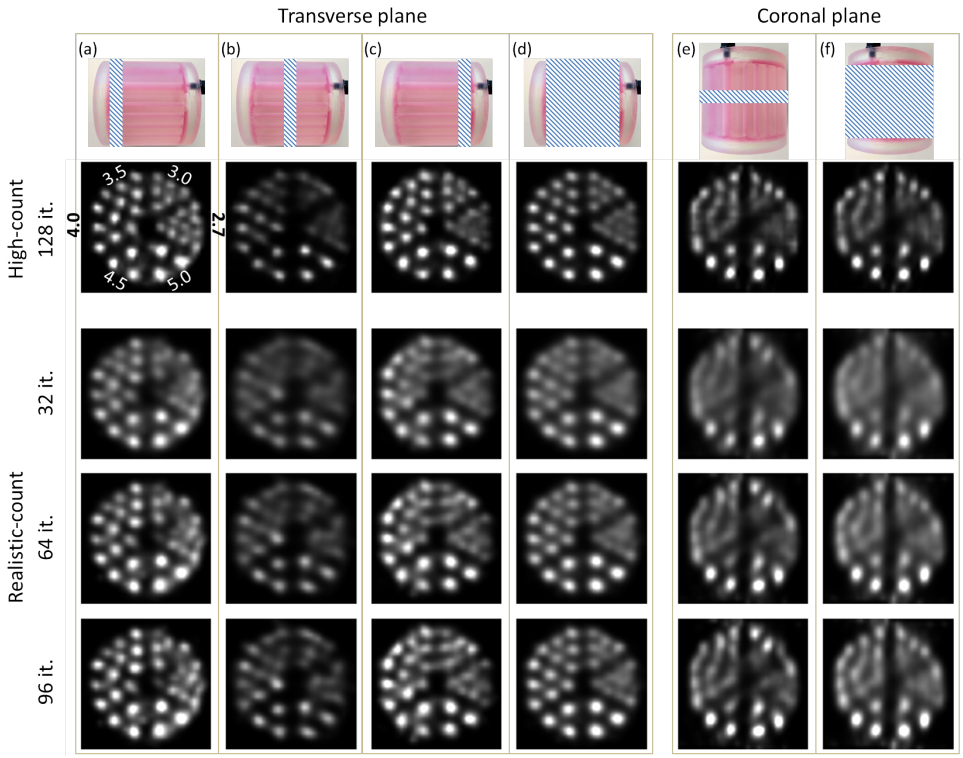

Figure 5.4: Resolution phantom images obtained at different iterations. The top row shows the location, orientation and thickness of the displayed slices. The second row shows the images obtained with a high activity concentration of 370 kBq/mL activity (as a reference) while the other rows display images with a realistic 37 kBq/mL activity concentration obtained at different MLEM iterations filtered with a 2.0 mm FWHM Gaussian kernel for better visualisation. Columns (a)—(c) show transverse slices of 4.5 mm thick taken at the two ends and in the middle of the phantom when it was placed horizontally between the two (virtual) gamma cameras. Column (d) displays a transverse slice of 33 mm thickness. Columns (e) and (f) display coronal slices with 4.5 mm and 33 mm slice thickness obtained from the phantom placed vertically.

the Ø8 mm and Ø7 mm spheres are all clearly visible, while two out of three of the Ø6 mm spheres are visible. The Ø5 mm spheres cannot be distinguished from the background at all. It also appears from the images that the background contains noise with spatial correlations, meaning that structures that could be mistaken as lesions are visible. Though buried in background noise in the whole-breast mode scan, the Ø5 mm spheres can be better distinguished when scanning in the focusing mode (Figure 5.5c), both in the transverse and the sagittal slices. For the 22 min. scan (5.5d and 5.5e), the background noise is reduced, which makes the Ø6 mm spheres better visible in the whole-breast mode, while in the focusing mode, the Ø5 mm spheres are clearer than in the 11 min. scan. Moreover, in the sagittal view, all spheres are elongated, which indicates that the spatial resolution of the system is different in different directions as is also clear from the resolution phantom scans. It is worth noting that the upper edges of the reconstructed volumes close

to the chest wall are removed from displaying as they have artefacts due to the 15 mm unusable edge of the detector [174].

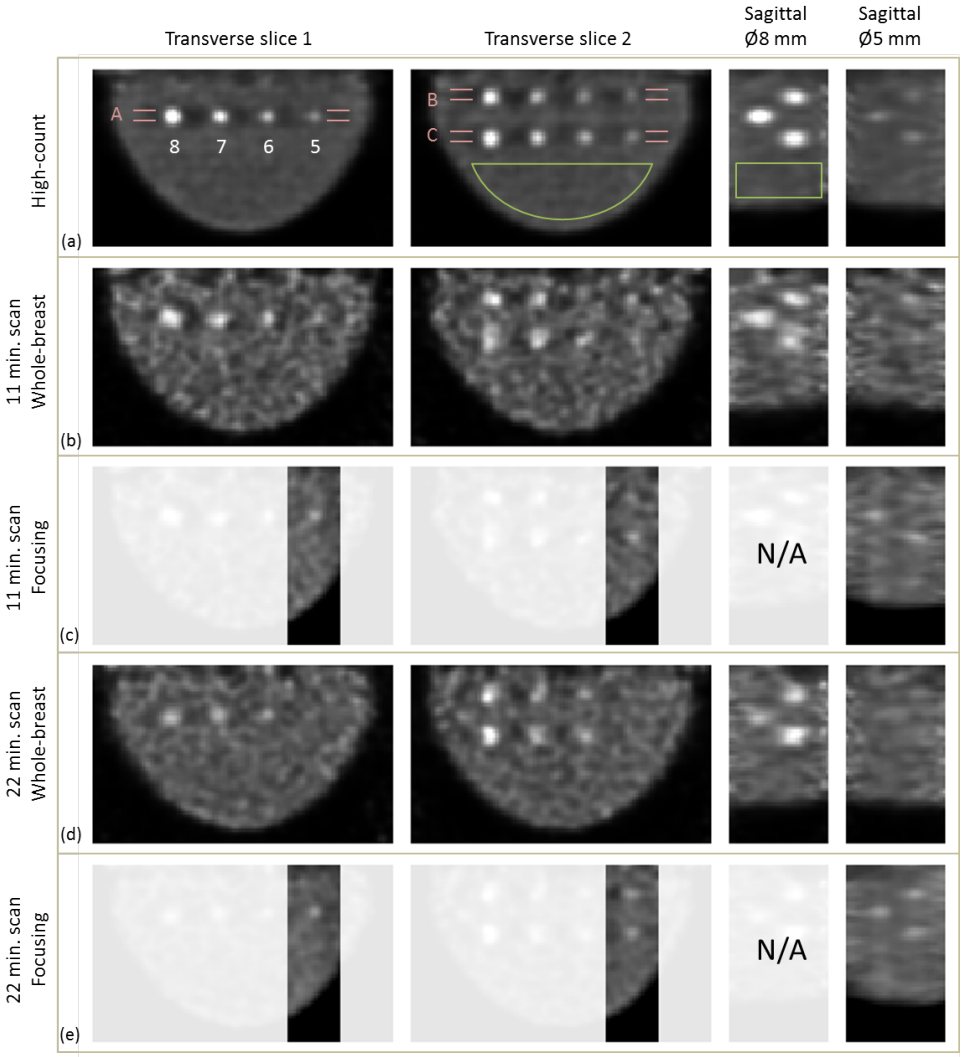

Figure 5.5: The reconstructed slices of the breast phantom with the tumour phantom inside. (a) High-count (550 kBq/mL injected in the tumour phantom and 55 kBq/mL injected in the breast phantom) scan of the breast phantom as a reference image of the phantom. (b) 11 min. whole-breast scan of the breast phantom and tumour phantom with realistic activity concentration (37 kBq/mL in tumour phantom and 3.7 kBq/mL in the background). (c) 11 min. scan focusing at the Ø5 mm spheres with realistic activity concentration. Only the part of reconstructed slices in the focus is shown (therefore the sagittal slice through the Ø8 mm spheres is dubbed N/A, i.e. Not Available). (d) and (e) 22 min. scans in whole-breast and focusing modes. All images have 4.5 mm slice thickness and are taken from 16-iteration MLEM reconstructions, and a 2.0 mm FWHM Gaussian filter is applied for better visualisation.

To better visualise the results in Figure 5.5, profiles (4.5 mm width; indicated by the red

lines in Figure 5.5a) through the three rows of tumours are plotted in Figure 5.6 for different scan modes and activity levels. The spheres invisible in Figure 5.5 show small 'bumps' in Figure 5.6, but can be hardly distinguished from the background.

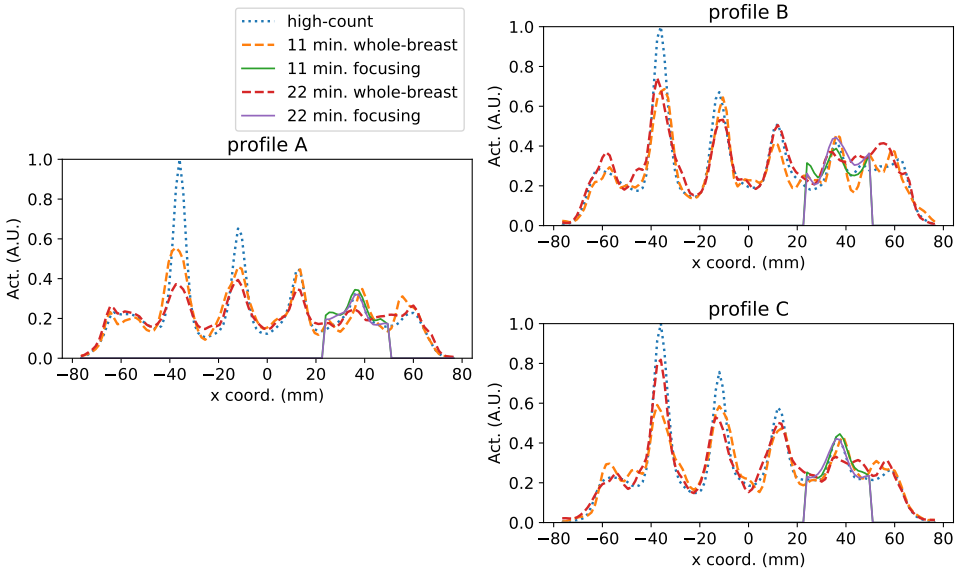

Figure 5.6: Profiles through tumour phantom from reconstructed slices (as indicated in Figure 5.5a). Reconstructed activity in the high-count measurement is divided by 15 (ratio between high-count and realistic activity concentrations), and at each profile, the reconstructed activity is normalised to the high-count measurement's maximum respectively.

Table 5.1 shows the average CNRs and their standard deviations. In our MP-MBT images, a CNR > 4 usually indicates that the sphere can be easily distinguished from the background, while CNR < 3 indicate that it is impossible to distinguish them, which is comparable to the Rose criterion [193]. The quantitative results in Table 5.1 confirm the visual impression in Figure 5.5 and Figure 5.6.

Table 5.1: Average CNRs of the tumour phantom spheres of different sizes (and scan modes)

Ø (mm) sphere	**CNR of 11 min. scan**	**CNR of 22 min. scan**
8	6.0±1.4	7.9±1.4
7	4.3±1.1	5.6±0.8
6	3.4±1.2	4.5±0.6
5	1.7±1.0	2.4±0.9
5 (focusing)	3.2±0.9	3.8±0.5

5.4. Discussion

In the resolution phantom images (Figure 5.4), slices near one of the two (virtual) gamma cameras appear clearer than those at the centre in between the cameras. This phenomenon exists regardless of the amount of activity inside the phantom. We believe that this is due to the geometry of the MP-MBT system in which pinhole magnification factors differ significantly depending on the location in the scanner. From [33], we estimate that system resolution in the slice in between cameras (shown in Figure 5.4b) would be 6.6 mm, while for the slices close to one of the cameras (5.4a and 5.4c) better system resolutions of 4.8 mm were calculated. Therefore, it is understandable that the measurement reveals poorer spatial resolution in-between the two gamma cameras than near one of them. Reconstructed slices near the centre of the phantom are also lower in intensity than those near the collimator, which is clearly visible in the images in Figure 5.4. We investigated this issue by doing a full simulation of the resolution phantom scan (with/without attenuation, with/without detector blur, with/without noise) in our VRT software. From the simulations, we found that for noiseless projections, the middle part attains a similar intensity as the peripheral parts only after hundreds of MLEM iterations, i.e. the central part of the image converges slower than the peripheral parts. However, if we reconstruct the experimental images with more iterations, the noise in the reconstructed images increases which degrades visual image quality even if a post-filter is applied. Attenuation of the gamma rays in the breast phantom plays only a minor role here.

In the images shown in Figure 5.5b and d, the presence of spatially correlated noise is the main reason that the Ø5 mm spheres are not well visible. The pattern of the noise is very similar in appearance to small lesions, which may cause false-positive diagnoses. Such a noise pattern was also visible in our earlier simulation study for different collimators [194]. However, in the high-count measurement (Figure 5.5a), the noise pattern is largely reduced. Moreover, such a noise pattern is not commonly visible in low-sensitivity clinical or preclinical SPECT images (complete sampling over 180°), which may suggest that the observed noise pattern results from the interplay between limited count statistics and sampling incompleteness. The cause of the pattern is still under investigation.

To overcome the correlated noise issue and increase the specificity of MBT for smaller tumours, the use of a longer acquisition time might be a solution, as has been shown by the improvement of images in Figure 5.5d and 5.5e. Although only mild breast compression is applied, for longer measurements, the comfort of patients may be impaired and risks of motion artefacts can increase. Therefore, it could be impractical to increase acquisition time. Another solution may be using a different reconstruction algorithm. Instead of MLEM without any prior information, a maximum *a posteriori* reconstruction [195] for general purpose SPECT or PET and total variation reconstruction [196] for X-ray breast tomosynthesis are reported to lead to improved noise characteristics. Therefore, further investigation of different reconstruction algorithms for MP-MBT could be a subject

of further research.

The whole-breast mode of MP-MBT could be performed to search for any lesions in the breast at the diagnostic stage, while the focusing mode could be performed after a tumour is detected with another modality, to confirm if a tumour was successfully treated, or to characterise a tumour with known location, e.g. using different tracers. In this aspect the method has advantages over PET since SPECT has the unique ability to perform multi-isotope imaging. From Figure 5.5, Figure 5.6 and Table 5.1, it is clear that the focusing mode of MP-MBT clearly outperforms the whole-breast mode. Such modes could be highly interesting in combination with new tracers for tumour responses or to identify tumour types [197–201]. Compared with planar breast scintigraphy devices, MP-MBT gives extra information on the 3rd dimension which is useful in determining the location, size and shape of the tumour. Investigations still need to be done to check the tumour detectability of MP-MBT (both whole-breast and focusing modes) compared with planar breast scintigraphy to determine if the former is a good alternative for the latter.

5.5. Conclusion

To conclude, our group has built a setup to test the concept of MP-MBT. A Derenzo-like resolution phantom showed that the system's spatial resolution was about 3.5 mm, while a breast phantom scan showed the smallest detectable tumours to be Ø6 mm in the whole-breast mode and Ø5 mm in the focusing mode for a clinically realistic activity concentration. Thus, sub-centimetre tumour detection is possible with the MP-MBT system, though challenges related to reducing the correlated background noise remain. MP-MBT might be a supplementary tool to the standard X-ray mammography or X-ray breast tomosynthesis in diagnosing breast cancers because of its many unique imaging capabilities e.g. characterising tissue.

Acknowledgement

We thank Benjamin Cox and Justin Jeffery from Phantech LLC. for designing and printing the tumour phantom. We thank Malte Verleg and Kevin Kamman from DEMO at TU Delft for designing and printing the resolution phantom, and the former also for all the help in the mechanical aspect of MP-MBT. We thank Kathalijne de Nijs, Daan van der Ham and Jason Mulder for their work on the optimisation of several aspects of MP-MBT.

Appendix

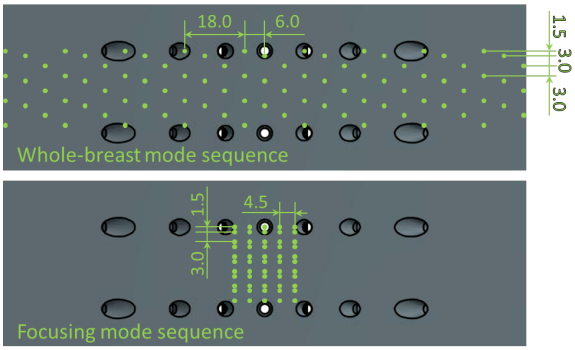

Figure 5.7: The sequences of the two scan modes used in MP-MBT with respect to the multi-pinhole collimator. For the whole-breast mode, the neighbouring scanned positions have 18 mm interval, while there is a 6 mm horizontal shift between each neighbouring row; the vertical neighbouring rows have 1.5 mm or 3.0 mm interval. For the focusing mode, the horizontal interval is fixed at 4.5 mm, while the vertical interval is either 1.5 mm or 3.0 mm.

6

Conclusion

Multi-pinhole SPECT technology is currently widely applied in e.g. small animal imaging and clinical cardiac imaging with proven success. This thesis aims to bring the multi-pinhole collimation technique to breast cancer imaging, to improve 3D localisation and detection of tumours in dense breasts which is a difficulty with the routine X-ray mammography technology. To this end, a multi-pinhole molecular breast tomosynthesis (MP-MBT) scanner was developed and validated.

This thesis builds on earlier simulation studies in our group for scanner geometry optimisation. The in-house simulation tools were validated at the start of this thesis. From the simulations, we found out that conventional gamma detectors are not suitable for MP-MBT, and a customised gamma detector design was required. Therefore, several novel gamma detector setups were designed and evaluated in a simulation study and the optimal setup was experimentally realised and characterised. As the performance of the customised gamma detector met the initial requirements, we mounted a multi-pinhole collimator onto the detector and integrated the whole gamma camera with a robot arm enabling it to scan objects with a programmed sequence. Finally, phantom experiments were carried out to evaluate the prototype MP-MBT and we can indeed image sub-centimetre tumours in 3D.

In Chapter 2, the voxelized raytracing (VRT) software, which was developed earlier in our group and used throughout the project, was described and validated for MBT. To this end, the simulation results from VRT were compared with Monte Carlo simulations which showed a difference in the (almost) noiseless projection images as low as 0.15% on average. However, VRT was at least 300 times faster than an accelerated Monte Carlo simulation in generating low-noise projections, which is useful in evaluating different

system designs. Moreover, in Chapter 2, we performed full Monte Carlo simulations of the whole MP-MBT system, including scattered photons and tracer activity in the torso (in heart and liver), which were not considered in VRT. The Monte Carlo simulation showed that scatters and torso activities would not be detrimental to MP-MBT images, however we should keep in mind that activities in torso, heart and especially liver may contaminate the detector when scanning very large breasts and a larger volume (include parts of the torso) should be modelled in reconstruction.

The simulation results of earlier simulation studies, as well as Chapter 2, relied on a gamma detector with a small dead edge on the side close to the patient's chest. There are such detectors on the market but these are very expensive. Therefore, we decided to build our own detector. In Chapter 3, we simulated several gamma detector designs based on a continuous NaI(Tl) scintillator and photomultiplier tube (PMT) readout, a combination which has been proven to be cost-effective in the past half century. This mature detector technology together with a special light-guide we introduced, the use of a maximum likelihood position estimation algorithm and black edge coating of the scintillator ensured that we got sufficiently small dead edges. This special design could benefit any application in which small dead edges are required.

From different layouts simulated in Chapter 3, we selected the best performing one and built a prototype detector, as described in Chapter 4. This in-house-developed detector was characterised experimentally and the results were very similar to those of the simulations in Chapter 3. Therefore, the simulations in Chapter 3 were implicitly validated and may serve as a reference for future research in designing scintillation detectors. Chapter 4 also showed that although our detector had small dead edge, its energy resolution (thus capability to reject scatter based on the estimated energy of photons) at the edges was poor. Fortunately, high energy resolution is not required for MP-MBT as Chapter 2 has shown that photon scattering is not detrimental to our application. Nevertheless, for future studies on black-edge scintillators, the poor scatter rejection should be taken into consideration. The dead edge of the built detector was about 15 mm, which was much better than the 4 cm dead edge present in conventional gamma detectors, but it could still be improved further. As 12 mm of these 15 mm dead edge was due to the scintillator case to ensure a good sealing of the hygroscopic NaI(Tl) crystal, the dead edge can be even smaller if the sealing space can be reduced in the future.

As reported in Chapter 5, we built a prototype system by integrating the customised gamma detector with an optimised multi-pinhole collimator and a robot arm which enabled the detector to scan with a programmed sequence. Two typical sequences, a whole-breast scan (the entire volume of a breast is scanned) and a focusing scan (a long scan of a small part of the breast volume), were tested. A resolution phantom and a breast phantom filled with both a high and a clinically realistic activity of ^{99m}Tc were scanned. The resolution phantom scan revealed the spatial resolution of MP-MBT was non-uniform, i.e. the closer to one of the collimators, the higher spatial resolution we could obtain. The

breast phantom scan showed that the smallest tumour visible in an 11-minute whole-breast scan with a realistic activity was about Ø6 mm. In a focusing scan, which is a unique feature of MP-MBT, small tumours of Ø5 mm could be very well distinguished from the background. Moreover, when increasing the scan time from 11 minutes to 22 minutes, the image quality was further improved. The detection of even smaller tumours with MP-MBT was hard mainly due to the fact that the noise in the reconstructed images was spatially-correlated, i.e. the noise and smaller tumours in the reconstructed images had similar blob-like shapes and were hard to distinguish from each other. The scanning results from the high-activity breast phantom showed much less noise correlation which suggested that the noise pattern was most likely due to a interplay of low numbers of counts and limited angular information in the setup.

The current MP-MBT prototype is a proof-of-concept setup and still far from a device that can be used in the clinic. The results from Chapter 5 indicate that the MP-MBT technology would probably not replace the current breast cancer diagnosis routine, but rather be a supplementary tool to it. In principle, its unique focusing mode can be an effective method for post-operation examination, e.g. MP-MBT can focus on the location where there used to be a tumour to determine if it was successfully removed after treatment. As the major limitation of MP-MBT is its suboptimal resolution-sensitivity trade-off and object sampling, future research about nuclear medicine in breast cancer imaging should focus on advanced methods to deal with these shortcomings, e.g. advanced reconstruction methods utilising *a priori* information or deep learning methods.

References

[1] Ferlay, J., Soerjomataram, I., Dikshit, R., *et al.*, *Cancer incidence and mortality worldwide: Sources, methods and major patterns in GLOBOCAN 2012*, Int J Cancer **136**, E359 (2015).

[2] Calonge, N., Petitti, D. B., DeWitt, T. G., *et al.*, *Screening for breast cancer: U.S. preventive services task force recommendation statement*, Ann Intern Med **152**, 199 (2010).

[3] Egan, R. L., *Experience with mammography in a tumor institution — evaluation of 1,000 studies*, Radiology **75**, 894 (1960).

[4] Hendrick, R. E. and Helvie, M. A., *Mammography screening: A new estimate of number needed to screen to prevent one breast cancer death*, Am J Roentgenol **198**, 723 (2012).

[5] Chen, B. and Ning, R., *Cone-beam volume CT breast imaging: Feasibility study*, Med Phys **29**, 755 (2002).

[6] O'Connell, A. M., Karellas, A., and Vedantham, S., *The potential role of dedicated 3D breast CT as a diagnostic tool: Review and early clinical examples*, Breast J **20**, 592 (2014).

[7] Skaane, P., Bandos, A. I., Gullien, R., *et al.*, *Comparison of digital mammography alone and digital mammography plus tomosynthesis in a population-based screening program*, Radiology **267**, 47 (2013).

[8] Ciatto, S., Houssami, N., Bernardi, D., *et al.*, *Integration of 3D digital mammography with tomosynthesis for population breast-cancer screening (storm): a prospective comparison study*, Lancet Oncol **14**, 583 (2013).

[9] Rafferty, E. A., Park, J. M., Philpotts, L. E., *et al.*, *Assessing radiologist performance using combined digital mammography and breast tomosynthesis compared with digital mammography alone: Results of a multicenter, multireader trial*, Radiology **266**, 104 (2013).

[10] Berg, W. A., *Tailored supplemental screening for breast cancer: what now and what next?* Am J Roentgenol **192**, 390 (2009).

[11] Hruska, C. B., *Molecular breast imaging for screening in dense breasts: state of the art and future directions*, Am J Roentgenol **208**, 275 (2017).

[12] de Groot, J. E., Broeders, M. J. M., Branderhorst, W., den Heeten, G. J., and Grimbergen, C. A., *A novel approach to mammographic breast compression: Improved standardization and reduced discomfort by controlling pressure instead of force*, Med Phys **40**, 081901 (2013).

[13] Holland, K., Sechopoulos, I., den Heeten, G., Mann, R. M., and Karssemeijer, N., *Performance of breast cancer screening depends on mammographic compression*, in *Breast Imaging, IWDM 2016*, Vol. 9699 (2016) pp. 183–189.

[14] Jeukens, C. R. L. P. N., van Dijk, T., Berben, C., Wildberger, J. E., and Lobbes, M. B. I., *Evaluation of pressure-controlled mammography compression paddles with respect to force-controlled compression paddles in clinical practice*, Eur Radiol **29**, 2545 (2019).

[15] Berg, W. A., Zhang, Z., Lehrer, D., *et al.*, *Detection of breast cancer with addition of annual*

screening ultrasound or a single screening MRI to mammography in women with elevated breast cancer risk, JAMA **307**, 1394 (2012).

[16] Plana, M. N., Carreira, C., Muriel, A., *et al.*, *Magnetic resonance imaging in the preoperative assessment of patients with primary breast cancer: systematic review of diagnostic accuracy and meta-analysis*, Eur Radiol **22**, 26 (2012).

[17] Lee, C. H., Dershaw, D. D., Kopans, D., *et al.*, *Breast cancer screening with imaging: recommendations from the society of breast imaging and the ACR on the use of mammography, breast MRI, breast ultrasound, and other technologies for the detection of clinically occult breast cancer*, J Am Coll Radiol **7**, 18 (2010).

[18] Grosenick, D., Rinneberg, H., Cubeddu, R., and Taroni, P., *Review of optical breast imaging and spectroscopy*, J Biomed Opt **21**, 091311 (2016).

[19] Goorden, M. C., van der Have, F., Kreuger, R., *et al.*, *VECTor: A preclinical imaging system for simultaneous submillimeter SPECT and PET*, J Nucl Med **54**, 306 (2013).

[20] Ghaly, M., Links, J. M., and Frey, E. C., *Optimization and comparison of simultaneous and separate acquisition protocols for dual isotope myocardial perfusion SPECT*, Phys Med Biol **60**, 5083 (2015).

[21] Ivashchenko, O., van der Have, F., Goorden, M. C., Ramakers, R. M., and Beekman, F. J., *Ultra-high-sensitivity submillimeter mouse SPECT*, J Nucl Med **56**, 470 (2015).

[22] Kelkar, S. S. and Reineke, T. M., *Theranostics: Combining imaging and therapy*, Bioconjugate Chem **22**, 1879 (2011).

[23] Specht, J. M. and Mankoff, D. A., *Advances in molecular imaging for breast cancer detection and characterization*, Breast Cancer Res **14**, 206 (2012).

[24] Yordanova, A., Eppard, E., Kurpig, S., *et al.*, *Theranostics in nuclear medicine practice*, OncoTargets Ther **10**, 4821 (2017).

[25] Penuelas, I., Dominguez-Prado, I., Garcia-Velloso, M. J., *et al.*, *PET tracers for clinical imaging of breast cancer*, J Oncol **2012**, 710561 (2012).

[26] Berg, W. A., *Nuclear breast imaging: Clinical results and future directions*, J Nucl Med **57 Suppl 1**, 46S (2016).

[27] Wibmer, A. G., Hricak, H., Ulaner, G. A., and Weber, W., *Trends in oncologic hybrid imaging*, Eur J Hybrid Imaging **2**, 1 (2018).

[28] Brem, R. F., Schoonjans, J. M., Kieper, D. A., *et al.*, *High-resolution scintimammography: a pilot study*, J Nucl Med **43**, 909 (2002).

[29] Hruska, C. B., Phillips, S. W., Whaley, D. H., Rhodes, D. J., and O'Connor, M. K., *Molecular breast imaging: Use of a dual-head dedicated gamma camera to detect small breast tumors*, Am J Roentgenol **191**, 1805 (2008).

[30] Hruska, C. B. and O'Connor, M. K., *Nuclear imaging of the breast: Translating achievements in instrumentation into clinical use*, Med Phys **40**, 050901 (2013).

[31] Rhodes, D. J., Hruska, C. B., Conners, A. L., *et al.*, *Molecular breast imaging at reduced radiation dose for supplemental screening in mammographically dense breasts*, Am J Roentgenol **204**, 241 (2015).

[32] van Roosmalen, J., Goorden, M. C., and Beekman, F. J., *Molecular breast tomosynthesis with scanning focus multi-pinhole cameras*, Phys Med Biol **61**, 5508 (2016).

[33] van Roosmalen, J., Beekman, F. J., and Goorden, M. C., *System geometry optimization for molecular breast tomosynthesis with focusing multi-pinhole collimators*, Phys Med Biol **63**, 015018 (2017).

[34] Copeland, D. E. and Benjamin, E. W., *Pinhole camera for gamma-ray sources*, Nucleonics **5**, 44 (1949).

[35] Anger, H. O., *Use of a gamma-ray pinhole camera for in vivo studies*, Nature **170**, 200 (1952).

[36] Wouters, A., Simon, K. M., and Hirschbe, J. G., *Direct method of decoding multiple images*, Appl Optics **12**, 1871 (1973).

[37] Chang, L. T., Kaplan, S. N., Macdonald, B., Perezmen.V, and Shiraishi, L., *Method of tomographic imaging using a multiple pinhole-coded aperture*, J Nucl Med **15**, 1063 (1974).

[38] Beekman, F. J. and van der Have, F., *The pinhole: gateway to ultra-high-resolution three-dimensional radionuclide imaging*, Eur J Nucl Med Mol Imaging **34**, 151 (2007).

[39] Beekman, F. J., van der Have, F., Vastenhouw, B., *et al.*, U-SPECT-I: *A novel system for submillimeter-resolution tomography with radiolabeled molecules in mice*, J Nucl Med **46**, 1194 (2005).

[40] Meikle, S. R., Kench, P., Kassiou, M., and Banati, R. B., *Small animal SPECT and its place in the matrix of molecular imaging technologies*, Phys Med Biol **50**, R45 (2005).

[41] Franc, B. L., Acton, P. D., Mari, C., and Hasegawa, B. H., *Small-animal SPECT and SPECT/CT: important tools for preclinical investigation*, J Nucl Med **49**, 1651 (2008).

[42] van der Have, F., Vastenhouw, B., Ramakers, R. M., *et al.*, U-SPECT-II: *An ultra-high-resolution device for molecular small-animal imaging*, J Nucl Med **50**, 599 (2009).

[43] Vogel, R. A., Kirch, D., LeFree, M., and Steele, P., *A new method of multiplanar emission tomography using a seven pinhole collimator and an Anger scintillation camera*, J Nucl Med **19**, 648 (1978).

[44] Seret, A., Defrise, M., and Blocklet, D., *180 degrees pinhole SPET with a tilted detector and OS-EM reconstruction: phantom studies and potential clinical applications*, Eur J Nucl Med **28**, 1836 (2001).

[45] Bocher, M., Blevis, I. M., Tsukerman, L., *et al.*, *A fast cardiac gamma camera with dynamic SPECT capabilities: design, system validation and future potential*, Eur J Nucl Med Mol Imaging **37**, 1887 (2010).

[46] Beekman, F., *Gamma radiation imaging apparatus*, (US Patents US9168014B2, 2013).

[47] Chen, Y., Vastenhouw, B., Wu, C., Goorden, M. C., and Beekman, F. J., *Optimized image acquisition for dopamine transporter imaging with ultra-high resolution clinical pinhole SPECT*, Phys Med Biol **63**, 225002 (2018).

[48] Beekman, F. J., van der Have, F., Goorden, M. C., *et al.*, G-SPECT-I: *a full ring high sensitivity and ultra-fast clinical molecular imaging system with < 3mm resolution*, in *Annual Congress of the European Association of Nuclear Medicine 2015*, Vol. 42 (SPRINGER, NEW YORK, USA, 2015).

[49] Anger, H. O., *Scintillation camera*, Rev Sci Instrum **29**, 27 (1958).

[50] Peterson, T. E. and Furenlid, L. R., *SPECT detectors: the Anger camera and beyond*, Phys Med Biol **56**, R145 (2011).

[51] Barber, H. B., Apotovsky, B. A., Augustine, F. L., *et al.*, *Semiconductor pixel detectors for gamma-*

ray imaging in nuclear medicine, Nucl Instrum Meth A **395**, 421 (1997).

[52] Luke, P. N., Amman, M., Phlips, B. F., Johnson, W. N., and Kroeger, R. A., *Germanium orthogonal strip detectors with amorphous-semiconductor contacts*, IEEE Trans Nucl Sci **47**, 1360 (2000).

[53] Korevaar, M. A. N., Goorden, M. C., Heemskerk, J. W. T., and Beekman, F. J., *Maximum-likelihood scintillation detection for EM-CCD based gamma cameras*, Phys Med Biol **56**, 4785 (2011).

[54] Wang, B., van Roosmalen, J., Piët, L., *et al.*, *Voxelized ray-tracing simulation dedicated to multi-pinhole molecular breast tomosynthesis*, Biomed Phys Eng Expr **3**, 045021 (2017).

[55] Mueller, B., O'Connor, M. K., Blevis, I., *et al.*, *Evaluation of a small cadmium zinc telluride detector for scintimammography*, J Nucl Med **44**, 602 (2003).

[56] Coover, L. R., Caravaglia, G., and Kuhn, P., *Scintimammography with dedicated breast camera detects and localizes occult carcinoma*, J Nucl Med **45**, 553 (2004).

[57] Hruska, C. B., Weinmann, A. L., and O'Connor, M. K., *Proof of concept for low-dose molecular breast imaging with a dual-head CZT gamma camera. Part I. Evaluation in phantoms*, Med Phys **39**, 3466 (2012).

[58] Hruska, C. B., Weinmann, A. L., Skjerseth, C. M. T., *et al.*, *Proof of concept for low-dose molecular breast imaging with a dual-head CZT gamma camera. Part II. Evaluation in patients*, Med Phys **39**, 3476 (2012).

[59] Siman, W. and Kappadath, S. C., *Performance characteristics of a new pixelated portable gamma camera*, Med Phys **39**, 3435 (2012).

[60] Long, Z., Conners, A. L., Hunt, K. N., Hruska, C. B., and O'Connor, M. K., *Performance characteristics of dedicated molecular breast imaging systems at low doses*, Med Phys **43**, 3062 (2016).

[61] Fowler, A. M., *A molecular approach to breast imaging*, J Nucl Med **55**, 177 (2014).

[62] Tornai, M. P., Bowsher, J. E., Jaszczak, R. J., *et al.*, *Mammotomography with pinhole incomplete circular orbit SPECT*, J Nucl Med **44**, 583 (2003).

[63] Brzymialkiewicz, C. N., Tornai, M. P., McKinley, R. L., and Bowsher, J. E., *Evaluation of fully 3-D emission mammotomography with a compact cadmium zinc telluride detector*, IEEE Trans Med Imaging **24**, 868 (2005).

[64] Raylman, R. R., Majewski, S., Smith, M. F., *et al.*, *The positron emission mammography/tomography breast imaging and biopsy system (PEM/PET): design, construction and phantom-based measurements*, Phys Med Biol **53**, 637 (2008).

[65] MacDonald, L., Edwards, J., Lewellen, T., *et al.*, *Clinical imaging characteristics of the positron emission mammography camera: PEM Flex Solo II*, J Nucl Med **50**, 1666 (2009).

[66] Baghaei, H., Li, H. D., Zhang, Y. X., *et al.*, *A breast phantom lesion study with the high resolution transformable HOTPET camera*, IEEE Trans Nucl Sci **57**, 2504 (2010).

[67] Williams, M. B., Judy, P. G., Gunn, S., and Majewski, S., *Dual-modality breast tomosynthesis*, Radiology **255**, 191 (2010).

[68] Yanagida, T., Yoshikawa, A., Yokota, Y., *et al.*, *Development of Pr:LuAG scintillator array and assembly for positron emission mammography*, IEEE Trans Nucl Sci **57**, 1492 (2010).

[69] Moliner, L., Gonzalez, A. J., Soriano, A., *et al.*, *Design and evaluation of the MAMMI dedicated breast PET*, Med Phys **39**, 5393 (2012).

[70] Gopan, O., Gilland, D., Weisenberger, A., Kross, B., and Welch, B., *Molecular imaging of the*

breast using a variable-angle slant-hole collimator, IEEE Trans Nucl Sci **61**, 1143 (2014).

[71] Gong, Z. Y. and Williams, M. B., *Comparison of breast specific gamma imaging and molecular breast tomosynthesis in breast cancer detection: Evaluation in phantoms*, Med Phys **42**, 4250 (2015).

[72] Rogers, D. W. O., *Fifty years of Monte Carlo simulations for medical physics*, Phys Med Biol **51**, R287 (2006).

[73] Haynor, D. R., Harrison, R. L., Lewellen, T. K., *et al.*, *Improving the efficiency of emission tomography simulations using variance reduction techniques*, IEEE Trans Nucl Sci **37**, 749 (1990).

[74] Gieles, M., de Jong, H. W. A. M., and Beekman, F. J., *Monte Carlo simulations of pinhole imaging accelerated by kernel-based forced detection*, Phys Med Biol **47**, 1853 (2002).

[75] De Beenhouwer, J., Staelens, S., Kruecker, D., *et al.*, *Cluster computing software for GATE simulations*, Med Phys **34**, 1926 (2007).

[76] Jan, S., Santin, G., Strul, D., *et al.*, *GATE: A simulation toolkit for PET and SPECT*, Phys Med Biol **49**, 4543 (2004).

[77] Jan, S., Benoit, D., Becheva, E., *et al.*, *GATE V6: A major enhancement of the GATE simulation platform enabling modelling of CT and radiotherapy*, Phys Med Biol **56**, 881 (2011).

[78] Devries, D. J., Moore, S. C., Zimmerman, R. E., *et al.*, *Development and validation of a Monte-Carlo simulation of photon transport in an Anger camera*, IEEE Trans Med Imaging **9**, 430 (1990).

[79] Cot, A., Sempau, J., Pareto, D., *et al.*, *Evaluation of the geometric, scatter, and septal penetration components in fan-beam collimators using Monte Carlo simulation*, IEEE Trans Nucl Sci **49**, 12 (2002).

[80] Cot, A., Sempau, J., Pareto, D., *et al.*, *Study of the point spread function (PSF) for I-123 SPECT imaging using Monte Carlo simulation*, Phys Med Biol **49**, 3125 (2004).

[81] Hunter, W. C. J., Barrett, H. H., Muzi, J. P., *et al.*, *SCOUT: a fast Monte-Carlo modeling tool of scintillation camera output*, Phys Med Biol **58**, 3581 (2013).

[82] Lippuner, J. and Elbakri, I. A., *A GPU implementation of EGSnrc's Monte Carlo photon transport for imaging applications*, Phys Med Biol **56**, 7145 (2011).

[83] Bert, J., Perez-Ponce, H., El Bitar, Z., *et al.*, *Geant4-based Monte Carlo simulations on GPU for medical applications*, Phys Med Biol **58**, 5593 (2013).

[84] Garcia, M.-P., Bert, J., Benoit, D., Bardiès, M., and Visvikis, D., *Accelerated GPU based SPECT Monte Carlo simulations*, Phys Med Biol **61**, 4001 (2016).

[85] Wang, H. L., Jaszczak, R. J., and Coleman, R. E., *A new composite model of objects for Monte-Carlo simulation of radiological imaging*, Phys Med Biol **38**, 1235 (1993).

[86] Beekman, F. J., de Jong, H. W. A. M., and Slijpen, E. T. P., *Efficient SPECT scatter calculation in non-uniform media using correlated Monte Carlo simulation*, Phys Med Biol **44**, N183 (1999).

[87] de Jong, H. W. A. M., Slijpen, E. T. P., and Beekman, F. J., *Acceleration of Monte Carlo SPECT simulation using convolution-based forced detection*, IEEE Trans Nucl Sci **48**, 58 (2001).

[88] Ljungberg, M., Larsson, A., and Johansson, L., *A new collimator simulation in SIMIND based on the delta-scattering technique*, IEEE Trans Nucl Sci **52**, 1370 (2005).

[89] Rehfeld, N. S., Stute, S., Apostolakis, J., Soret, M., and Buvat, I., *Introducing improved voxel navigation and fictitious interaction tracking in GATE for enhanced efficiency*, Phys Med Biol

54, 2163 (2009).

[90] Descourt, P., Carlier, T., Du, Y., *et al.*, *Implementation of angular response function modeling in SPECT simulations with GATE*, Phys Med Biol **55**, N253 (2010).

[91] El Bitar, Z., Bekaert, V., and Brasse, D., *Acceleration of fully 3D Monte Carlo based system matrix computation for image reconstruction in small animal SPECT*, IEEE Trans Nucl Sci **58**, 121 (2011).

[92] Feng, B., Chen, M., Bai, B., *et al.*, *Modeling of the point spread function by numerical calculations in single-pinhole and multipinhole SPECT reconstruction*, IEEE Trans Nucl Sci **57**, 173 (2010).

[93] Goorden, M. C., van der Have, F., Kreuger, R., and Beekman, F. J., *An efficient simulator for pinhole imaging of PET isotopes*, Phys Med Biol **56**, 1617 (2011).

[94] Li, X. and Furenlid, L. R., *A SPECT system simulator built on the SolidWorks™ 3D-Design package*, in SPIE Optical Engineering + Applications 2014, Vol. 9214 (2014).

[95] Siddon, R. L., *Fast calculation of the exact radiological path for a 3-dimensional CT array*, Med Phys **12**, 252 (1985).

[96] Smith, M. F., Jaszczak, R. J., Wang, H. L., and Li, J. Y., *Lead and tungsten pinhole inserts for I-131 SPECT tumor imaging: Experimental measurements and photon transport simulations*, IEEE Trans Nucl Sci **44**, 74 (1997).

[97] Goertzen, A. L., Beekman, F. J., and Cherry, S. R., *Effect of phantom voxelization in CT simulations*, Med Phys **29**, 492 (2002).

[98] Schramm, N. U., Ebel, G., Engeland, U., *et al.*, *High-resolution SPECT using multipinhole collimation*, IEEE Trans Nucl Sci **50**, 315 (2003).

[99] Tabary, J., Guillemaud, R., Mathy, F., Gliere, A., and Hugonnard, P., *Combination of high resolution analytically computed uncollided flux images with low resolution Monte Carlo computed scattered flux images*, IEEE Trans Nucl Sci **51**, 212 (2004).

[100] Funk, T., Kirch, D. L., Sun, M. S., *et al.*, *Simulation and validation of point spread functions in pinhole SPECT imaging*, IEEE Trans Nucl Sci **53**, 2729 (2006).

[101] Lin, J. Y., Kench, P. L., Gregoire, M. C., and Meikle, S. R., *Projection process modelling for iterative reconstruction of pinhole SPECT*, IEEE Trans Nucl Sci **57**, 2578 (2010).

[102] Matej, S. and Lewitt, R. M., *Practical considerations for 3-D image reconstruction using spherically symmetric volume elements*, IEEE Trans Med Imaging **15**, 68 (1996).

[103] Zbijewski, W. and Beekman, F. J., *Comparison of methods for suppressing edge and aliasing artefacts in iterative X-ray CT reconstruction*, Phys Med Biol **51**, 1877 (2006).

[104] Meagher, D., *Geometric modeling using octree encoding*, Comput Vision Graph **19**, 129 (1982).

[105] Glassner, A. S., *Space subdivision for fast ray tracing*, IEEE Comput Graph **4**, 15 (1984).

[106] Ogawa, K. and Maeda, S., *A Monte Carlo method using octree structure in photon and electron transport*, IEEE Trans Nucl Sci **42**, 2322 (1995).

[107] Suganuma, R. and Ogawa, K., *Effective description of a 3D object for photon transportation in Monte Carlo simulation*, IEEE Trans Nucl Sci **47**, 1024 (2000).

[108] Hubert-Tremblay, V., Archambault, L., Tubic, D., Roy, R., and Beaulieu, L., *Octree indexing of DICOM images for voxel number reduction and improvement of Monte Carlo simulation computing efficiency*, Med Phys **33**, 2819 (2006).

[109] Sarrut, D. and Guigues, L., *Region-oriented CT image representation for reducing computing*

time of Monte Carlo simulations, Med Phys **35**, 1452 (2008).

[110] Badal, A., Kyprianou, I., Banh, D. P., Badano, A., and Sempau, J., *penMesh — Monte Carlo radiation transport simulation in a triangle mesh geometry*, IEEE Trans Med Imaging **28**, 1894 (2009).

[111] Huesman, R. H., Klein, G. J., Moses, W. W., *et al.*, *List-mode maximum-likelihood reconstruction applied to positron emission mammography (PEM) with irregular sampling*, IEEE Trans Med Imaging **19**, 532 (2000).

[112] Wackers, F. J. T., Berman, D. S., Maddahi, J., *et al.*, *Technetium-99m hexakis 2-methoxyisobutyl isonitrile - human biodistribution, dosimetry, safety, and preliminary comparison to Tl-201 for myocardial perfusion imaging*, J Nucl Med **30**, 301 (1989).

[113] Maublant, J., deLatour, M., Mestas, D., *et al.*, *Technetium-99m-sestamibi uptake in breast tumor and associated lymph nodes*, J Nucl Med **37**, 922 (1996).

[114] Pani, R., De Vincentis, G., Scopinaro, F., *et al.*, *Dedicated gamma camera for single photon emission mammography (SPEM)*, IEEE Trans Nucl Sci **45**, 3127 (1998).

[115] Gruber, G. J., Moses, W. W., and Derenzo, S. E., *Monte Carlo simulation of breast tumor imaging properties with compact, discrete gamma cameras*, IEEE Trans Nucl Sci **46**, 2119 (1999).

[116] Williams, M. B., Narayanan, D., More, M. J., *et al.*, *Analysis of position-dependent Compton scatter in scintimammography with mild compression*, IEEE Trans Nucl Sci **50**, 1643 (2003).

[117] Hruska, C. B. and O'Connor, M. K., *CZT detectors: How important is energy resolution for nuclear breast imaging*, Phys Medica **21**, 72 (2006).

[118] Hruska, C. B. and O'Connor, M. K., *A Monte Carlo model for energy spectra analysis in dedicated nuclear breast imaging*, IEEE Trans Nucl Sci **55**, 491 (2008).

[119] Campbell, D. L. and Peterson, T. E., *Simulation study comparing high-purity germanium and cadmium zinc telluride detectors for breast imaging*, Phys Med Biol **59**, 7059 (2014).

[120] Segars, W. P. and Tsui, B. M. W., *MCAT to XCAT: The evolution of 4-D computerized phantoms for imaging research*, Proc IEEE **97**, 1954 (2009).

[121] Vastenhouw, B. and Beekman, F. J., *Submillimeter total-body murine imaging with U-SPECT-I*, J Nucl Med **48**, 487 (2007).

[122] Assie, K., Gardin, I., Vera, P., and Buvat, I., *Validation of the Monte Carlo simulator GATE for indium-111 imaging*, Phys Med Biol **50**, 3113 (2005).

[123] Lamare, F., Turzo, A., Bizais, Y., Le Rest, C. C., and Visvikis, D., *Validation of a Monte Carlo simulation of the Philips Allegro/GEMINI PET systems using GATE*, Phys Med Biol **51**, 943 (2006).

[124] Schmidtlein, C. R., Kirov, A. S., Nehmeh, S. A., *et al.*, *Validation of GATE Monte Carlo simulations of the GE Advance/Discovery LS PET scanners*, Med Phys **33**, 198 (2006).

[125] Staelens, S., Vunckx, K., De Beenhouwer, J., *et al.*, *GATE simulations for optimization of pinhole imaging*, Nucl Instrum Meth A **569**, 359 (2006).

[126] Brunner, F. C., Khoury, R., Benoit, D., *et al.*, *Simulation of PIXSCAN, a photon counting micro-CT for small animal imaging*, J Instrum **4**, P05012 (2009).

[127] Chen, Y., Liu, B., O'Connor, J. M., Didier, C. S., and Glick, S. J., *Characterization of scatter in cone-beam CT breast imaging: Comparison of experimental measurements and Monte Carlo simulation*, Med Phys **36**, 857 (2009).

[128] van der Laan, D. J., Schaart, D. R., Maas, M. C., *et al.*, *Optical simulation of monolithic scintil-*

lator detectors using GATE/GEANT4, Phys Med Biol **55**, 1659 (2010).

[129] Grevillot, L., Frisson, T., Maneval, D., *et al.*, *Simulation of a 6 MV Elekta Precise Linac photon beam using GATE/GEANT4*, Phys Med Biol **56**, 903 (2011).

[130] Li, C. M., Segars, W. P., Tourassi, G. D., Boone, J. M., and Dobbins, J. T., *Methodology for generating a 3D computerized breast phantom from empirical data*, Med Phys **36**, 3122 (2009).

[131] Segars, W. P., Sturgeon, G., Mendonca, S., Grimes, J., and Tsui, B. M. W., *4D XCAT phantom for multimodality imaging research*, Med Phys **37**, 4902 (2010).

[132] Wang, H. L., Scarfone, C., Greer, K. L., Coleman, R. E., and Jaszczak, R. J., *Prone breast tumor imaging using vertical axis-of-rotation (VAOR) SPECT: An initial study*, IEEE Trans Nucl Sci **44**, 1271 (1997).

[133] Hruska, C. B. and O'Connor, M. K., *Quantification of lesion size, depth, and uptake using a dual-head molecular breast imaging system*, Med Phys **35**, 1365 (2008).

[134] Perez, K. L., Cutler, S. J., Madhav, P., and Tornai, M. P., *Characterizing the contribution of cardiac and hepatic uptake in dedicated breast SPECT using tilted trajectories*, Phys Med Biol **55**, 4721 (2010).

[135] Ogawa, K., Harata, Y., Ichihara, T., Kubo, A., and Hashimoto, S., *A practical method for position-dependent compton-scatter correction in single photon-emission CT*, IEEE Trans Med Imaging **10**, 408 (1991).

[136] Ichihara, T., Ogawa, K., Motomura, N., Kubo, A., and Hashimoto, S., *Compton scatter compensation using the triple-energy window method for single-isotope and dual-isotope SPECT*, J Nucl Med **34**, 2216 (1993).

[137] Hashimoto, J., Kubo, A., Ogawa, K., *et al.*, *Scatter and attenuation correction in technetium-99m brain SPECT*, J Nucl Med **38**, 157 (1997).

[138] Hutton, B. F., Buvat, I., and Beekman, F. J., *Review and current status of SPECT scatter correction*, Phys Med Biol **56**, R85 (2011).

[139] Zaidi, H. and Koral, K. F., *Scatter modelling and compensation in emission tomography*, Eur J Nucl Med Mol Imaging **31**, 761 (2004).

[140] Wang, B., Kreuger, R., Beekman, F. J., and Goorden, M. C., *Novel light-guide-PMT geometries to reduce dead edges of a scintillation camera*, Phys Medica **48**, 84 (2018).

[141] Freifelder, R., Haigh, A. T., and Karp, J. S., *Reducing edge effects and improving position resolution in position-sensitive NaI(Tl) detectors*, IEEE Trans Nucl Sci **40**, 208 (1993).

[142] Wong, W. H., Uribe, J., Hicks, K., and Hu, G. J., *An analog decoding BGO block detector using circular photomultipliers*, IEEE Trans Nucl Sci **42**, 1095 (1995).

[143] Surti, S., Freifelder, R., and Karp, J. S., *Slotted surface treatment of position-sensitive NaI(Tl) detectors to improve detector performance*, IEEE Trans Nucl Sci **48**, 2418 (2001).

[144] Rozler, M., Liang, H. N., and Chang, W., *Development of a cost-effective modular pixelated NaI(Tl) detector for clinical SPECT applications*, IEEE Trans Nucl Sci **59**, 1831 (2012).

[145] Joung, J., Miyaoka, R. S., and Lewellen, T. K., *cMiCE: a high resolution animal PET using continuous LSO with a statistics based positioning scheme*, Nucl Instrum Meth A **489**, 584 (2002).

[146] Domingo-Pardo, C., Goel, N., Engert, T., *et al.*, *A position sensitive gamma-ray scintillator detector with enhanced spatial resolution, linearity, and field of view*, IEEE Trans Med Imaging **28**, 2007 (2009).

[147] Deprez, K., Vandenberghe, S., Vandeghinste, B., and Van Holen, R., *FlexiSPECT: A SPECT system consisting of a compact high-resolution scintillation detector (SPECTatress) and a lofthole collimator*, IEEE Trans Nucl Sci **60**, 53 (2013).

[148] Bruyndonckx, P., Lemaitre, C., van der Laan, D. J., *et al.*, *Evaluation of machine learning algorithms for localization of photons in undivided scintillator blocks for PET detectors*, IEEE Trans Nucl Sci **55**, 918 (2008).

[149] Li, Z., Wedrowski, M., Bruyndonckx, P., and Vandersteen, G., *Nonlinear least-squares modeling of 3D interaction position in a monolithic scintillator block*, Phys Med Biol **55**, 6515 (2010).

[150] Schaart, D. R., van Dam, H. T., Seifert, S., *et al.*, *A novel, SiPM-array-based, monolithic scintillator detector for PET*, Phys Med Biol **54**, 3501 (2009).

[151] Marcinkowski, R., Mollet, P., Van Holen, R., and Vandenberghe, S., *Sub-millimetre DOI detector based on monolithic LYSO and digital SiPM for a dedicated small-animal PET system*, Phys Med Biol **61**, 2196 (2016).

[152] Korevaar, M. A. N., Heemskerk, J. W. T., Goorden, M. C., and Beekman, F. J., *Multi-scale algorithm for improved scintillation detection in a CCD-based gamma camera*, Phys Med Biol **54**, 831 (2009).

[153] Doshi, N. K., Shao, Y. P., Silverman, R. W., and Cherry, S. R., *Design and evaluation of an LSO PET detector for breast cancer imaging*, Med Phys **27**, 1535 (2000).

[154] Gruber, G. J., Choong, W. S., Moses, W. W., *et al.*, *A compact 64-pixel CsI(Tl)/Si PIN photodiode imaging module with IC readout*, IEEE Trans Nucl Sci **49**, 147 (2002).

[155] Miller, B. W., Barber, H. B., Barrett, H. H., *et al.*, *Single-photon spatial and energy resolution enhancement of a columnar CsI(Tl)/EMCCD gamma-camera using maximum-likelihood estimation*, in *Medical Imaging 2006*, Vol. 6142 (2006).

[156] Raylman, R. R., Majewski, S., Kross, B., *et al.*, *Development of a dedicated positron emission tomography system for the detection and biopsy of breast cancer*, Nucl Instrum Meth A **569**, 291 (2006).

[157] Krizsan, A. K., Lajtos, I., Dahlbom, M., *et al.*, *A promising future: Comparable imaging capability of MRI-compatible silicon photomultiplier and conventional photosensor preclinical PET systems*, J Nucl Med **56**, 1948 (2015).

[158] Butler, J. F., Lingren, C. L., Friesenhahn, S. J., *et al.*, *CdZnTe solid-state gamma camera*, IEEE Trans Nucl Sci **45**, 359 (1998).

[159] Gray, R. M. and Macovski, A., *Maximum a posteriori estimation of position in scintillation cameras*, IEEE Trans Nucl Sci **23**, 849 (1976).

[160] Barrett, H. H., Hunter, W. C. J., Miller, B. W., *et al.*, *Maximum-likelihood methods for processing signals from gamma-ray detectors*, IEEE Trans Nucl Sci **56**, 725 (2009).

[161] Joung, J., Miyaoka, R. S., Kohlmyer, S. G., and Lewellen, T. K., *Investigation of bias-free positioning estimators for the scintillation cameras*, IEEE Trans Nucl Sci **48**, 715 (2001).

[162] Hamamatsu, *Photomultiplier tubes and related products* (Hamamatsu Photonics K.K., Japan, 2016).

[163] Janecek, M. and Moses, W. W., *Optical reflectance measurements for commonly used reflectors*, IEEE Trans Nucl Sci **55**, 2432 (2008).

[164] Dorenbos, P., de Haas, J. T. M., and van Eijk, C. W. E., *Non-proportionality in the scintillation*

response and the energy resolution obtainable with scintillation crystals, IEEE Trans Nucl Sci **42**, 2190 (1995).

[165] Moszynski, M., Zalipska, J., Balcerzyk, M., *et al.*, *Intrinsic energy resolution of NaI(Tl)*, Nucl Instrum Meth A **484**, 259 (2002).

[166] Moore, S. K., *ModPET: Novel applications of scintillation cameras to preclinical PET*, Thesis, The University of Arizona (2011).

[167] Vinke, R. and Levin, C. S., *A method to achieve spatial linearity and uniform resolution at the edges of monolithic scintillation crystal detectors*, Phys Med Biol **59**, 2975 (2014).

[168] NEMA, *NEMA Standards Publication NU 1-2007: Performance Measurement of Gamma Cameras* (National Electrical Manufacturers Association, USA, 2007).

[169] Villena, J. L., Tapias, G., Lage, E., Kreuger, R., and Beekman, F. J., *Evaluation of a 25—511 keV list mode readout system for a large field-of-view gamma camera*, in IEEE Nuclear Science Symposium Conference Record (NSS/MIC) 2010 (2010) pp. 2168–2173.

[170] Hesterman, J. Y., Caucci, L., Kupinski, M. A., Barrett, H. H., and Furenlid, L. R., *Maximum-likelihood estimation with a contracting-grid search algorithm*, IEEE Trans Nucl Sci **57**, 1077 (2010).

[171] Hunter, W. C. J., *Modeling stochastic processes in gamma-ray imaging detectors and evaluation of a multi-anode PMT scintillation camera for use with maximum-likelihood estimation methods*, Thesis, The University of Arizona (2007).

[172] SensL, *http://sensl.com/estore/arrayj-60035-64p-pcb/*, (2017), [last access: 16 Feb 2017].

[173] Ohara, *Optical Glass datasheets* (Ohara Inc., Japan, 2016).

[174] Wang, B., Kreuger, R., Huizenga, J., Beekman, F. J., and Goorden, M. C., *Experimental validation of a gamma detector with a novel light-guide-PMT geometry to reduce dead edge effects*, IEEE Trans Radiat and Plasma Med Sci **4**, 98 (2019).

[175] Milster, T. D., Aarsvold, J. N., Barrett, H. H., *et al.*, *A full-field modular-gamma camera*, J Nucl Med **31**, 632 (1990).

[176] Vaska, P., Petrillo, M. J., and Muehllehner, G., *Virtual PMTs: Improving centroid positioning performance near the edges of a gamma camera detector*, IEEE Trans Nucl Sci **48**, 645 (2001).

[177] Gilland, D. R., Welch, B. L., Lee, S., Kross, B., and Weisenberger, A. G., *Evaluation of a novel collimator for molecular breast tomosynthesis*, Med Phys **44**, 5740 (2017).

[178] Majewski, S., Popov, V., Wojcik, R., and Weisenberger, A., *Optimization of a mini-gamma camera based on a 2 × 2 array of Hamamatsu H8500 PSPMTs*, Nucl Instrum Meth A **569**, 215 (2006).

[179] Miyaoka, R. S., Li, X., Hunter, W., *et al.*, *Resolution properties of a prototype continuous miniature crystal element (cMiCE) scanner*, IEEE Trans Nucl Sci **58**, 2244 (2011).

[180] Kastis, G. A., Barber, H. B., Barrett, H. H., *et al.*, *Gamma-ray imaging using a CdZnTe pixel array and a high-resolution, parallel-hole collimator*, IEEE Trans Nucl Sci **47**, 1923 (2000).

[181] Wagenaar, D. J., Chowdhury, S., Engdahl, J. C., and Burckhardt, D. D., *Planar image quality comparison between a CdZnTe prototype and a standard NaI(Tl) gamma camera*, Nucl Instrum Meth A **505**, 586 (2003).

[182] Verger, L., Gentet, A. C., Gerfault, L., *et al.*, *Performance and perspectives of a CdZnTe-based gamma camera for medical imaging*, IEEE Trans Nucl Sci **51**, 3111 (2004).

[183] Cai, L., Lai, X. C., Shen, Z. M., Chen, C. T., and Meng, L. J., *MRC-SPECT: A sub-500 μm resolution*

MR-compatible SPECT system for simultaneous dual-modality study of small animals, Nucl Instrum Meth A **734**, 147 (2014).

[184] Groll, A., Kim, K., Bhatia, H., *et al.*, *Hybrid pixel-waveform (HPWF) enabled CdTe detectors for small animal gamma-ray imaging applications*, IEEE Trans Radiat Plasma Sci **1**, 3 (2017).

[185] Ruiz-Gonzalez, M., Bora, V., and Furenlid, L. R., *Maximum-likelihood estimation of scintillation pulse timing*, IEEE Trans Radiat Plasma Sci **2**, 1 (2018).

[186] Furenlid, L. R., Wilson, D. W., Chen, Y. C., *et al.*, *FastSPECT II: A second-generation high-resolution dynamic SPECT imager*, IEEE Trans Nucl Sci **51**, 631 (2004).

[187] Li, X., Ruiz-Gonzalez, M., and Furenlid, L. R., *An edge-readout, multilayer detector for positron emission tomography*, Med Phys **45**, 2425 (2018).

[188] Branderhorst, W., Vastenhouw, B., van der Have, F., *et al.*, *Targeted multi-pinhole SPECT*, Eur J Nucl Med Mol Imaging **38**, 552 (2011).

[189] van der Have, F., Vastenhouw, B., Rentmeester, M., and Beekman, F. J., *System calibration and statistical image reconstruction for ultra-high resolution stationary pinhole SPECT*, IEEE Trans Med Imaging **27**, 960 (2008).

[190] Goorden, M. C., van Roosmalen, J., van der Have, F., and Beekman, F. J., *Optimizing modelling in iterative image reconstruction for preclinical pinhole PET*, Phys Med Biol **61**, 3712 (2016).

[191] Mann, S. D., Perez, K. L., McCracken, E. K. E., *et al.*, *Initial in vivo quantification of Tc-99m sestamibi uptake as a function of tissue type in healthy breasts using dedicated breast SPECT-CT*, J Oncol **2012**, 146943 (2012).

[192] Shepp, L. A. and Vardi, Y., *Maximum likelihood reconstruction for emission tomography*, IEEE Trans Med Imaging **1**, 113 (1982).

[193] Rose, A., *The sensitivity performance of the human eye on an absolute scale*, J Opt Soc Am **38**, 196 (1948).

[194] van Roosmalen, J., Beekman, F. J., and Goorden, M. C., *Comparison of fan beam, slit-slat and multi-pinhole collimators for molecular breast tomosynthesis*, Phys Med Biol **63**, 105009 (2018).

[195] Nuyts, J., Baete, K., Beque, D., and Dupont, P., *Comparison between MAP and postprocessed ML for image reconstruction in emission tomography when anatomical knowledge is available*, IEEE Trans Med Imaging **24**, 667 (2005).

[196] Velikina, J., Leng, S., and Chen, G. H., *Limited view angle tomographic image reconstruction via total variation minimization*, Proc SPIE **6510**, 651020 (2007).

[197] Zhou, Y., Shao, G., and Liu, S., *Monitoring breast tumor lung metastasis by U-SPECT-II/CT with an integrin $\alpha_v\beta_3$-targeted radiotracer* ^{99m}Tc-3P-RGD$_2$, Theranostics **2**, 577 (2012).

[198] Elvas, F., Vangestel, C., Rapic, S., *et al.*, *Characterization of [Tc-99m]duramycin as a SPECT imaging agent for early assessment of tumor apoptosis*, Mol Imaging Biol **17**, 838 (2015).

[199] Josefsson, A., Nedrow, J. R., Park, S., *et al.*, *Imaging, biodistribution, and dosimetry of radionuclide-labeled PD-L1 antibody in an immunocompetent mouse model of breast cancer*, Cancer research **76**, 472 (2016).

[200] Deken, M. M., Bos, D. L., Tummers, W., *et al.*, *Multimodal image-guided surgery of HER2-positive breast cancer using [^{111}In]In-DTPA-trastuzumab-IRDye800CW in an orthotopic breast tumor model*, EJNMMI research **9**, 98 (2019).

[201] Solomon, V. R., Alizadeh, E., Bernhard, W., *et al.*, *^{111}In- and ^{225}Ac-labeled cixutumumab for*

imaging and alpha-particle radiotherapy of IGF-1R positive triple-negative breast cancer, Mol Pharmaceutics **16**, 4807–4816 (2019).

Acknowledgements

In the late afternoon of Oct. 31 2014, a gloomy winter day in Stockholm, I was doing assignments while looking for my future online in a computer room in KTH campus and discovered a vacancy in TU Delft which perfectly matched my background. Though the deadline of the application was just the day after, it was enough to write an application letter on a familiar topic. About one month later, Marlies contacted me and we had a Skype interview. During the interview, Marlies talked very swiftly, and in my later days working with her, I found that she was not only swift in talking but also thinking, reading, moving and even eating. As my daily supervisor, we had a planned weekly meeting when I started in Delft. However, before long, Marlies probably found a planned meeting time slot was not always necessary because most of my problems and results were in fact solved and presented by 'pulling' her out of her office. As the principal investigator of my project, Marlies was the person who pushed the entire project forward. Without her help, the title of this project would be: from simulation to nothing. We have (almost) made 4 publications for this project, and I kept every iteration of the drafts. Whenever I look back into her comments, I can see the improvements and her 'blood, toil, tears and sweat' in them. Before the interview, although Marlies was struggling with her laptop and I was struggling with the darkness in my shabby room, the interview itself probably went very well, because another month later we had another interview face-to-face in Delft.

The trip to Delft was not an easy one. The metro and train delay on Jan. 15 morning in Stockholm made me almost missed the flight, and a slip during my rush to the terminal kept my hip painful for a whole month. When I arrived in Delft in the rainy afternoon, before enjoying the beauty of this lovely town, a car passed by and splashed me entirely (this happened multiple times later). However, the next day (interview day) was one of the sunniest days I ever had in the Netherlands. Jarno received me at the entrance of the reactor institute (RID). In the latter two years, Jarno was the direct person who introduced me to the world of multi-pinhole molecular breast tomosynthesis. The tools he created were the foundation of everything in this project. Even after his graduation, he helped me several times. I also met the newly promoted dr. Pieter Vaissier. A serious man whom I was also always seriously spoke of. When I just started in Delft, one day Pieter was very excited and told me that his paper was accepted. At that time, I did not understand why he was so excited. But over the years, I have become more excited about hearing my paper's acceptance than he did.

Most importantly, in the interview, I met Freek for the first time. A name that I had seen

only on papers. Since the interview, I have learned a lot from Freek why many good researches were not realised in end products. I also got to know many practical issues in the industry from him. His knowledge about the history of the field, suppliers of different components we needed, experts we can turn to, and solutions in many engineering problems facilitated this project and saved me a lot of time from searching information or reinventing the wheel. Without Freek's help, this project might become: from simulation to another simulation. Moreover, he helped extend my first junior researcher contract to a PhD candidate contract in 2017, and again extend to a postdoc contract in 2019 so that I could finish my PhD without worrying much about my life.

At the interview, I made a bold request to Freek that I wanted to visit MILabs the next day, i.e. a Saturday. Though hard to arrange, he managed to ask Chao to give me a guided tour in MILabs the next day. Chao is the first person I know who can talk about our research purely in Chinese. I am still trying to do so but it is not easy. He showed me not only the latest U-SPECT under construction but also how a PhD defence looked like in the Netherlands, which was very intriguing for me (though I could never have the full monty for myself). The Japanese restaurant we ate was still the best I ever had in Europe.

After a very short consideration, I accepted the offer. As soon as I got the Dutch residence permit (2 days after I collected it), I flew to Schiphol and posted 'Hej då Sverige! Hallo Nederland!' to all my acquaintances. Thanks to Trudy for her help in my Dutch residence permit application and later on for all the administrative stuff, especially arranging all my business trips.

Once I started in Delft, I met all other group members. Rob was the one who taught me everything in the labs. Whenever I had problems in my experiment Rob was always the one to turn to. Every time he could draw a very clear map and show me which road I should go for trouble-shooting. Moreover, Rob was the only person asked me for my master thesis which was very moving when I just started (though for some reason he did not give any comments on that). Jan made all the electronics for my setup and he was the solution for all my electric problems. Whatever messy soldering or cable works I made, he could transform them into something nicely done that could be directly sold on bol.com. Jan also initiated several group activities, like buying fish, trailwalk (battle with the bees), group drink, etc. As Rob and Jan have been working in RID for more than a quarter of a century, they knew everyone and everything here. Whenever I needed something from our institute, I could get it via them. Both of them had rich experience in engineering and helped me not only in my project but also many other things in life, e.g. bike, stove, fridge, washing machine, and car driving etc. I also met the other PhD in our group, Sasha. Her PhD defence was the first one I attended in our group. When I worked with her, I was not aware of how hard it was to finish a PhD in 4 years (last year even part-time) as well as participate in social communities, e.g. as the president of PromooD. The mug Sasha gave me when she left Delft was used during my entire PhD period.

As I became more and more senior in the group, we also had new people joining. Yuan, coincidentally also a Chinese PhD candidate. I cannot imagine how difficult it is to travel in the Eindhoven-Delft route or the Eindhoven-Utrecht route for almost four years every day. But she made it. I learned a lot about how to use our group software and what to consider in deep learning and from Yuan, which dramatically facilitated my work. When I ordered parts from China for my project, Yuan introduced her logistic contact to me which saved my time searching for information and a lot of project budget. It was also so nice to cook with her after her relocation in Delft. We would have cooked more if there was no such coronavirus crisis. Minh's arrival in our group was a surprise for me and Jarno. It was only one day before his arrival and we were asked to pick a new PhD candidate up in the train station that we knew there would be a new member in our group. After Minh started in our group, besides quickly getting familiar with his research, he also learned driving, had a son, learned swimming and participated in badminton tournaments. I also wanted to copy his road but got stuck at the learning driving step... Minh helped me a lot in my PhD project whenever I needed to transport some heavy stuff, as well as in my postdoc project, in which he is really expert. Monika joined our group at the end of my PhD. I tried to speak Swedish to her but it did not work well, as my Swedish was almost overwritten by Dutch, and Swedish still differs a lot from Norwegian in pronunciation. We worked on the same project which made it easier for us to verify our own results as we could often compare with each other. I wish Yuan, Minh and Monika's PhD projects will go on smoothly and quickly in the future.

In the office, our group shared the same coffee table with the Luminescence group and we often had a coffee break together. I have met Hongde already during the lunchtime in my interview. When I was in Sweden, I rarely went to restaurants, and neither did my friends. We always cooked together. However, when I started in the Netherlands, Hongde did not want to cook with me but often asked me to go out for dinner. The times I went to restaurants with Hongde exceeded the times I went to restaurants in my entire two years in Sweden. Weronika was not only a colleague but also my flatmate. She always made me think of Maria Skłodowska-Curie (I will not mistake the spelling anymore), and I learned a lot about Poland and flying from her. Roy triggered my interest in beer culture in my second year in the Netherlands until I realised that I am physically not capable of feeling the joy of alcohol. Anna was the 'queen' of the coffee table. The trip she organised in Lower Silesia was the best group trip I had in the five years. I still would like to eat bigos once. Johan was always generous and helpful whenever I needed to use the tool or facility in his lab. I was amazed by the fact that he cycled from Sassenheim to Delft to work almost every day with good weather (35 km one way!). Francesco also helped me when I calibrated our newly bought PMTs and scintillator. He also gave me a lot of advice on my frequent trips to Italy. Evert was the person who made our not-well-functioning PhD community work. Respect! Maybe he did not know, but in my RID 24/7 pass application, I put his name there as the person with whom I stayed together outside regular working hours. Maarten was actually another person who often stayed

with me outside regular working hours. He promised to organise a stamppot party in his apartment. But because of the damned coronavirus, it has not taken place yet. I still look forward to it Maarten! Tianshuai always looks forward to his next paper. I am sure he will get a nice position in China. Giácomo was often the only person having lunch with our group. We always talked about the bad weather when waiting for the microwave. Lei, as a Shanxi Ren, taught me how to cook the best MenMian with the material we could get in the Netherlands. Mubiao was a great example for me about how to make full use of our holidays in travelling in Europe. Adey told me his story from Iraq to Greece to the Netherlands, which was difficult but fortunately the story had a happy ending. John had a comment on the Dutch football team when he was in the group. He should now be more satisfied. Anouk helped me many times, especially for inviting the committee members for my PhD defence. Erik took every chance to promote his students' company. It was lucky for his students with a start-up idea to have a supervisor like him. Prof. Pieter Dorenbos was the person I cannot avoid when I wrote about scintillators in my papers since my master project. When I introduced my master project to Freek in my interview, he promoted RID as 'the building where $LaBr_3$ was discovered'. Pieter was the first person to agree to be a member of my doctoral committee (on a Saturday!) when we were desperately looking for people, which I was very grateful for.

Over time I received a lot of help from many colleagues in RID, to whom I would like to say thanks. The SBD people: Henk, Koos, Radboud, Bouke, Erwin, Josetta, Marlies, and Christian, helped me when I needed to use any available radioactive sources in the building and ensured my (and others') safety when I conducted experiments. When I needed the Tc-koe for my experiment, Jolanda was always there to contact the hospital and arrange it for me, which I felt very grateful for. Malte, Ernst, Kevin and many of the DEMO guys were in charge of the mechanical works involved in my project. They did an excellent job so that our design on-screen could finally become a real thing. Stefan Brunner shared a lot of his knowledge of SiPM and optical interface with me when he was here and after he started in Broadcom. Valerio helped me with GATE installation on the cluster and shared his experience about using GATE on our cluster with me. Giacomo Borghi introduced the magic device of digital SiPM to me and his paper on gamma detector calibration also inspired me a lot. I wish Valerio and Giacomo would get their PhD degree soon. Pablo was once my mentor and he helped me by sharing his knowledge about how to enrich $NaTcO_4$ solutions. Antonia was also my mentor and she was always passionate about work and people and so easy to talk to. Dr. Yao cooked together with me multiple times and she also told me who I should turn to when I have a radiochemical question. When I had a problem with fluid, I turned to Liu Zheng and he gave me several lab tours about the problems and solutions in his research. The WuXiang NiuRou he made was unsurpassed. LongGe (Li Zhaolong) opened the door of buying experiment material/equipment on Taobao to me, which exponentially accelerated my project and saved our group budget. He also gave me a chance to thank Alibaba and Jack Ma papa. LongGe was not only a colleague but also my former flatmate and current landlord. He

allowed me to stay in the apartment after he moved out so that I did not have to sleep under a bridge. I missed his cooking and his pressure cooker so much after he moved out. Tian Bei was one of the very few LaoXiang I met in Europe. We had very nice times making Baozi and Shaomai and playing board games together. I would have passed my driving exam a long time ago if I knew her husband Ruiqi had a driving simulator. Evgenii started his PhD just a few weeks before me and we met at the Dutch lesson. He continued Dutch learning and mastered this language, which was not so common among our foreigners here. Shasha enjoyed her time in the Netherlands partly because of the dinners she had in our apartment. She also invited me for lunch in Tsinghua several times after she went back to China which was very delicious. Zhou Zhou and I somehow 'worked' on the same project shortly, as he needed to use our lab and I opened the door for him occasionally. His research of imaging the microscope from Antoni van Leeuwenhoek was probably the most advertisable work in our institute, as I even heard an introduction of it when I visited Rijksmuseum Boerhaave in Leiden. Xinmin and Yifan chose to start their PhD after quite some years of working experience, which I could hardly imagine how difficult it could be to return to a university from a working place. But they both did good jobs and have seen the dawn of finishing. Jouke was in charge of all the computation issues in his group but also shared his knowledge about our cluster with our group frequently. He was also my neighbour for 2 years and told me a lot of very interesting stories about the past 50 years. Stefan van der Sar and I had a lot of interesting discussions about football: Manchester United and Dutch National (both male and female) teams. The PhD community guys and girl, namely Remco, Hanan, Maxim, Evert, Maarten, and Giácomo (the last three please also refer to the previous paragraph), I think we should be proud of our job. I feel accomplished by helping hold all the activities, and I am sure the PhD community will continue doing great jobs in the future. Many other people in our institute helped me in all different forms or shared fun time with me that I cannot describe one by one here: René, Ico, Peter van Biesen, Haixing, Qian Kun, Peng Bo, Yaolin, Fengjiao, Xuefei, Wenqin, Guorui, Huanhuan, Jiawei, Bowei, Liu Ming, Wang Chao, Runze, Hamutu, Yibole, Ma Chao, Shen Qi, Fengqi.

My alumni from Zhejiang University have been like family members of mine in the Netherlands in the five years. We have held several successful activities like trailwalks, group dinners, BBQ, etc, and it was always great to remember those good old days in Hangzhou. Hou Zhe was the person who picked me to the alumni contact list. When he left Delft he asked me to continue organising activities with the alumni here and I tried to do that. I wish him to return to Delft and receive his PhD degree soon. ZhuanGe (Tao Xuan) was the first alumnus I met in Delft in person. He was also the most ZheDaised person (who stayed in Hangzhou for only 2.5 years) I have ever seen. The SanGuoSha he gave me was one of the very few entertainments I could have during the coronavirus quarantine period. Tianyuan was the initiator of every trailwalk and as a marathon runner, these 15 — 18 km flat land trailwalk routes were so easy for her. I did not dare to run with her once which was a pity. ZheGe (Li Zhe) was one of the few people I met who took Dutch lan-

guage and society learning seriously. Though not from Beijing, his Beijing dialect could get my endorsement. I first heard of Zheng Xuan from my officemate Yuan and met her at several trailwalks including an improvised one in the suburb of Stockholm. Together with Gao Zhenyu, another trailwalk activist, we have planned more dinners in Amsterdam, but unfortunately, the dinners could not be realised because of the coronavirus crisis. Cai Shufan opened a new door about how the younger generation lives for me. It is not proper to describe most of his stories here, but one very impressive case was that he once organised a party at my apartment and I told him I could arrange up to six chairs. But he still invited eight people and asked several of my neighbours for the rest chairs, which was a solution I really appreciated. There are also many other alumni who I could not describe our happy time together with one by one here: Jingyi, Wuyang, Wang Meng, Wang Qu, Feng Kesong, Jia Kangjun, Fangzhou, Zhang Tian, Hu Xin, etc. My language partner Pau was actually also a ZheDa alumnus and it was (almost) not under my influence. He kept me practising Dutch regularly after I finished all free courses. Het is ook heel leuk om de concerten van Rotterdams Philharmonisch Orkest met Pau te gaan. MingShu (Ma Ming) and Zilong were my two other flatmates. The time we had dinners together was memorable and I learned a lot about the academic world in China from them.

My friends in Sweden supported me during my master's study and continued supporting me in my PhD. My master supervisor Mamo understood my decision of joining Delft and turning the CSC PhD opportunity in his group down. When Marlies interviewed me via Skype, she asked if I have any reference contacts. I gave her Mamo's contact before realising that I should first ask for his permission. I immediately sent Mamo an email, but he replied almost instantly that he had already talked with Marlies on a phone call and recommended me. We met almost every year during IEEE conference and I wish we can continue meeting at this conference. My master's classmate Liyun, together with my neighbour Yuquan, organised activities in Stockholm and provided me with chances to return. I also attended the PhD defence of Liyun. Though I did not manage to stay in the lecture room for the entire session (> 2.5 hours!), it was very interesting to experience a different style of PhD defence. LouZhu (Chen Hongjian) was in the same bachelor and master programme as me in Hangzhou and Stockholm. After I came to the Netherlands, he continued his PhD in KTH. Every year his research circle has a conference in Rotterdam, I met him every January. It was like a yearly appointment, which I liked very much.

In the end, I would like to thank my family. My uncle, aunt, and cousins hosted me several times during my trips in the US which were extraordinary experiences. My parents have been waiting for seven years since I left for Europe. It has been too long, and now it is finally the time to return.

Curriculum Vitæ

Beien Wang

王贝恩

8-Jan-1991 Born in Beijing, China.

Aug. 2009 — Jul. 2013	Zhejiang University, Hangzhou, China B.Eng. in Biomedical Engineering
Jul. 2012	National University of Singapore, Singapore Summer Course in Biomedical Engineering
Aug. 2013 — Jun. 2015	KTH, Royal Institute of Technology, Stockholm, Sweden M.Sc. in Medical Engineering Thesis: 3D Scintillation Positioning Method in a Breast-specific Gamma Camera
Jun. 2015 — May 2017	Delft University of Technology, The Netherlands Junior Researcher Project: Gamma detector design for the multi-pinhole molecular breast tomosynthesis
May 2017 — Present	Delft University of Technology, The Netherlands Ph.D. candidate Thesis: Multi-pinhole Molecular Breast Tomosynthesis: from Simulation to Prototype
Jun. 2019 — Present	Delft University of Technology, The Netherlands Postdoc researcher Project: QUARAT: Quantitative Universal Radiotracer Tomography

List of Publications

Peer-Reviewed Journal Article

Beien Wang, Jarno van Roosmalen, Rob Kreuger, Jan Huizenga, Freek J. Beekman, Marlies C. Goorden. *Characterisation of a multi-pinhole molecular breast tomosynthesis scanner*, Physics in Medicine and Biology **under revision** (2020).

Beien Wang, Rob Kreuger, Jan Huizenga, Freek J. Beekman, Marlies C. Goorden. *Experimental validation of a gamma detector with a novel light-guide-PMT geometry to reduce dead edge effects*, IEEE Transactions on Radiation and Plasma Medical Sciences **4** (2019), 98-107.

Beien Wang, Rob Kreuger, Freek J. Beekman, Marlies C. Goorden. *Novel light-guide-PMT geometries to reduce dead edges of a scintillation camera*, Physica Medica — European Journal of Medical Physics **48** (2018), 84-90.

Beien Wang*, Jarno van Roosmalen*, Louis Piët, Marcel A. van Schie, Freek J. Beekman, Marlies C. Goorden. *Voxelized ray-tracing simulation dedicated to multi-pinhole molecular breast tomosynthesis*, Biomedical Physics & Engineering Express **3**.4 (2017), 045021.
**These two authors have equally contributed to this work.*

Conference Abstract

Beien Wang, Rob Kreuger, Jan Huizenga, Freek J. Beekman, Marlies C. Goorden, *First experimental results for a multi-pinhole molecular breast tomosynthesis scanner*, IEEE Nuclear Science Symposium and Medical Imaging Conference 2019, Manchester, UK.
Recipient of Conference Trainee Grant.

Beien Wang, Rob Kreuger, Jan Huizenga, Freek J. Beekman, Marlies C. Goorden, *First experimental results for novel gamma detector for multi-pinhole molecular breast tomosynthesis*, IEEE Nuclear Science Symposium and Medical Imaging Conference 2018, Sydney, Australia.
Recipient of Conference Trainee Grant; Finalist of Christopher J. Thompson NPSS Student Paper Award.

Beien Wang, Wander van der Wal, Jeroen G. Ohm, Freek J. Beekman, Marlies C. Goorden, *Depth-of-interaction estimation for a monolithic NaI(Tl) gamma detector with PMT readout*, IEEE Nuclear Science Symposium and Medical Imaging Conference 2017, Atlanta, USA.
Recipient of Conference Trainee Grant.

Beien Wang, Rob Kreuger, Freek J. Beekman, Marlies C. Goorden, *Low-cost gamma detector with novel light-guide-PMT geometry to increase usable field-of-view*, IEEE Nuclear Science Symposium and Medical Imaging Conference 2016, Strasbourg, France.
Recipient of Conference Trainee Grant.

Beien Wang, Jarno van Roosmalen, Louis Piët, Marcel van Schie, Freek J. Beekman, Marlies C. Goorden, *Fast and accurate ray-tracing simulation of multi-pinhole molecular breast tomosynthesis*, Society of Nuclear Medicine and Molecular Imaging Annual Meeting 2016, San Diego, USA.

Beien Wang, David Larsson, Paolo Bennati, Ivan Valastyán, Massimiliano Colarieti-Tosti, *High linearity 3D scintillation positioning method for gamma scintillation detector*, IEEE Nuclear Science Symposium and Medical Imaging Conference 2015, San Diego, USA.
Recipient of Conference Trainee Grant.

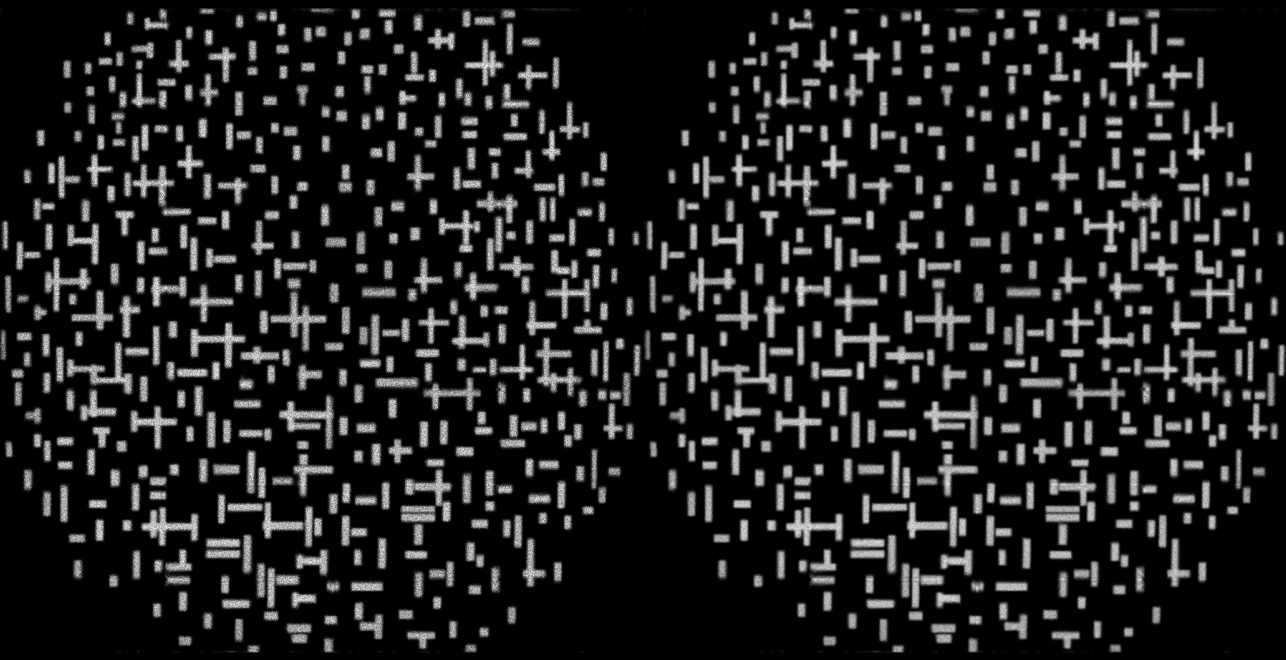

ISBN 978-94-6366-273-4

TU Delft